CHARACTERIZATION AND FEASIBILITY STUDY OF A NEAR INFRARED CCD IMAGER FOR MONITORING TUMOR HEMODYNAMICS

by

MANAN GOEL

Presented to the Faculty of the Graduate School of

The University of Texas at Arlington and University of Southwestern

Medical Center at Dallas in Partial Fulfillment

of the Requirements

for the Degree of

MASTER OF SCIENCE IN BIOMEDICAL ENGINEERING

THE UNIVERSITY OF TEXAS AT ARLINGTON

AUGUST 2006

To my mom Alka and dad Ravi who are my source of inspiration, encouragement and support.

ACKNOWLEDGEMENTS

I would like to express my sincere gratitude to all my professors, colleagues and friends Thank you Dr. Liu for introducing me to the world of research. Without your guidance, encouragement and support, this thesis wouldn't have been possible. I will always cherish the time I spent working at Biomedical Optics Lab.

I thank Dr. Liping Tang and Dr. Jinhui Shen for their help and support during the entire course of this project. Dr. Yuan Bo Peng, your invigorating ideas and valuable suggestions have been inspirational. Thank you for the opportunity to utilize my summer learning and experimenting in your lab. Dr. Vikram Kodibagkar, thank you for your valuable ideas and suggestions and serving on my committee.

I sincerely thank all my lab members for their unwavering support and suggestions during the course of the project.

July 19, 2006

ABSTRACT

CHARACTERIZATION AND FEASIBILITY STUDY OF A NEAR INFRARED CCD IMAGER FOR MONITORING TUMOR HEMODYNAMICS

Publication No. _____

Manan Goel, M.S

The University of Texas at Arlington, 2006

Supervising Professor: Dr. Hanli Liu

Prostate cancer is one of the most common types of cancers diagnosed among North American men. Chemotherapy is generally used to target advanced metastatic prostate cancer. Near infrared spectroscopy (NIRS) has been previously investigated to monitor the hemodynamic changes in rat prostate tumors; however, the previous study with NIRS is limited by its spatial resolution. The goal of this study is to characterize an NIR, CCD imager and to explore the feasibility of using the CCD imager to non-invasively monitor hemodynamic changes in rat prostate tumors during gas intervention. Firstly, studies were conducted to characterize the CCD imager and

understand the propagation of photons through simulated tissue phantoms. These results aid our understanding of light propagation through a uniform medium and detection of photons by the NIR, CCD imager. Secondly, experiments were performed to study the feasibility of the imager to monitor hemodynamic changes in rat prostate tumors during gas intervention. Adult male Copenhagen rats implanted with prostate carcinoma on the fore back were used in this study. Cyclophosphamide, a chemotherapeutic agent, was administered to treat the rat prostate tumors, and pure oxygen was used as gas intervention to introduce hemodynamic perturbation in the tumors during the measurements. After the CCD images were taken at multiple NIR wavelengths, for comparison with the previous records, the images were processed and integrated to provide global temporal files of various hemodynamic parameters for three different groups of rats. A few topographic hemodynamic maps were also obtained, showing spatial heterogeneity within the tumors. The animal experimental results also support the efficacy of cyclophosphamide to be effective in inhibiting the growth of prostate carcinoma. Furthermore, the animal data reveals possible experimental sources causing instability of the measured NIR signals. Overall, this initial study basically demonstrates the feasibility of using a multi-wavelength NIR CCD imager for non-invasively monitoring tumor regional hemodynamics.

TABLE OF CONTENTS

LIST OF ILLUSTRATIONS

LIST OF TABLES

CHAPTER 1

INTRODUCTION

1.1 Significance of Developing an NIR CCD Imager

1.1.1 NIR Spectroscopy

Near infrared (NIR) spectroscopy is a simple and cost effective way of studying the physiological properties of the biological tissues. When light is transmitted through a biological specimen, it undergoes multiple scattering and absorption before it is detected by the optical detector. This detected light carries quantitative information about some physiological parameters. While visible light is strongly attenuated by biological tissues, attenuation in the NIR region of the spectrum is relatively less. Oxygenated hemoglobin [HbO_2] and deoxygenated hemoglobin [Hb] are the main sources of light attenuation in the visible and NIR region. Any variation in concentration levels of [HbO_2] or [Hb] causes a corresponding change in amplitude of detected optical signal. Hence quantities of [HbO_2] or [Hb] can be probed using NIR, and it is possible to non-invasively monitor tumor vascular oxygenation changes during gas intervention [1]. Near infrared spectroscopy has been extensively used for such applications as non-invasive detection of breast cancer, study of cerebral hemodynamics, neonatal and functional brain imaging. Figure 1.1 below shows the absorption spectra of tissue in the NIR window of the spectra.

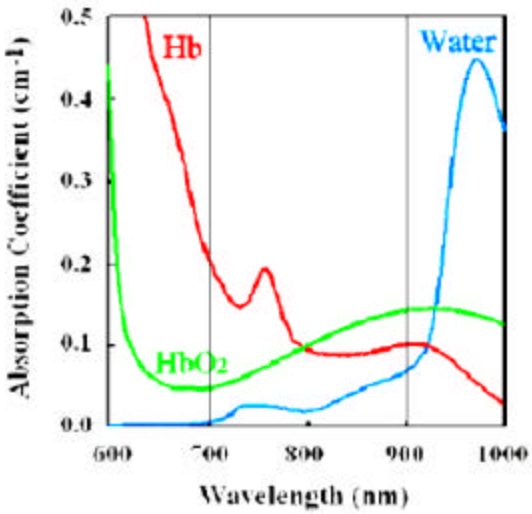

Figure 1.1: Absorption spectra in NIR window (Paunescu 2001)

Hemoglobin concentration in a solution can be determined by using Beer Lambert's law. Biochemists and scientists have developed a notation of absorbance to express light absorption as a function of hemoglobin concentration[2-7],

$$OD = \log(Io / I) = ecL, \tag{1.1}$$

where OD is the optical density, Io is the light intensity of incident light, I is the light intensity of transmitted light, e is the extinction coefficient of hemoglobin, c is the concentration of hemoglobin, and L is the length of light path through the solution. The value of L is assumed to be 1 cm. Blood chromophores of HbO_2 and Hb are the main absorbers of light in the NIR region. Therefore, equation (1.1) can be further expanded as

$$OD^{l} = \{e_{Hb}{}^{l}[Hb] + e_{HbO_2}{}^{l}[HbO_2]\}L, \tag{1.2}$$

where OD^{l} is the optical density or absorbance at wavelength l and $e_{Hb}{}^{l}$ and $e_{HbO_2}{}^{l}$ are the extinction coefficients at wavelength l for molar concentrations of deoxygenated hemoglobin, [Hb], and oxygenated hemoglobin, [HbO_2], respectively. By measuring light absorbance at two wavelengths and known values of extinction coefficients $e_{Hb}{}^{l}$ and $e_{HbO_2}{}^{l}$ for the two wavelengths, oxygenated and deoxygenated hemoglobin concentrations can be determined as expressed below:

$$[HbO_2] = \frac{e_{Hb}{}^{l_2} OD^{l_1} - e_{Hb}{}^{l_1} OD^{l_2}}{L(e_{Hb}{}^{l_2} e_{HbO_2}{}^{l_1} - e_{Hb}{}^{l_1} e_{HbO_2}{}^{l_2})} \tag{1.3}$$

$$[Hb] = \frac{e_{HbO_2}{}^{l_2} OD^{l_1} - e_{HbO_2}{}^{l_1} OD^{l_2}}{L(e_{Hb}{}^{l_1} e_{HbO_2}{}^{l_2} - e_{Hb}{}^{l_2} e_{HbO_2}{}^{l_1})} \tag{1.4}$$

Using equations (1.3) and (1.4), relative changes in [HbO_2] and [Hb] can be calculated as

$$\Delta[HbO_2] = \frac{e_{Hb}{}^{l_2} \Delta OD^{l_1} - e_{Hb}{}^{l_1} \Delta OD^{l_2}}{L(e_{Hb}{}^{l_2} e_{HbO_2}{}^{l^1} - e_{Hb}{}^{l_1} e_{HbO_2}{}^{l_2})} \tag{1.5}$$

$$\Delta[Hb] = \frac{e_{HbO_2}{}^{l_2} \Delta OD^{l_1} - e_{HbO_2}{}^{l_1} \Delta OD^{l_2}}{L(e_{Hb}{}^{l_1} e_{HbO_2}{}^{l_2} - e_{Hb}{}^{l_2} e_{HbO_2}{}^{l_1})} \tag{1.6}$$

$$\Delta[Hb]_{total} = \Delta[Hb] + \Delta[HbO_2] \tag{1.7}$$

The term ΔOD^{l} represents a change in optical density at the specific wavelength, l, and equals log (I_B/I_T), where I_B is the detected light intensity during baseline, and I_T is the detected light intensity under transient conditions.

1.1.2 Limitations of Current Spectroscopic Methods

Hemodynamic changes in rat prostate tumor can be monitored using spectroscopic techniques, such as spectrometry and ISS oximeter. In the single-channel spectrometer method, light is delivered through the tumor tissue and detected by the fiber optic bundle placed at a known separation from the light source. With the setups shown in figures 1.2 (a) and 1.2(b), it is not possible to study detailed regional changes in hemoglobin concentrations occurring in the tumor during gas intervention. Though global changes in tumor tissue hemodynamics can be monitored, it is not possible to get dynamic spatial maps of tissue oxygenation levels which would reveal tumor heterogeneity. Spatial information might prove to be valuable in monitoring effects of chemotherapy for cancer.

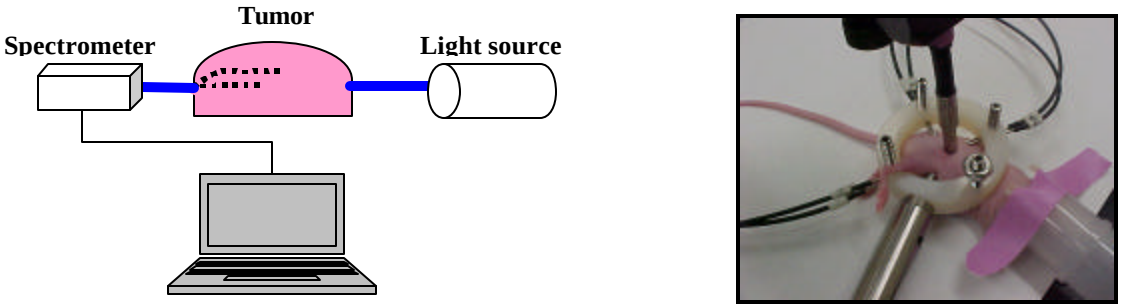

(a) (b)

Figure 1.2: a) Setup of single channel spectrometer. (b) Setup of ISS Oximeter

By using a near infrared CCD imager, it may be possible to non-invasively monitor tumor hemodynamics. High resolution CCD images at different wavelengths can be used to obtain spatial and temporal maps of the hemodynamic changes occurring

in the tumor during gas intervention. These dynamic spatial maps could be useful in showing tumor heterogeneity and could be used for monitoring hemodynamics during chemotherapy.

1.1.3 CCD Imager System

A charged coupled device (CCD) with a camera lens assembly forms the main component of the NIR CCD imaging system. An integrated circuit consisting of a CCD is located just behind the camera lens. The lens focuses a small scene of the image in front of the lens directly onto the CCD imager chip which is behind an optical glass window in its package [8]. The NIR CCD imager consists of a 12-bit CCD chip with an array size of 496 rows and 656 columns. Hence the image captured by the CCD has an image size of 496 X 656 pixels. The resolution of the CCD is as small as few micrometers.

Each cell of the CCD array consists of a tiny photodiode along with a charge transfer area and shift register. When a photon strikes the silicon, an electron hole pair is generated. These photoelectrons are then collected in one of many discrete collecting sites over a fixed interval of time. An image is read out of the device by transferring the charge packets integrated at each collection site in parallel along electron conducting channels connecting columns of collection sites[8]. The time interval during which these photons are collected is the integration time of the CCD.

The NIR CCD imager has been built with the integration of Sensovation Samba QS-34 camera with a 6-position filter wheel. This filter wheel holds 6 filters that can be in the near infrared region. Along with these spectral filters, the optical assembly also

consists of a Navitar Zoom 7000 18-108 mm lens which is a close-focusing macro video lens (AVI-92-MS, Apogee Biodimensions user manual). This lens has been specifically designed to image objects with a size of 1" or smaller in diameter. Zoom 7000 offers 6X magnification power over a focal range of 18 to 108 mm.

The system is computer controlled and is equipped with a user interface to control data acquisition, filter wheel and integration time for each filter. During image acquisition, image data is sequentially acquired from each of the six filters and stored on the computer in tag image file format (TIFF). The minimum time required by the system to cycle through each of the filters is about 15 seconds and shows some variability depending upon the integration time set for each filter and other factors. This system is portable and can be easily mounted on an optical breadboard. Figure 1.3 below shows the principal components of the CCD imager system.

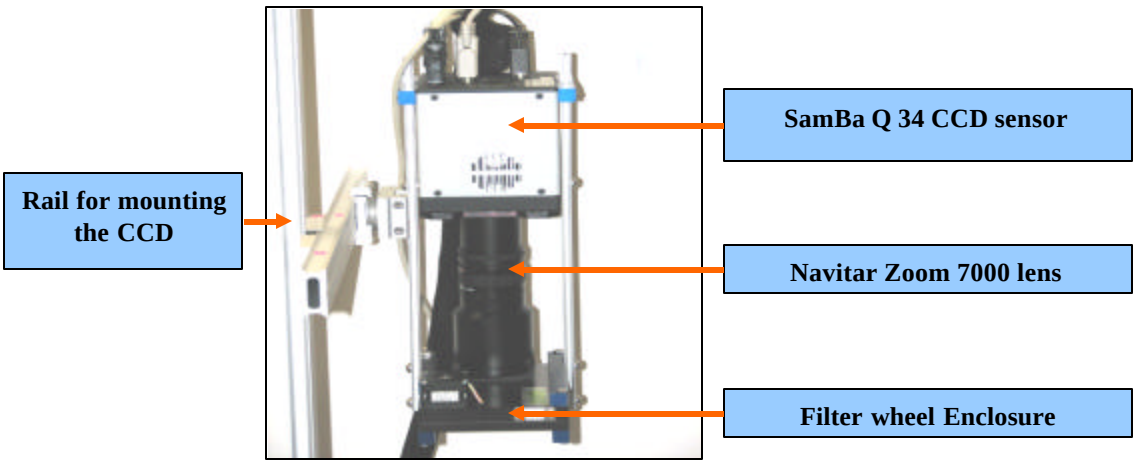

Figure 1.3: Principal components of CCD camera

1.2 Background of Prostate Cancer Study

1.2.1 Prostate Cancer

Prostate cancer is one of the most commonly diagnosed diseases among the men in North America. Of all the cases of cancer reported among men, 33% happen to be prostate cancer. It is estimated that, in the year 2006, there will be 2, 34,460 cases of prostate cancer with the 27,350 cases leading to death[9]. The prostate gland is a muscular, walnut sized gland that surrounds a part of the urethra. The prostate gland is a part of the male reproductive system, and its main function is to produce seminal fluid. It is located in front of the bladder and beneath the rectum. The urethra passes through the prostate gland. Any enlargement of the prostate gland results in obstruction of passage of urine and semen. Figure 1.4 below shows the general anatomy of the male reproductive tract.

Prostate cancer is caused by uncontrolled growth of cells in the prostate gland. This growth is called a tumor. These tumors can be malignant or benign. Malignant tumors can be highly metastatic and spread to other areas of the body through the lymph nodes and blood vessels. For tumor growth, a constant supply of blood is needed and this achieved through a process called as angiogenesis.

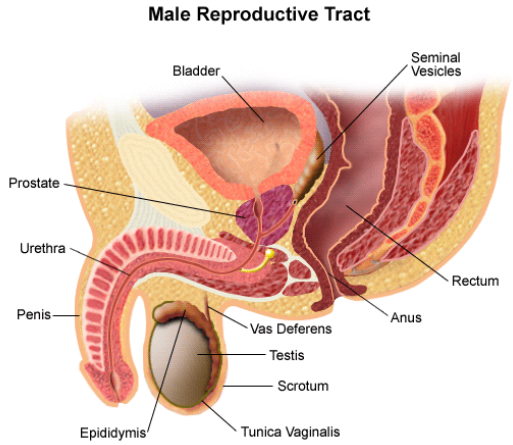

Figure 1.4: General anatomy of the male reproductive tract. (http://medicalcenter.osu.edu)

1.2.2 Angiogenesis

The process of recruitment of new blood vessels and capillaries is called as angiogenesis. Tumor growth is highly dependant on angiogenesis[10, 11]. Tumor cells produce specific angiogenic proteins which lead to recruitment of new blood vessels and capillaries in the tumors[10, 11]. Vascular Endothelial Growth Factor (VEGF), which is a mitogen and survival factor, is one of the major growth factor and promotes the development of angiogenesis in tumors and neovascularization[12]. One of the strategies used to suppress tumor growth is the use of chemotherapeutic agents and angiogenesis inhibitors. Cyclophosphamide, an alkylating and cytoxic chemotherapeutic agent, is known to exert anti-angiogenic effects[12]. Tumor growth is suppressed due to the anti-angiogenic effects caused by chemotherapy.

1.2.3 Tumor Hypoxia

Since tumor cells are proliferating at a much higher rate than normal endothelial cells, tumor vasculature is characterized by its irregular growth of blood vessels, leaky

vessel walls, blind ends and temporary occlusions [13]. Tumors generally exhibit high heterogeneity in its functional and morphological aspects. Some regions of the tumor are highly vascularized with a mesh of interconnected network of blood vessels while other regions are poorly vascularized with sparse capillary supply[14]. These poorly vascularized regions which are away from the network of blood vessels are prone to hypoxia occurring as a result of inadequate blood supply and lack of oxygen. Tumor hypoxia promotes the release of VEGF leading to neovascularization and development of blood vessels. Therefore, hypoxia further promotes the growth of tumor vasculature. Also hypoxic tumor is known to support metastasis and involves selection of cells with malignant phenotypes.

1.2.4 Effect of Tumor Hypoxia on Chemotherapy

The efficacy of therapeutic treatment is also affected by tumor hypoxia. Tumor cells require a constant supply to nutrients and oxygen for their growth through the medium of blood. Since the amount of blood reaching these hypoxic regions is less as compared to normal regions, therapeutic treatments show a decrease in efficacy. Because of the poor perfusion of blood vessels in the hypoxic regions, chemotherapeutic agents can hardly reach these regions through the blood vessels. Furthermore, as compared to normal tumor cells, hypoxic tumor cells are more resistant to radiation therapy [15], having poor response to photodynamic therapy (PDT) and to some chemotherapeutic agents.

1.3 Clinical Significance of Monitoring Tumor Hypoxia and Hemodynamics during Therapy

Tumor hypoxia can be used in predicting the response of the tumors to different therapies. Hence there is a clinical need to monitor tumor oxygenation levels. The therapeutic efficacy of treatment could be improved by increasing the tumor oxygenation levels. The oxygenation levels in the tumor can be increased by making the subject breathe pure oxygen (100 %) or carbogen (95 % O2, 5% CO2)[16, 17]. Changes in vascular oxygenation levels during gas intervention can be effectively monitored using NIRS.

Being non-invasive, cost effective and portable, NIRS is a useful clinical tool for monitoring dynamic changes in the tissue oxygenation levels. A multi-wavelength NIR CCD imager may be used effectively to monitor hemodynamics during chemotherapy for cancer and to get dynamic spatial maps showing the hypoxic regions and heterogeneity in the tumor vasculature. These maps could be beneficial in monitoring the efficacy of chemotherapy.

The overall goal of this thesis has two major parts: (1) to develop and characterize the multi-wavelength NIR CCD imager for imaging tissue hemodynamics and (2) to study its feasibility of monitoring hemodynamic changes in rat prostate tumors during chemotherapy regime.

CHAPTER 2

MATERIALS AND METHODS

2.1 Materials and Methods for Studying the NIR CCD Imager

2.1.1 Study of NIR CCD Imager

The NIR CCD imager system was custom designed and procured from Apogee Biodimension Inc (Silver Springs, MD). The NIR CCD imager consists of a six-position filter wheel with pre-loaded filters with center wavelengths of 680 nm, 720 nm, 760 nm, 780 nm, 820 nm and 840 nm. Each of these filters transmits light intensity at its center wavelength, and the corresponding image is captured by a two-dimensional, 12-bit CCD array. The filter wheel assembly casing can be easily accessed, and the filters can be replaced with other filters of desired wavelengths. The NIR CCD imager has a user interface, enabling to change the position of filter wheel. National Instruments Image Acquisition system (NI IMAQ) is used to control the CCD, acquire the images, and store them in the computer. The images can be acquired continuously using just one of the filters or sequentially through each of the six filters. To compute the hemodynamics, minimum of two wavelengths are needed. Hence for the purpose of this study, the imager system is used in the sequential mode. The images obtained from the CCD are stored in the uncompressed 'Tag Image File Format' (TIFF) with a 16-bit resolution. The size of each image is 656 X 496 pixels with a file size of 650 kilobytes. These high resolution images can be resolved to a size of few microns of the actual scene. The time taken by the filter wheel to complete one cycle is approximately 15-18

seconds, and this time varies depending upon the integration time set for the CCD. Tests were conducted to increase the acquisition rate of the CCD. Factors, such as processes that run on the computer operating system, were found to be affecting the image acquisition time. Also, image size affects the acquisition rate of the system. By reducing the size of the image acquired, the acquisition rate can be improved to a certain extent.

2.1.2 Phantom Studies to Understand Light Propagation

Diffusion of light through the tumor tissue can be simulated by means of laboratory phantoms. It is imperative to understand how light diffuses and propagates through the tumor vasculature before being captured by the CCD. A laboratory phantom simulating optical properties of the tissue was made and used for the purpose of this study, as shown in Fig. 2.1(a). The phantom used a cylindrical plastic container filled with an Intralipid (Baxter 20% Intralipid, IV fat emulsion) solution diluted from 20% to 0.5% - 1.5%, yielding optical properties similar to those of tissue [1]. A tungsten halogen light source (Illumination Technologies, Inc) with quad fiber guide was used to transmit light through the phantom. The tip of the light-delivering fiber was placed on the side of the container at a depth of 0.5-2.5 cm from the top surface of the Intralipid solution. The CCD imager system was mounted above the phantom and focused on the surface of the Intralipid to image the photons diffusing through the Intralipid solution and being captured by the CCD. The images were acquired at all the wavelengths and were analyzed using MATLAB™. Figure 2.1(b) below shows the setup of the phantom experiment.

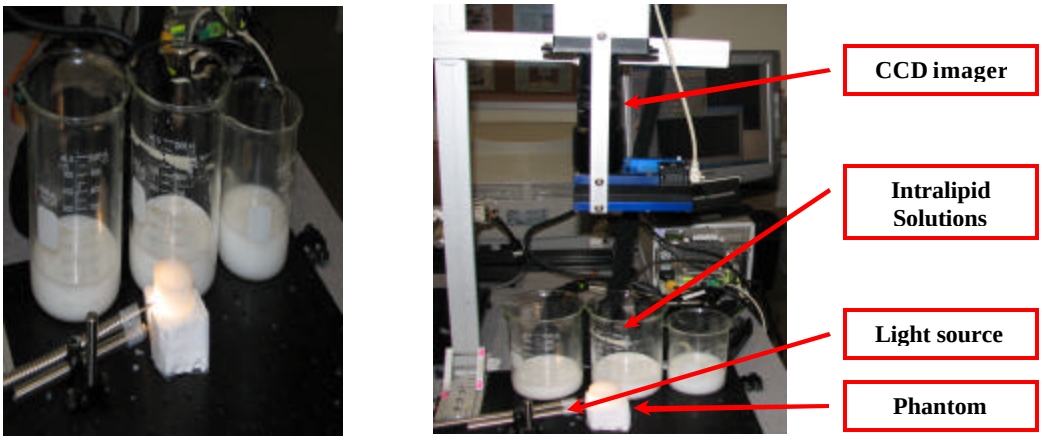

(a) (b)

Figure 2.1: (a) Phantom (b) Experimental setup for phantom study

To simulate the effect of absorption in the tissue, a very small amount of absorber in the form of Bombay black ink was mixed in the Intralipid solution, and the images were captured. To study the effect of change in depth of the light source and concentration of the Intralipid on image formation, different concentrations of Intralipid were used and images acquired for each concentration of Intralipid with change in depth. The concentrations of Intralipid used were 0.5%, 1% and 1.5%. For each concentration of the Intralipid, the depth of the light source from the surface of the container was varied, and images were acquired.

2.1.3 Data Processing and Analysis

The images for phantom studies were processed using MATLAB™. Images at one wavelength (720 nm) were selected, and threshold operation was performed to understand the propagation of light through the phantom. The brightest region in the Intralipid solution of the phantom was determined, and the distance between the light source and center of the bright region was calculated to understand the variation in

diffusion pattern with respect to change in separation of the light source from the top surface of Intralipid.

2.2 Materials and Methods for Monitoring Hemodynamics in Tumor

2.2.1 Prostate Tumor Animal Model

Adult male Copenhagen rats (5-6 weeks old, 200-300 gm, Harlan, Indianapolis, IN) were used for the purpose of this study. Dunning R 3327 AT3.1 rat prostate carcinoma cell line was used to grow tumors in Copenhagen rats. The cell line was originally obtained from Dr. J.T Isaacs (Johns Hopkins University, Baltimore, MD) through American Type Culture Collection (ATCC). The cells were cultured in a culture medium consisting of Dulbecco's Modification of Eagle's Medium (DMEM) supplemented with 10% Fetal Bovine Serum (FBS). After culturing, the cells were injected subcutaneously in the skin pedicles in the foreback of Copenhagen rats [1, 13, 19, 20, 21]. The concentration of cells injected was 1 million cells ($1 \text{ X } 10^6$) in 0.1 ml of media. These animal models were developed and provided by Drs. Jinhui Shen and Liping Tang (Department of Bioengineering, University of Texas at Arlington (UTA)) at the UTA animal vivarium. After the injection, the time required for the tumor to grow was approximately 7 to 10 days. The region where the cells were injected was shaved to allow easy monitoring of tumor progression. Vital parameters like body weight and tumor size were monitored on a daily basis. All experiments have been conducted under the strict regulation of IACUC (Institution for Animal Care and Use Committee) of the University of Texas at Arlington.

2.2.2 Gas Intervention and Anesthesia Setup

The rodent gaseous anesthesia unit (NLS Animal Health, OK) with anesthesia induction chamber was procured and used for the purpose of this study. Isoflurane was used as an anesthetic agent to induce anesthesia in rats. To monitor changes in the tumor oxygenation and hemodynamics, gas intervention was used. Air (21% O_2) and oxygen (100% O_2) were used for gas intervention. The schematic diagram for the gas intervention setup is shown in Fig. 2.2 below.

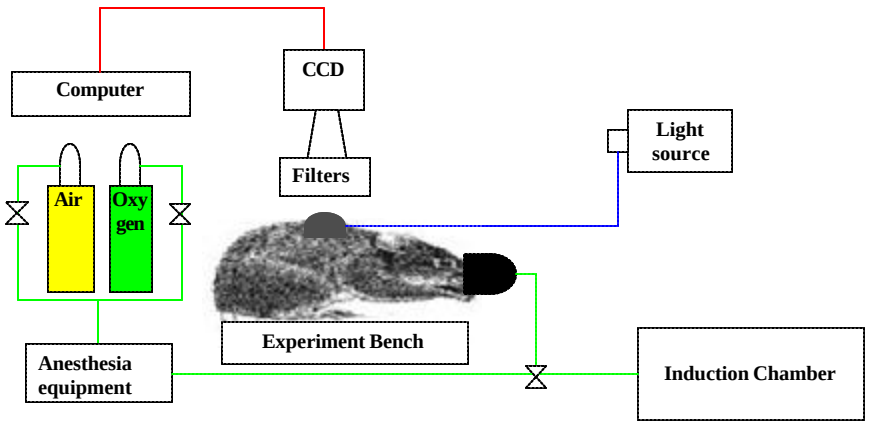

Figure 2.2: Experimental setup to monitor hemodynamic changes of rat prostate tumor during gas intervention

Air and oxygen cylinders were connected to the anesthesia unit through valves. The gas was mixed with isoflurane from the anesthesia unit and transformed into an anesthetic component. Using valves, this anesthetic gas can either be routed to the induction chamber or to the rodent mask placed on the experiment bench. The animal to be anesthetized was placed in the induction chamber. The rat inhaled 3% isoflurane in air at a flow rate of 1 dm^3/min. After the induction of anesthesia, the rat was placed on the experiment bench, and a gas mask was placed on its mouth and nose. The rat

inhaled 1.3% isoflurane in air at a flow rate of 1 dm^3/min to maintain the state of anesthesia till the end of the experiment.

2.2.3 Monitoring of Vital Parameters and Temperature Regulation

A thermal blanket with a control unit (Harvard Apparatus, Inc., Holliston, Massachusetts) was placed on the experimental bench to keep the rat warm during the course of the experiment. The body temperature of the rat was continuously monitored and maintained at 37°C using a rectally inserted thermal probe and a control unit. The animal's pulse oxygen saturation (S_pO_2) was continuously monitored during the entire course of the experiment using MouseOx™ (STARR Life Sciences, PA), which can record the pulse rate, pulse distention, and respiratory rate, besides serving as a pulse oximeter. The MouseOx utilized a sensor clip and was placed on the hind paw of the rat. Using the MouseOx software, the vital parameters were continuously monitored and data was logged (see Fig. 2.3).

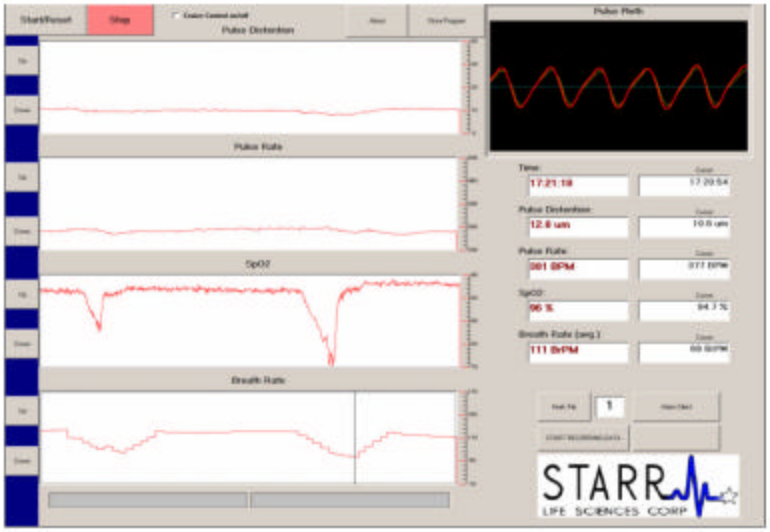

Figure 2.3: Graphical user interface of MouseOx

2.2.4 Drug and Treatment Protocol

Prostate tumors were implanted in adult male Copenhagen rats as described in section 1.2.1. Chemotherapeutic treatment was initiated when the tumors were approximately 1 cm in diameter [21]. A total of 17 rats were used for this study. These rats were divided into 3 groups. Group 1 (n = 6) was the untreated control group in which no therapy was administered. Group 2 (n = 6) was administered with a daily low dose of Cyclophosphamide (Sigma Chemical Co., St. Louis, MO) of 30 mg/kg intraperitoneally (i.p.) prepared by dissolving Cyclophosphamide in sterile phosphate buffered saline (PBS) with continuous stirring and heating the solution to 37^{o}C. Group 3 (n = 5) was administered with a single high dose of 200 mg/kg of cyclophosphamide in sterile PBS injected intraperitoneally. All the animals were monitored on a daily basis and were sacrificed when the animal lost 20 % of its original body weight, or the animal stopped grooming, or the tumor volume exceeded 20 % of the body mass of the animal. Tumor size and body weight of the animal were recorded on a daily basis for all animals. The tumor vasculature was not perfectly spherical, but rather slightly ellipsoidal. The tumor volume was calculated as (p /6)abc where a, b, c are the three axial dimensions of the tumor.

2.2.5 Monitoring of Tumor Hemodynamics during Chemotherapy

The rat was anesthetized and placed on the experiment bench using the procedure as described in section 1.2.2. The tumor region was shaved to facilitate transmission of light through the tumor vasculature and to improve detection of the transmitted light by the NIR CCD imager. The experiments were performed in a dark

room. A single fiber bundle connecting to the light source was placed on the periphery of the tumor vasculature to diffusively illuminate the tumor vasculature. The CCD imager was mounted on the top and focused on the tumor bearing region (see Fig. 2.4). The MouseOx sensor clip was attached to one of the hind paws and vital data was continuously acquired during the entire course of the experiment.

The rat inhaled air for the first 10 minutes to get a stable baseline. After the baseline taken, the gas was switched to oxygen for the next 10 minutes. After oxygen inhalation, the gas was again switched to air for the last 10 minutes. The images were continuously acquired by the CCD imager system during the gas intervention to determine the hemodynamic changes occurring as a result of the gas perturbation. The acquisition rate was about 15-18 seconds per data point. These images were then processed to quantify the hemodynamic changes in the tumor and to understand the heterogeneity in the tumor vasculature.

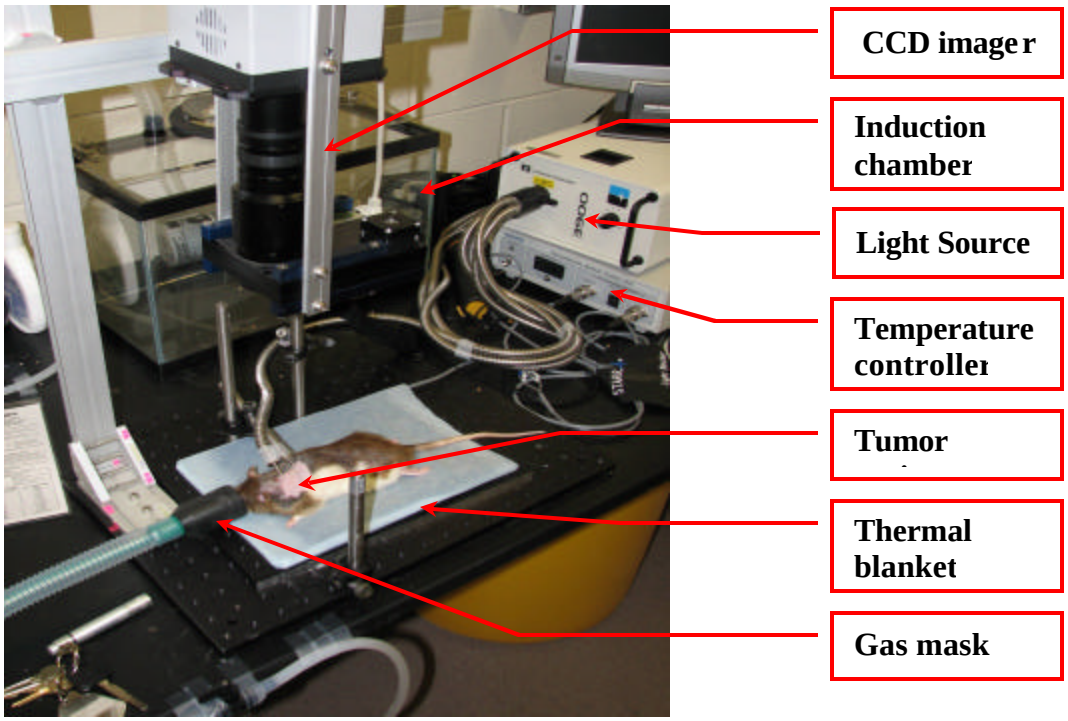

Figure 2.4: Experimental setup to monitor hemodynamic changes during gas intervention

2.2.6 Data Processing and Analysis

To compute the hemodynamic changes in the tumor vasculature during gas intervention, acquired images were processed using MATLAB™. Images at wavelength 720 nm (filter 2) and 820 nm (filter 6) were used. Equations (1.5), (1.6), and (1.7) in section 1.1.1 give the relative changes in oxygenated, deoxygenated and total hemoglobin concentration, respectively. Wavelength of 720 nm represents l_1 and wavelength of 820 nm represents l_2. Table 2.1 below gives the specific extinction coefficients of oxygenated and deoxygenated hemoglobin of rat at the respective wavelengths [26].

Table 2.1: Extinction coefficients of rat blood at 720 nm and 820 nm

Wavelength (nm)	e [HbO_2]	e [Hb]
720	4.668	6.579
820	8.115	5.206

The extinction coefficients and images obtained at 720 nm and 820 nm were substituted in equations (1.5) to (1.7) to give topographic maps, showing regional dynamic changes in oxygenated, deoxygenated, and total hemoglobin concentrations within the rat prostate tumors during gas intervention. The mean of these topographical maps was computed and plotted with respect to time in order to see the dynamic changes in tumor hemodynamics. Vital physiological data (i.e., pulse oximetry) obtained from MouseOx was also plotted to observe the arterial oxygenation trends of the rats during the entire experiments.

CHAPTER 3

RESULTS

3.1 Study of NIR CCD Imager

3.1.1 Light Propagation through Intralipid

It is known that photon migration in the tissue occurs in a banana shaped pattern [22, 23]. To characterize the CCD imager and understand light propagation in tissue, an Intralipid phantom was used. Light was delivered into the phantom from side in transmittance geometry as shown in figure 2.1. The integration time, separation between the phantom and CCD, and the intensity of light source were kept constant throughout the experiment. Using the image below in Fig. 3.1, the pixel scale of the image was converted to distance measurable in millimeters.

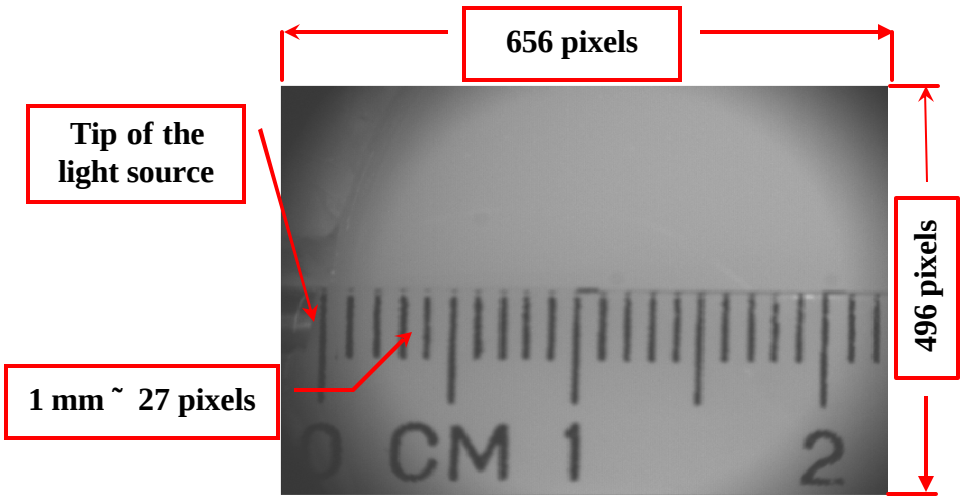

Figure 3.1: CCD image showing the image scale in mm

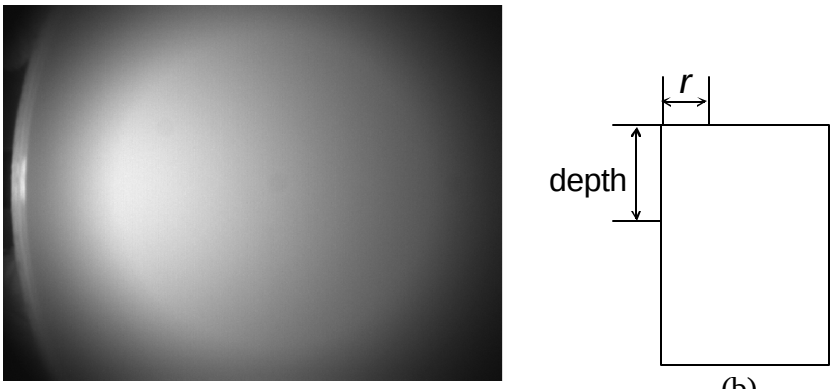

(a) (b)

Figure 3.2: Raw image obtained from the tissue phantom: (a) raw image, (b) illustration of distance from edge of container and depth of light source.

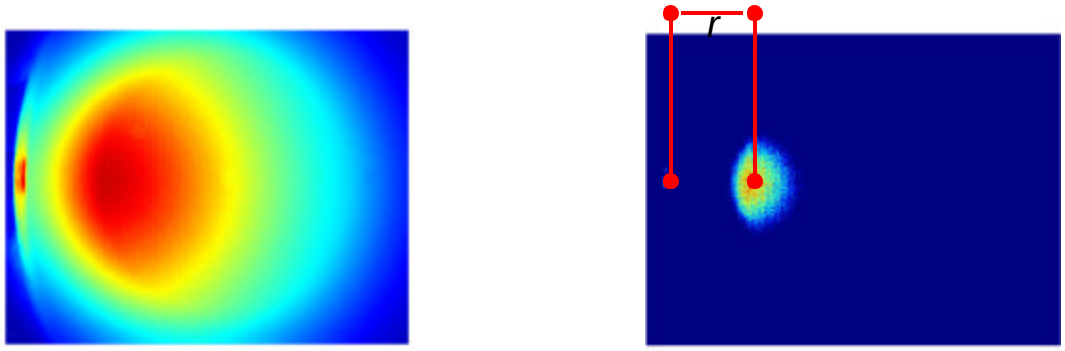

(a) (b)

Figure 3.3: Images obtained after applying: (a) colormap and, (b) threshold to Figure 3.2 to determine the distance of the brightest spot from the edge of the container.

Figure 3.3(a) shows the image obtained after applying colormap to the raw image in Figure 3.2(a). Figure 3.2(b) shows the geometry for the light source and the phantom. Thresholding was performed and the location of the area with highest density of photons (brightest spot) was determined, as given in Fig. 3.3(b), where '*r*' shows the distance of the brightest spot from the edge of the Intralipid phantom container (also see Fig. 3.2(b)).

To comprehend the effect of change in depth of light source and concentration of Intralipid on photon migration pattern, Intralipid concentration and depth of light source were varied. Intralipid of 0.5%, 1% and 1.5% concentration were used and the depth of the light source was varied from 5 mm to 25 mm with increments of 5 mm. The phantom serves as a finite medium in which the photons diffuse and migrate in a banana shaped pattern. Results obtained for different concentrations of Intralipid are plotted below in Figures 3.4, 3.5 and 3.6 to show the dependence of distance, r, and the depth of light source. The bright spot on the surface of Intralipid corresponds to the location of highest density of photons, the distance, r, represents the length from this spot to the edge of the container. From Figs. 3.4 to 3.6, it can be seen that the distance, r, increases with increase in depth of the light source from the top of the container in all three cases with Intralipid concentrations of 0.5%, 1.0%, and 1.5%. However, the slopes of the fitted lines do not vary much for all three curves (all near 0.5). This implies that the distance, r, does not greatly depend on light scattering of the phantom.

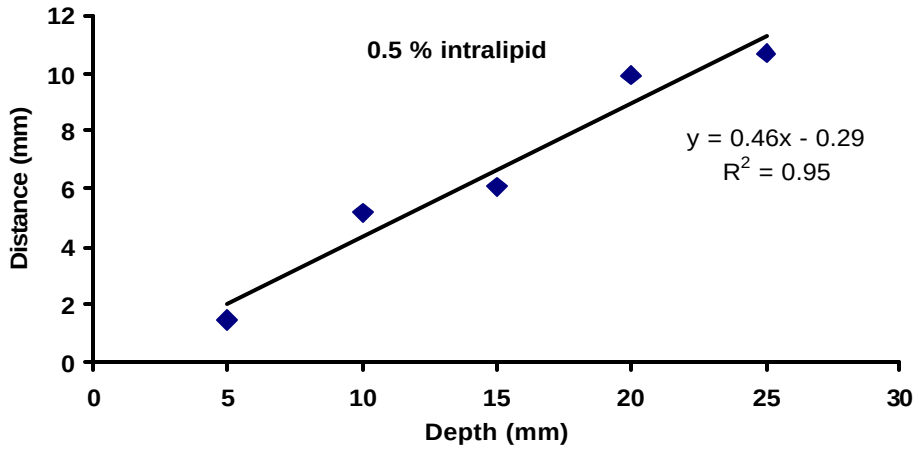

Figure 3.4: Graph showing the variation of the distance of the bright spot with depth of the light source for 0.5 % Intralipid solution

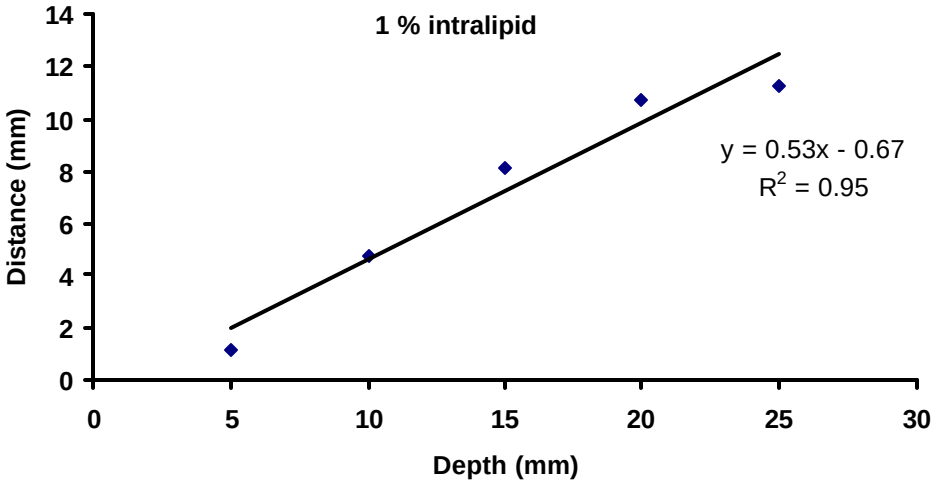

Figure 3.5: Graph showing the variation of the distance of the bright spot with depth of the light source for 1 % Intralipid solution

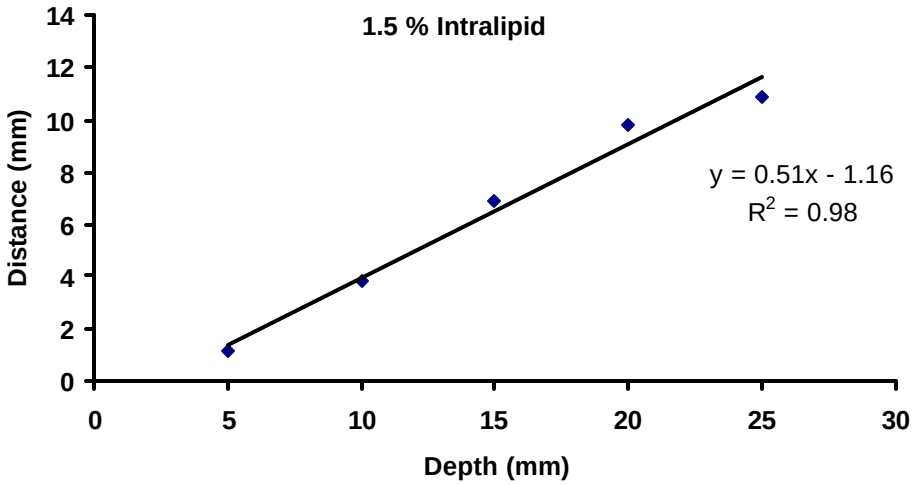

Figure 3.6: Graph showing the variation of the distance of the bright spot with depth of the light source for 1.5 % Intralipid solution

3.2 Path Length Correction Mask

To estimate the relative changes in hemodynamics, the optical path length, i.e. the distance traveled by photons between the source and detector, should be known and is equal to the product of source-detector separation and a factor, i.e., the differential

pathlength factor (DPF), of the tissue. As an approximation, DPF may be assumed to be a constant in this study, where we focus on hemodynamic changes during gas intervention and the DPF should remain constant. In previous studies [1, 19] with the single-channel spectrometer, the optical path length was assumed to be fixed because of the single source-detector geometry. In case of the CCD imager, however, the situation becomes more complex: each pixel of the 2-dimensional array acts as a detector, and the source-to-detector distances vary for different pixels. Hence, the distance of each detecting pixel from the light source depends on the individual locations of the pixels and depth of the light source.

Since the physical dimensions of the image under probation are known, the source-to-pixel distances can be calculated. based on the location of the light source, a path length mask can then be generated and used in equations (1.5), (1.6) and (1.7) to estimate the change in hemoglobin concentration, while the DPF will be used as a part of unit [7,13,19]. This mask is a function of the image coordinates (x, y) and the depth of the light source, z. The magnitude of the mask at the pixel location (a, b) is given by

$$I = \sqrt{(a^2 + b^2) + z^2}\ , \tag{3.1}$$

where, 'a' and 'b' are the coordinates of the pixel in mm and 'z' is the depth of the light source in mm. A path length mask for an image of 15 mm X 10 mm with light source at a depth of 10 mm is shown in figure 3.7 below.

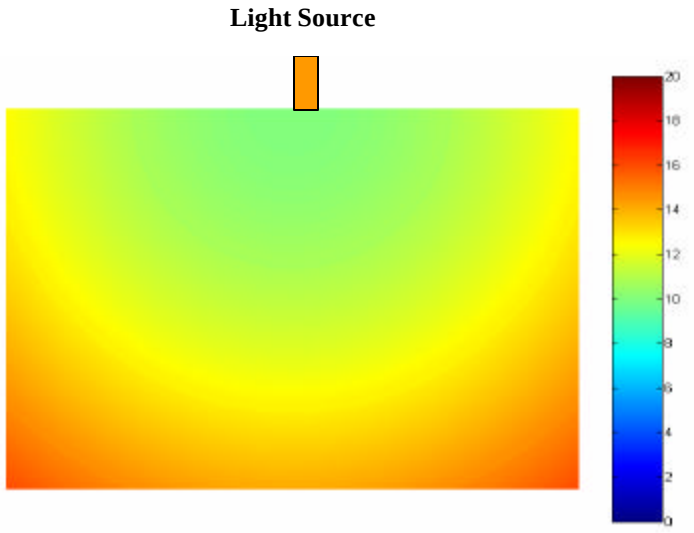

Figure 3.7: Map of path length correction factor (or path length correction mask)

By knowing the physical dimensions of the image, position and actual depth of the light source, such an optical path length correction mask needs to be generated for each experiment in calculation of hemodynamic concentrations in equations (1.5) to (1.7). Figure 3.8 shows a comparison of two images (at 720 nm) with corresponding profiles across the central image of Intralipid surface with and without path length correction. Fig. 3.8(a) was obtained by dividing an image of Intralipid phantom without ink by an Intralipid phantom with ink and taking the logarithm of the resultant image. Mathematically, this is written as:

$$I = \log(\frac{I_o}{I_T}), \tag{3.2}$$

where 'I' is the optical density, 'I_o' is the image of Intralipid without ink and 'I_T' is the image of Intralipid with ink. Fig. 3.8(b) which shows the corrected image is

obtained by dividing Fig. 3.8(a) by the correction mask matrix. Fig. 3.8(c) gives the profile across the uncorrected OD image (Fig. 3.8(a)) and Fig. 3.8(d) gives the profile across the pathlength corrected OD image (Fig. 3.8(b)).

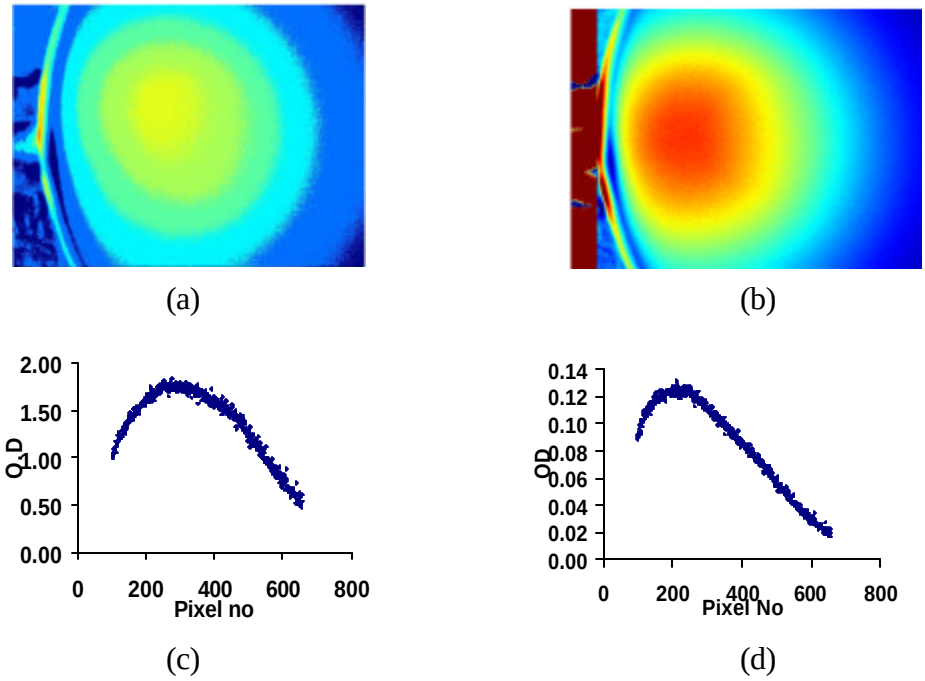

Figure 3.8: Effects of path length correction mask: (a) uncorrected OD image, (b) corrected OD image, (c) a central profile across uncorrected image, (d) a central profile across corrected image.

3.3 Effect of Variation in Concentration of Intralipid and Depth of Light Source

The concentration of the Intralipid affects the scattering properties of the solution. The higher the concentration of the Intralipid, the more is the number of scatterers in the medium. These scatterers affect the photon migration path. To study the effect of variation of concentration on image formation and photon migration path, for each depth of the light source, the concentration of Intralipid in the phantom was varied and images were acquired. Since data on the tumor is collected in the

transmittance mode, i.e. light source is placed on the side of the tumor and photons are forced through the tumor vasculature, the phantom experiment was designed to study the images in the transmittance mode. The images taken without ink are represented by Io and those with ink are represented by I_T. The quantity of O.D. is the resultant image (also labeled as I) showing the change of Io with respect to I_T, as given:

$$\text{O.D.} = I = \log (I_o/I_T) = \varepsilon cL = \varepsilon c d \, \text{DPF}, \tag{3.3}$$

where ε is the extinction coefficient of ink, c is the concentration of ink, and L is the path length and equal to the product of source-detector separation, *d*, and DPF. The images of optical density per DPF with inclusion of the path length correction mask for different concentrations of Intralipid at varying depths are given in the following graphs and images. Specifically, Figs. 3.9 to 3.12 correspond to the images taken at 0.5% Intralipid concentration with the source depths of 10, 15, 20, and 30 mm; Figs. 3.13 to 3.16 are from the Intralipid concentration of 1.0% at the respective depths; Figs. 3.17 to 3.20 show similar OD images taken from 1.5% Intralipid solution at the respective source depths.

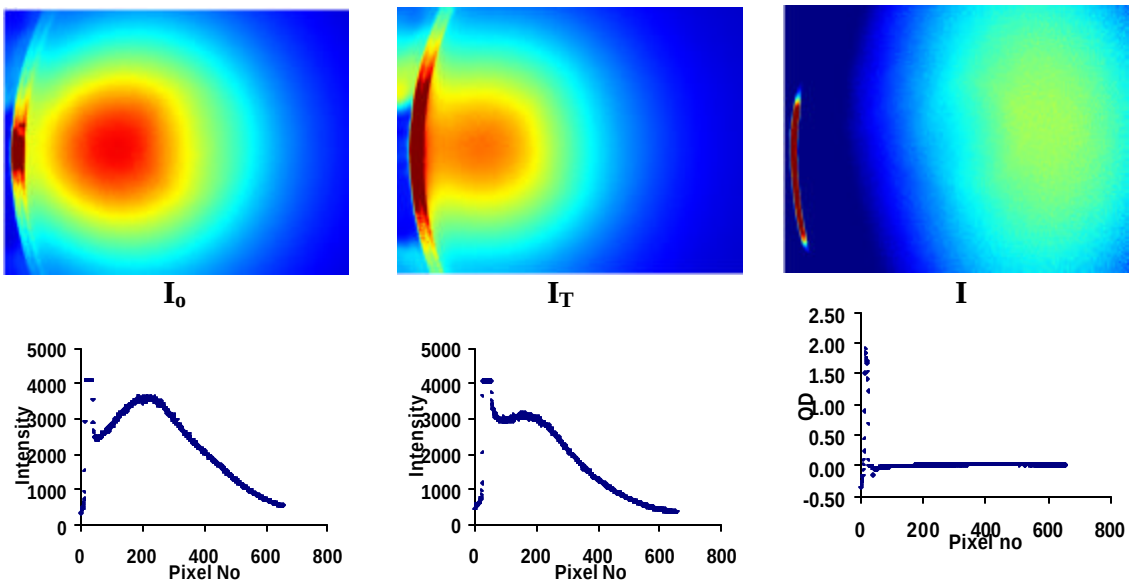

Figure 3.9: Images obtained for 0.5% IL with light source at a depth of 10mm.

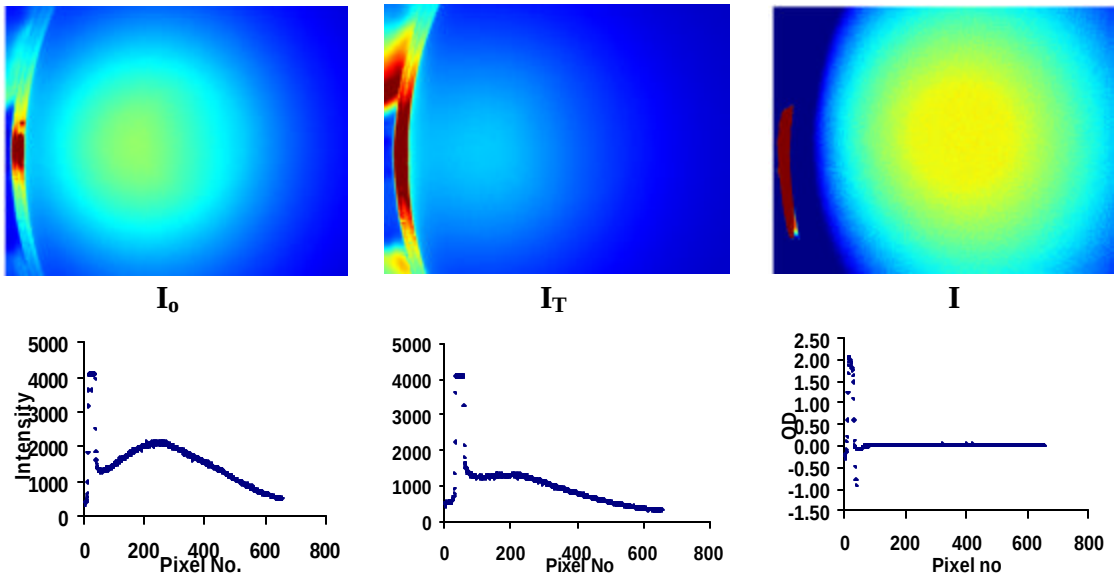

Figure 3.10: Images obtained for 0.5% IL with light source at a depth of 15mm.

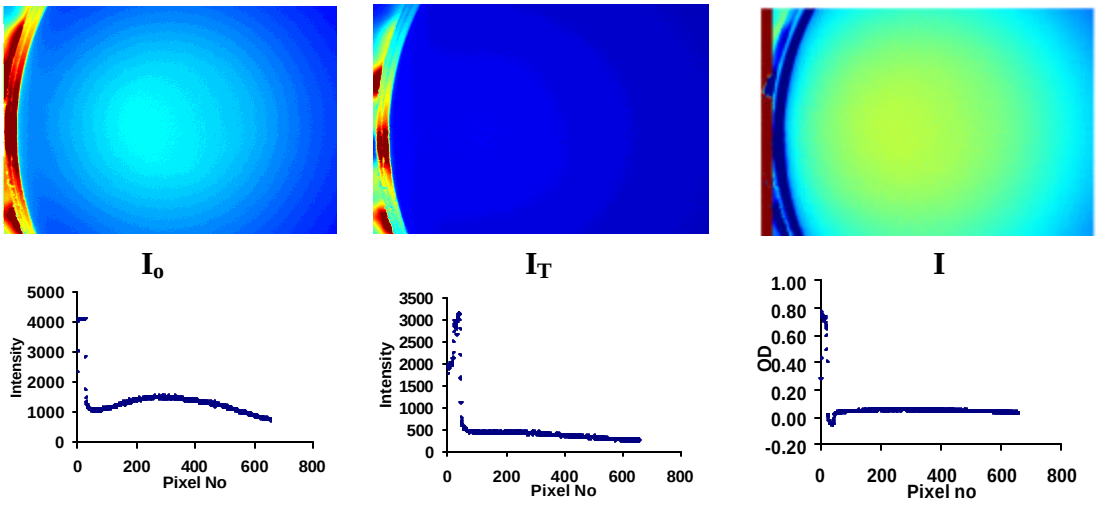

Figure 3.11: Images obtained for 0.5% IL with light source at a depth of 20mm.

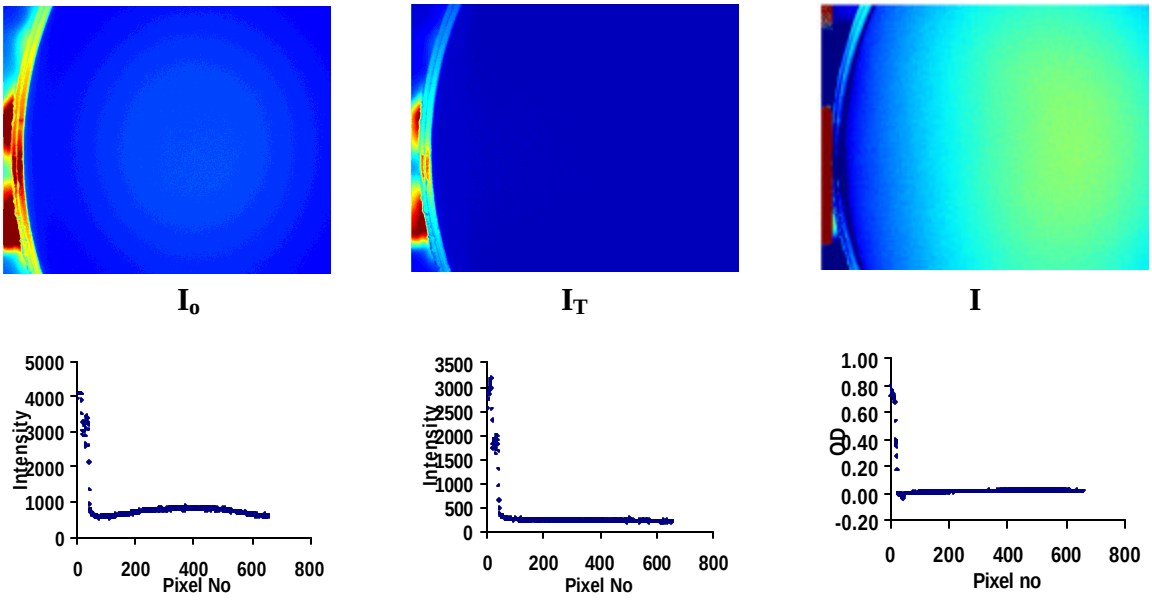

Figure 3.12: Images obtained for 0.5% IL with light source at a depth of 30mm.

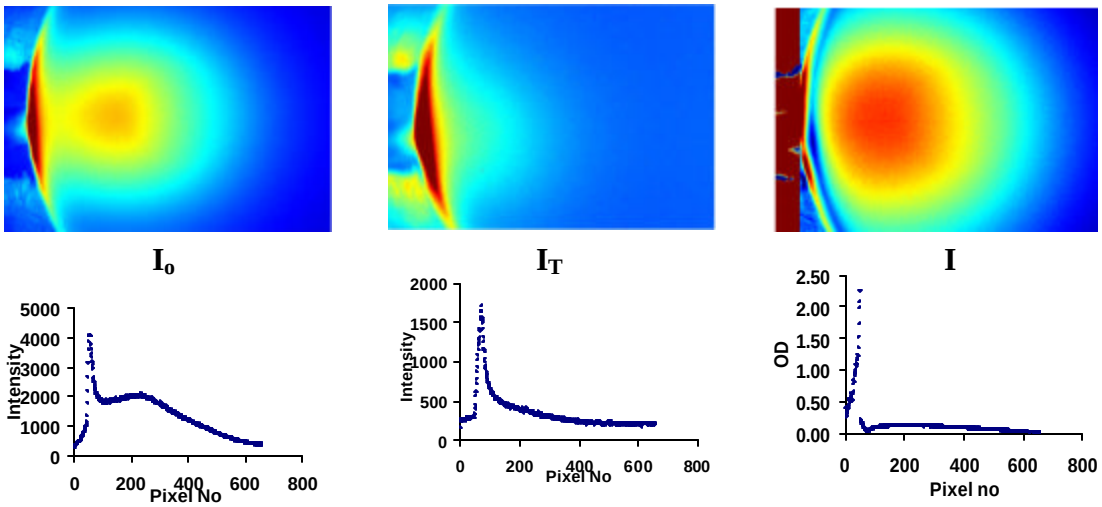

Figure 3.13: Images obtained for 1% IL with light source at a depth of 10mm.

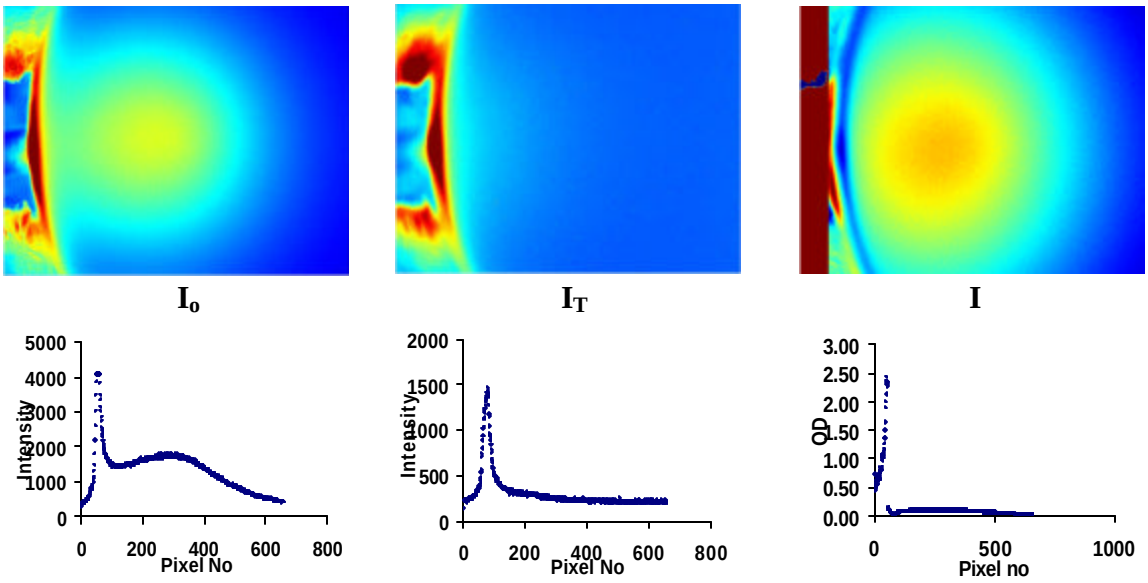

Figure 3.14: Images obtained for 1% IL with light source at a depth of 15 mm.

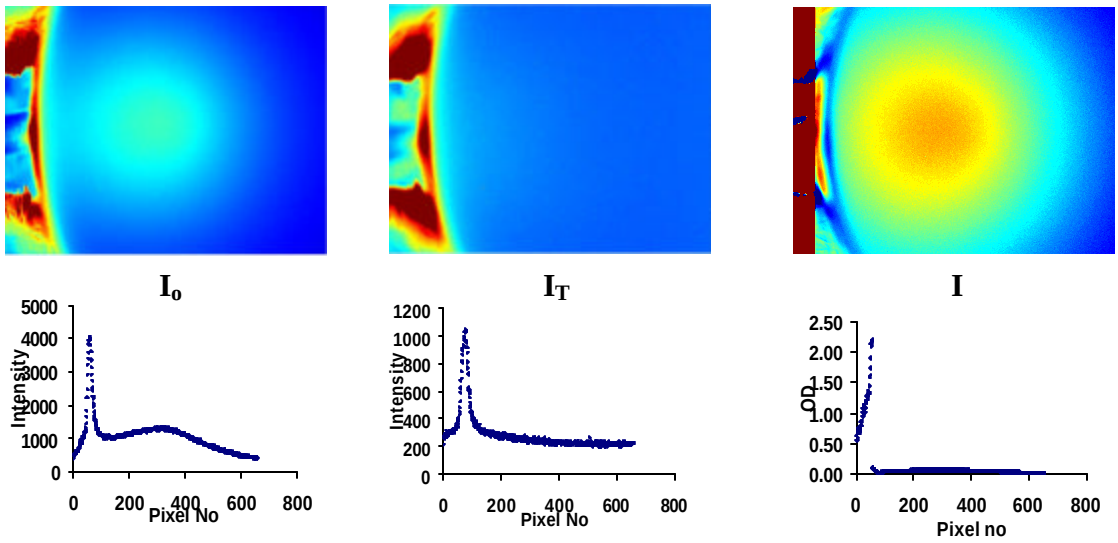

Figure 3.15: Images obtained for 1% IL with light source at a depth of 20 mm.

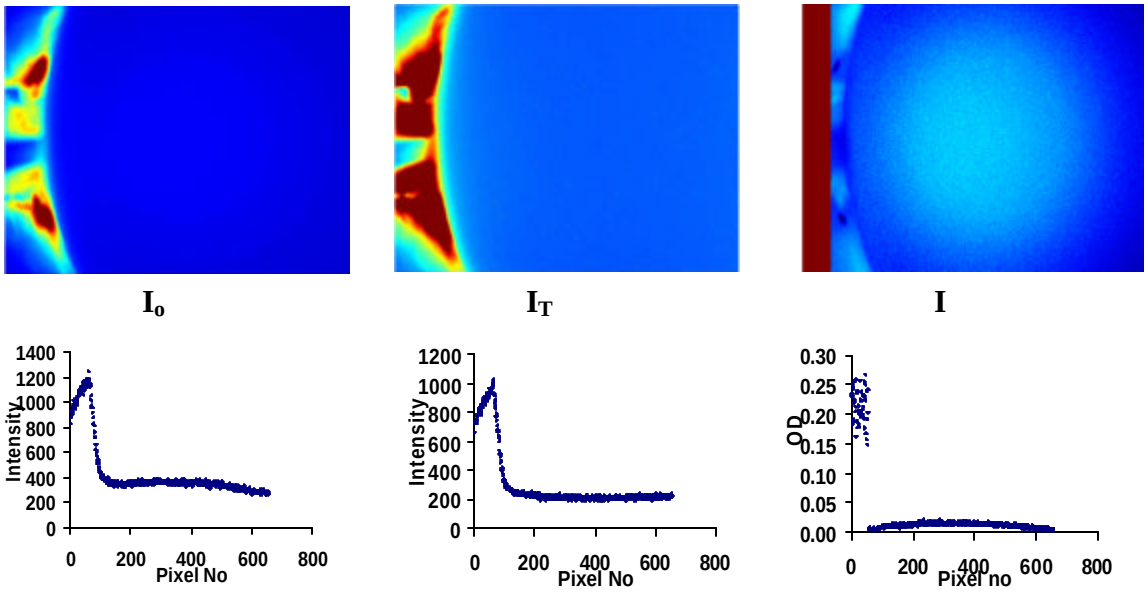

Figure 3.16: Images obtained for 1% IL with light source at a depth of 30 mm.

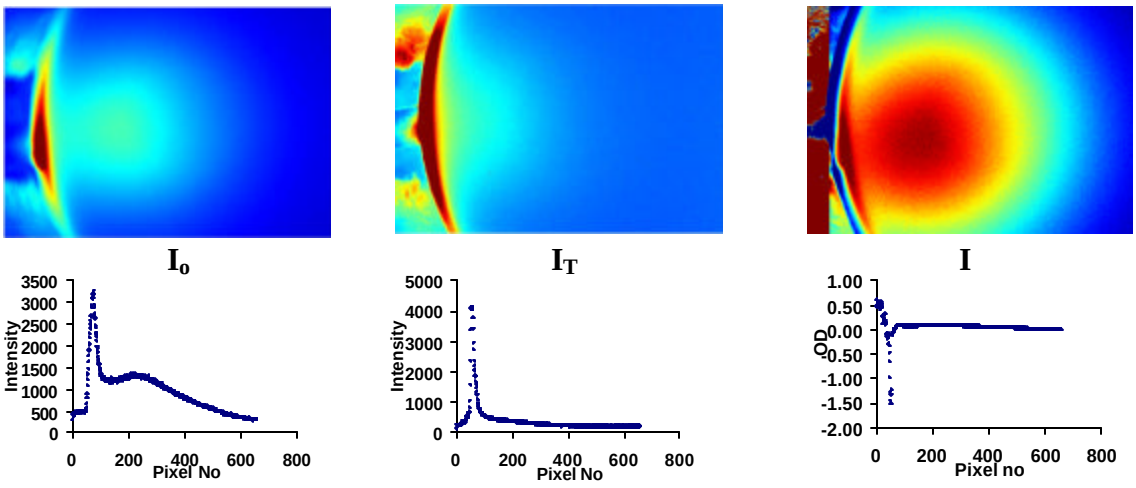

Figure 3.17: Images obtained for 1.5% IL with light source at a depth of 10 mm.

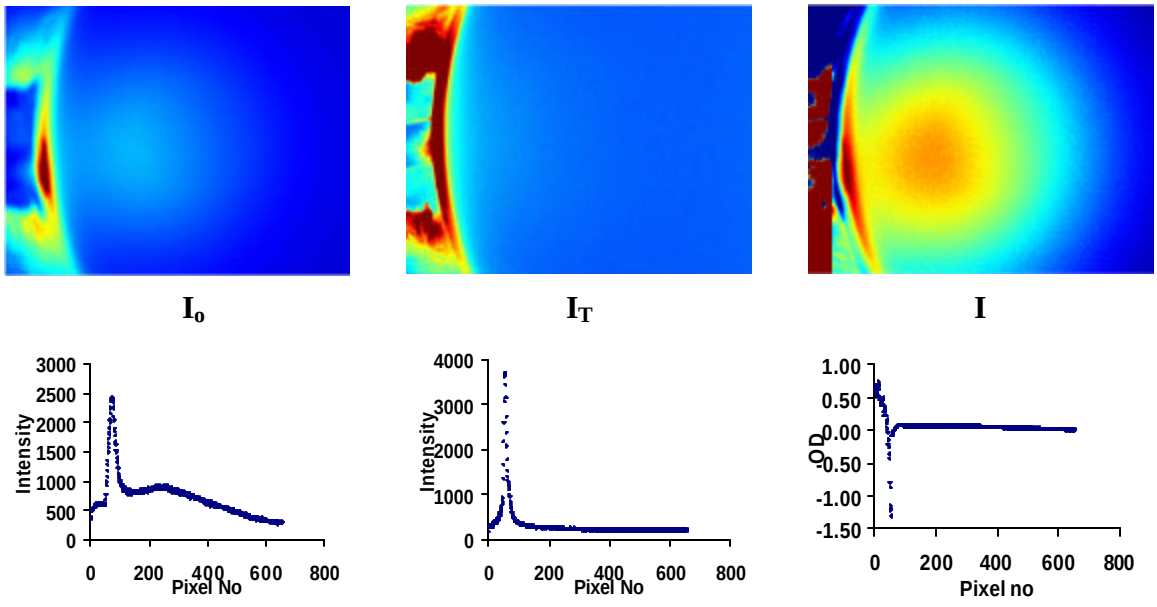

Figure 3.18: Images obtained for 1.5% IL with light source at a depth of 15 mm.

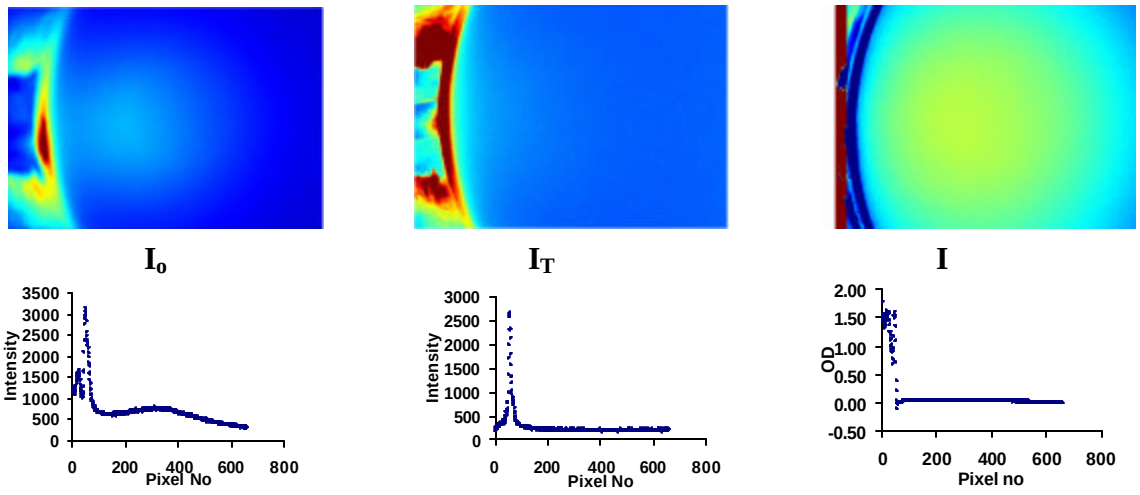

Figure 3.19: Images obtained for 1.5% IL with light source at a depth of 20 mm.

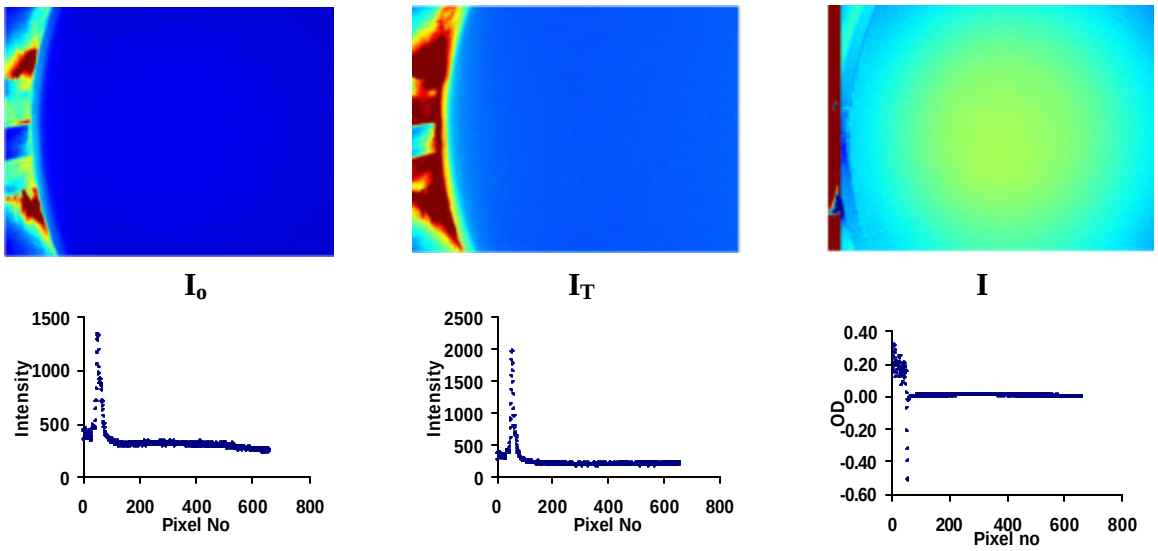

Figure 3.20: Images obtained for 1.5% IL with light source at a depth of 30 mm.

3.4 Profiles of Optical Density Plots at Different Depths and Varying Intralipid Concentrations

The optical density curves across the image at different source depths for each concentration of the Intralipid are plotted below; namely, these plots show the intensity distribution across the center line of each CCD image at different source depths. Although the magnitude of change in optical density is small, these plots provide useful information about photon propagation through Intralipid and effect of variation in depth of the light source. Figs. 3.21, 3.22, 3.23 and 3.24 show the effect of variation in Intralipid concentrations at depths of 10mm, 15mm, 20mm and 30mm, respectively. These profiles across the center image show the corresponding variation in optical density (OD) and the OD values have been normalized for comparison. Figs 3.25, 3.26 and 3.27 show the effect of variation in depth of light source for Intralipid concentrations of 0.5%, 1% and 1.5%, respectively. From these figures, it is seen that non-uniformity exists in the spatial distribution of the optical density plots.

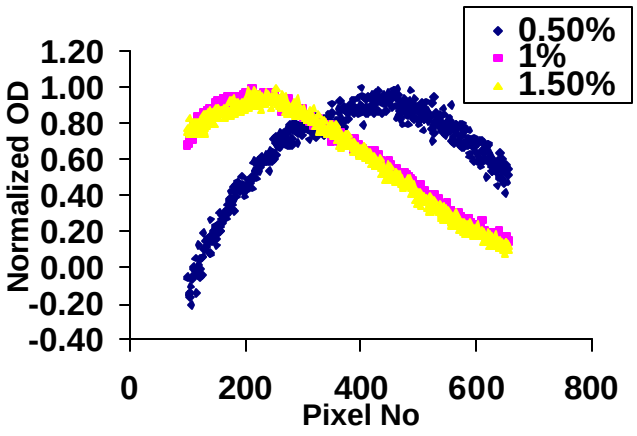

Figure 3.21: Optical profile for different Intralipid concentrations at 10 mm depth

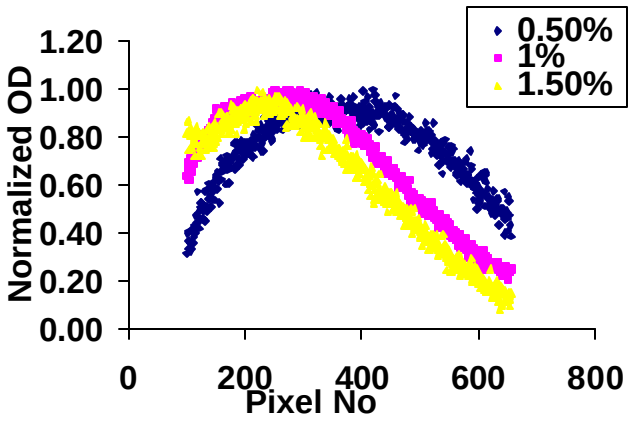

Figure 3.22: Optical profile for different Intralipid concentrations at 15 mm depth

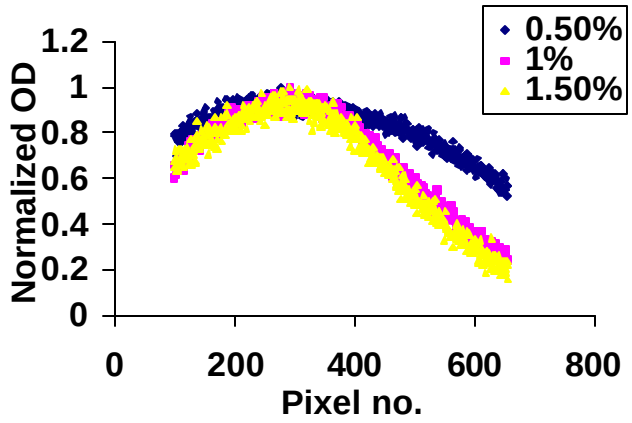

Figure 3.23: Optical profile for different Intralipid concentrations at 30 mm depth

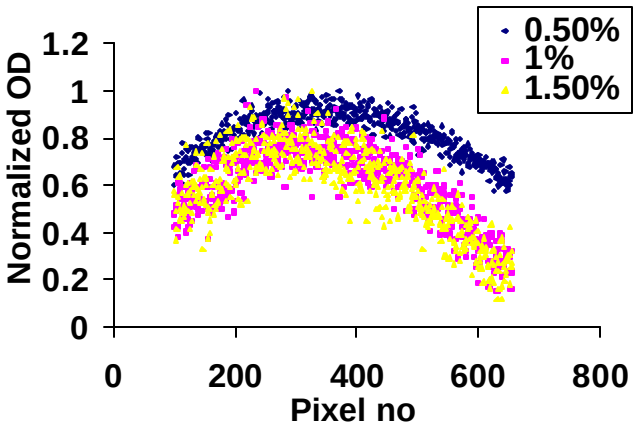

Figure 3.24: Optical profile for different Intralipid concentrations at 30 mm depth

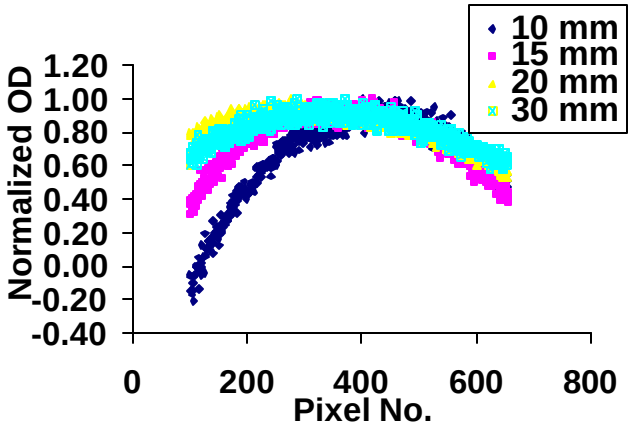

Figure 3.25: Optical profiles at different depths for 0.5% Intralipid

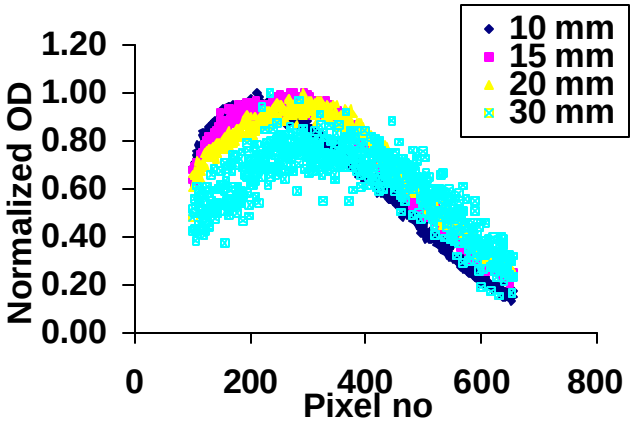

Figure 3.26: Optical profiles at different depths for 1% Intralipid

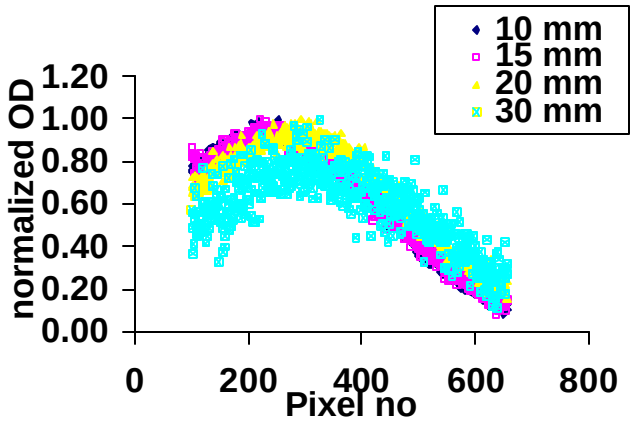

Figure 3.27: Optical profiles at different depths for 1.5% Intralipid

The above graphs show the variation due to change in depth of the light source. The photon migration path varies with change in depth of the light source as well as the concentration of Intralipid. To understand the non-uniformity issue, I investigate the imager system itself in the next sub-section and further discuss it in the following chapter.

3.5 Effect of Optics on the CCD in Reflectance Mode

The optical lenses and filters mounted in front of the CCD array contribute to the inhomogeneity and may have some effects on the image formation. To study the intensity distribution across the CCD array under static homogeneous conditions in reflectance mode, a homogenous, flat, white calibration sample (Ocean Optics Inc) was placed in the field of view of the system. The calibration sample, which is uniform and homogeneous with 99.9% reflectance, was illuminated uniformly by a tungsten light source. To ensure homogeneous illumination, the light source was placed at a sufficiently large distance from the sample. The image obtained is shown below in figure 3.28 (a). A profile of one row of pixels along the center is shown in figure 3.28(b). The ring-like structure in Figure 3.28(a) and the Gaussian-like distribution seen in Figure 3.28(b) reflect the non-uniformity in the spatial distribution of light intensity. Because of uniform light illumination and the homogeneous sample, the non-uniform light distribution may be attributed to the optics of the CCD imaging system.

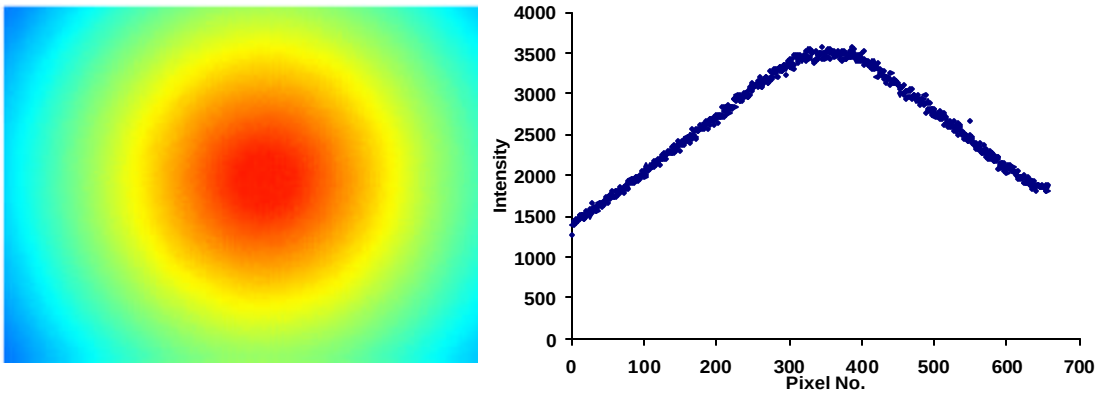

(a) (b)

Figure 3.28 a) Image obtained from calibration sample. (b) Profile of row across the center of image.

3.6 Results of Chemotherapy

As described in section 1.2.4, animals in low dose and high dose groups were administered chemotherapy while the animals in control group were not administered any form of chemotherapy. The body weight of the animal and tumor dimensions were monitored on a daily basis, and normalized tumor volume and body weights are shown in Figs. 3.29, 3.30 and 3.31 below. The error bars in these figures are plotted using the standard deviation. Chemotherapy and hemodynamic monitoring of tumor using NIR CCD imager was started when the tumor grew to a size of approximately 1 cm in diameter. This day was considered as day 1.

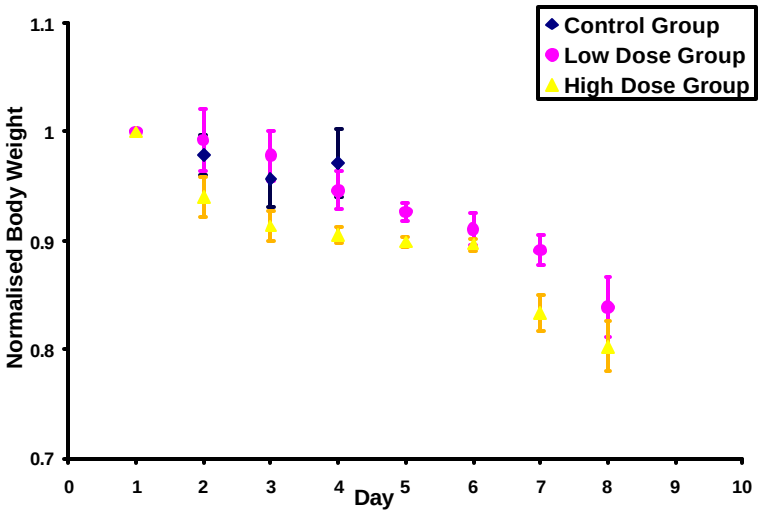

Figure 3.29: Change in rat body weight with time

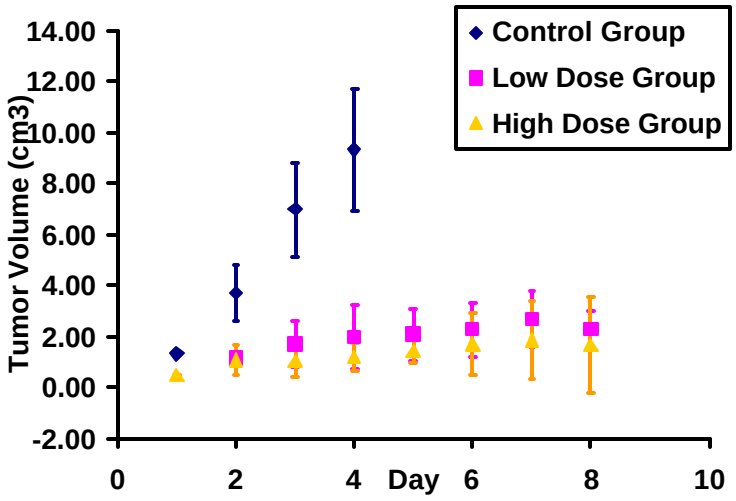

Figure 3.30: Change in rat tumor volume with time

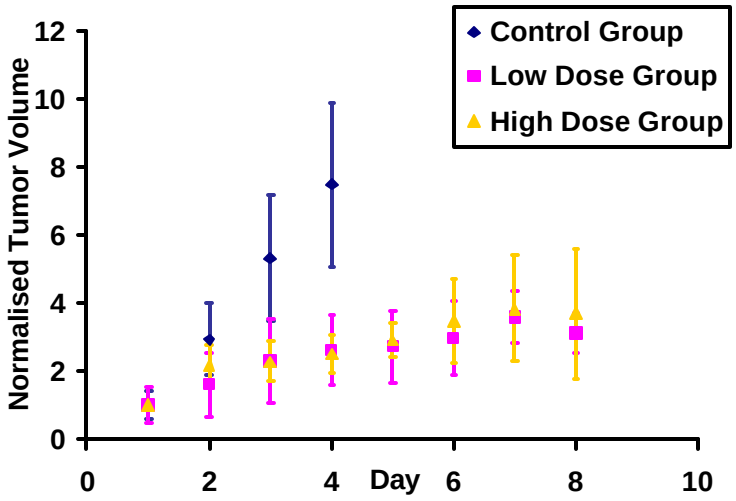

Figure 3.31: Change in normalized tumor volume with time

3.7 Tumor Histology

On day 4, an animal from each of the untreated control group and treated low dose group was sacrificed for the purpose of histology. The animals were sacrificed, and the skin was cut to expose the tumor vasculature such that the vasculature remained intact. Fig 3.32(a) shows the tumor from the untreated group. It can be seen that the size of untreated tumor is relatively large as compared to the low dose treated tumor shown in Fig. 3.32(b). The untreated tumor appeared to be highly vascularized as compared to the treated tumor. Histology was performed on the cross section of the untreated and treated tumors, and the results are as shown in Figs 3.32(c) and 3.32(d).

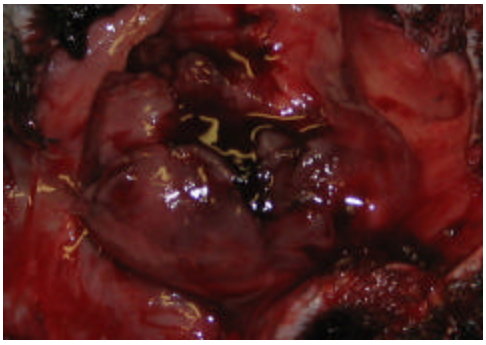

(a)

(b)

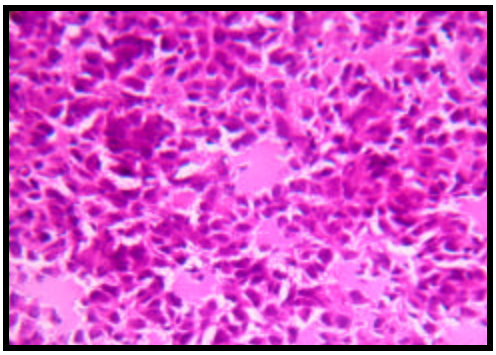

(c)

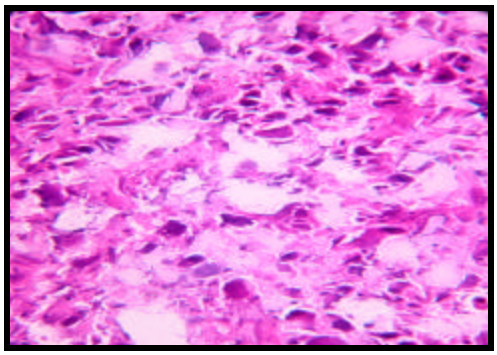

(d)

Figure 3.32: a) untreated rat prostate tumor after day 4 (b) tumor treated with low dose after day 4 (c) histology from the untreated tumor (d) histology from the treated tumor

Both of Figs. 3.32(c) and 3.32(d) were taken at 400X magnification. It can be seen that the cell density is high in the untreated tumor in comparison to that in the low dose treated tumor in Fig. 3.32(d). As shown in Fig. 3.32(c), the relative size of nuclei in the untreated case is relatively small, and the cells can be seen growing in clusters. Figure 3.32(d) shows that the size of nuclei is large with an abnormal shape, an indication of dysfunction of tumor nuclei. A large number of voids (white empty spaces) can be seen in the image suggesting a less dense cell density as compared to the

untreated group. Some ruptured cell membrane can also be seen in the image. Thus, histology provides clear evidence of the effectiveness of cyclophosphamide in controlling the growth of the tumor.

3.8 Results Obtained from the NIR CCD Imager

The NIR CCD imager was used to monitor the hemodynamic changes in the rat prostate tumors during gas intervention. The images were acquired at 720 nm and 820 nm. Using equations (1.5), (1.6), and (1.7), the relative changes in HbO_2, Hb and Hb Total were determined. The spatial hemodynamic maps of relative hemoglobin concentrations were averaged to obtain the plots showing temporal hemodynamic changes. The hemodynamic changes in rat prostate tumors that were implanted subcutaneously on foreback were monitored during the course of chemotherapy, and the complete sets of results are shown in appendix A. A few representative graphs showing hemodynamic changes during gas intervention obtained from the NIR CCD imager are given in Figs. 3.33, 3.34, and 3.35 below. A downward trend is seen in Fig. 3.34, which could be due to a gradual drop in the body temperature and/or the effect of anesthesia. I will discuss the latter point in Chap. 4.

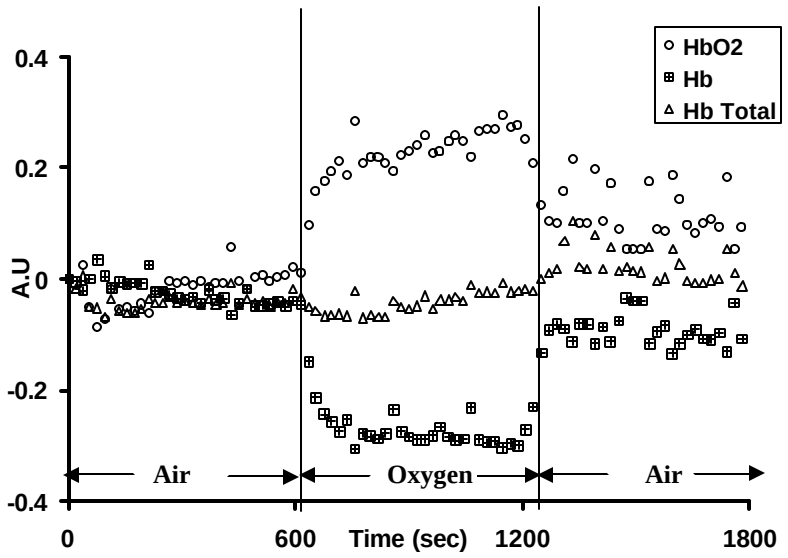

Figure 3.33: Hemodynamic changes in rat 4, day 1, high dose group during gas intervention

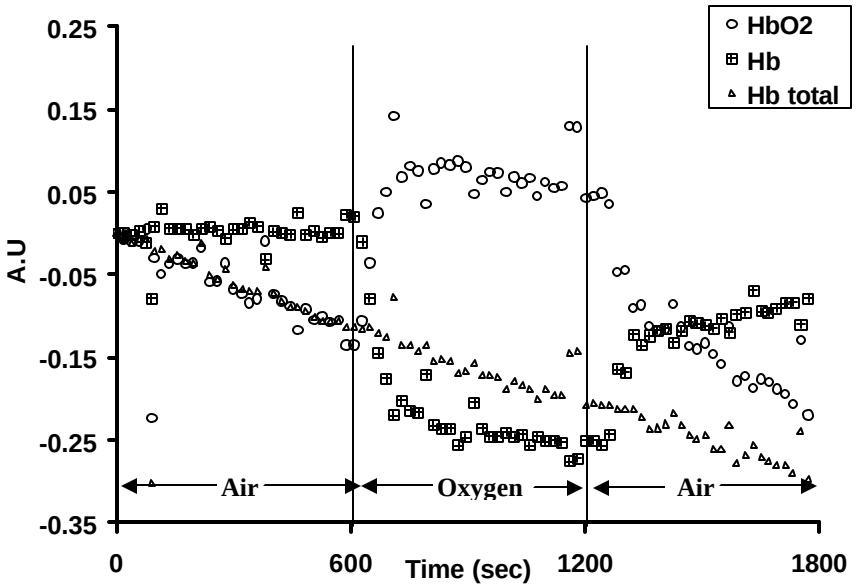

Figure 3.34: Hemodynamic changes in rat 1, day 1, control group during gas intervention

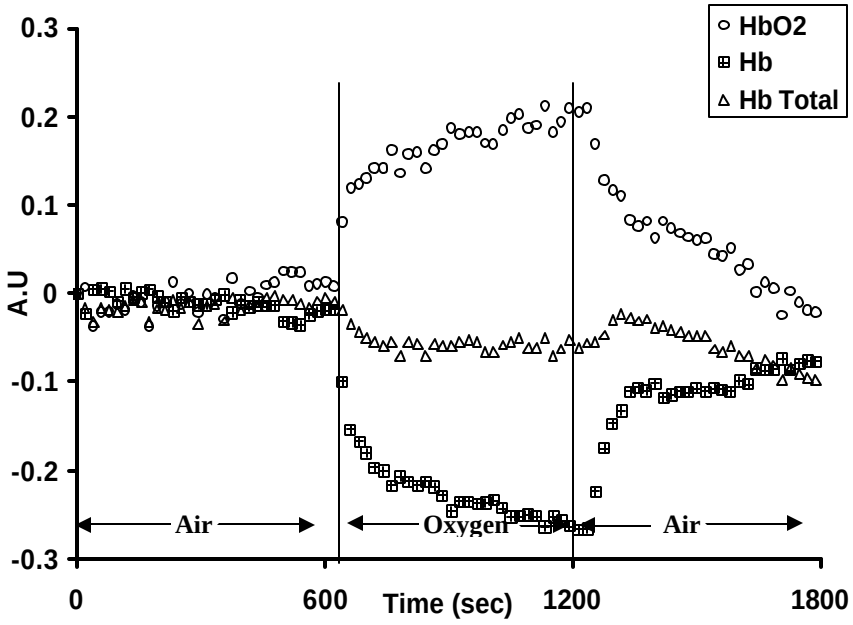

Figure 3.35: Hemodynamic changes in rat 2, day 1, low dose group during gas intervention

3.9 Comparison of CCD Results with Results from Spectrometer

NIR CCD imager data was validated by using a single-channel spectrometer and an optic fiber that simultaneously acquired data along with the CCD imager during gas intervention. The fiber optic probe was placed touching the tumor site. The same single light source was used to illuminate the tumor for both the CCD imager and spectrometer. The sampling rate of spectrometer was set to 1 scan per spectrum. The rat breathed air for the first 10 minutes as baseline, oxygen for next 10 minutes, and air again for 10 minutes. The wavelengths at 720 nm and 820 nm were chosen for both the CCD imager and spectrometer to quantify Hb and HbO_2.

Simultaneous data was acquired for a few rats and shown in Figs. 3.36, 3.37, 3.38 and 3.39 below. My observation on the data includes several points: (1) CCD data

in Figs. 3.38 and 3.39 appears to be noisy, (2) the data obtained from the spectrometer is also much noisier than those previously reported [13, 19], and (3) both CCD and spectrometer data in Fig. 3.36 show the downward drift. Points (1) and (2) will be further discussed in Chap. 4, and point (3) reveals that the downward drift is not instrument-dependent, rather caused by tumor physiology.

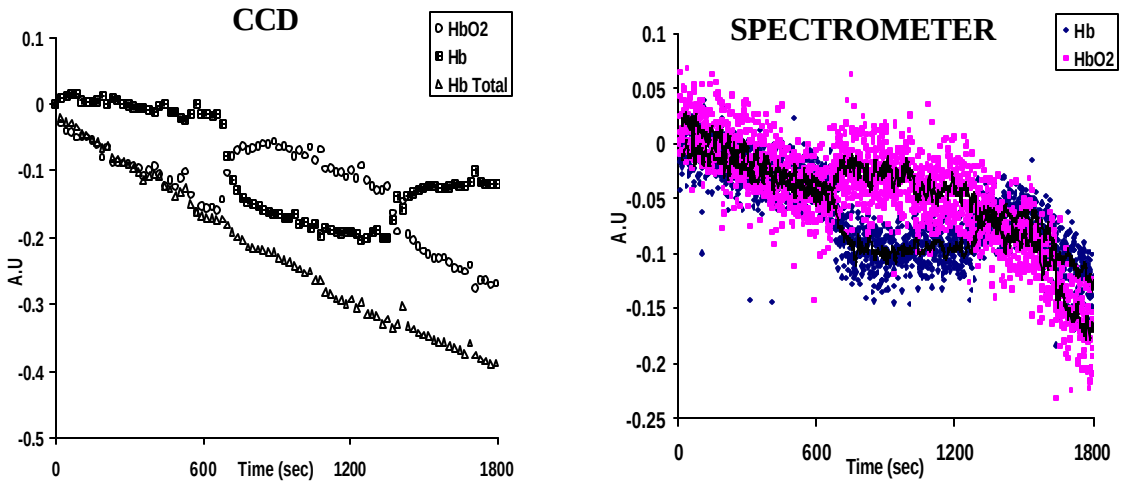

Figure 3.36: Data acquired simultaneously using CCD and spectrometer on Control group, Day 3, Rat 2.

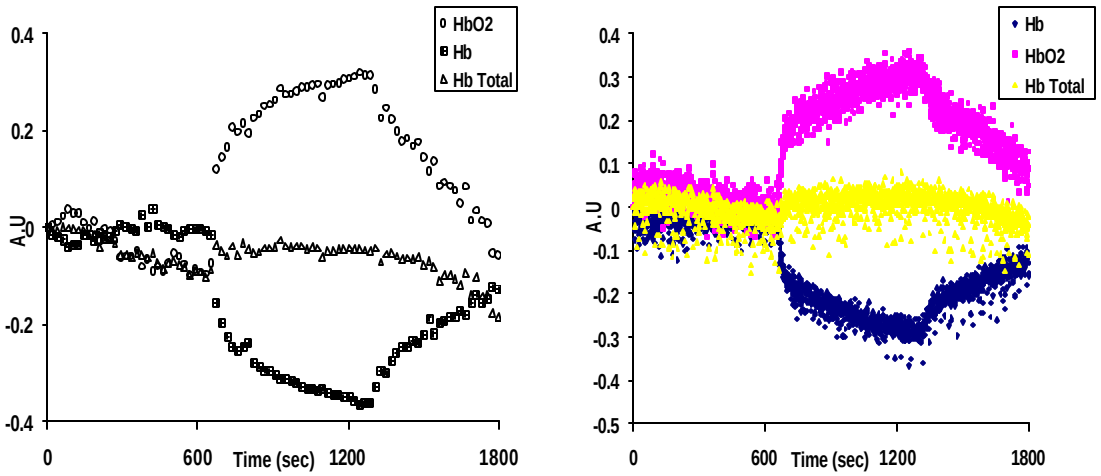

Figure 3.37: Data acquired simultaneously using CCD and spectrometer on Control group, Day 3, Rat 6.

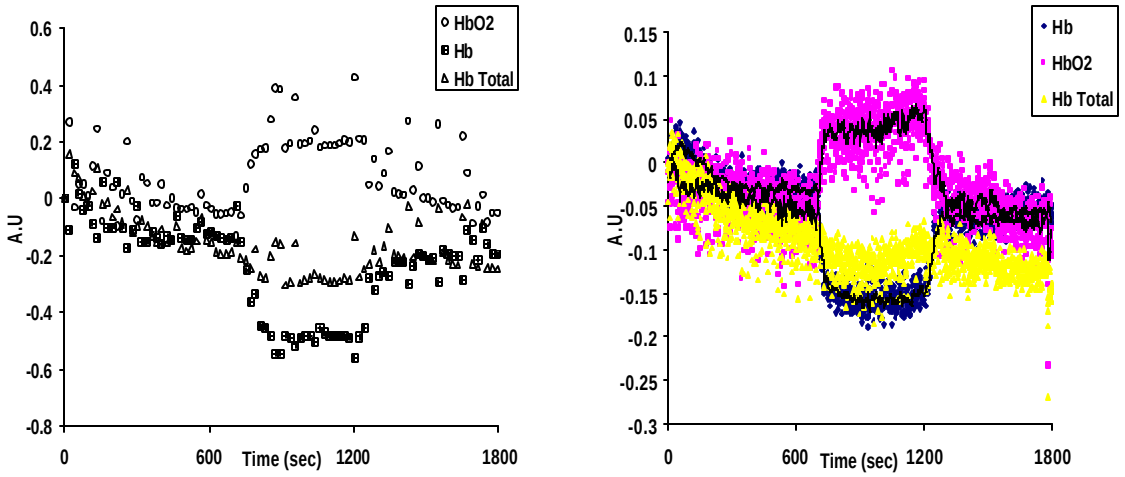

Figure 3.38: Data acquired simultaneously using CCD and spectrometer on high dose group, Day 1, Rat 2.

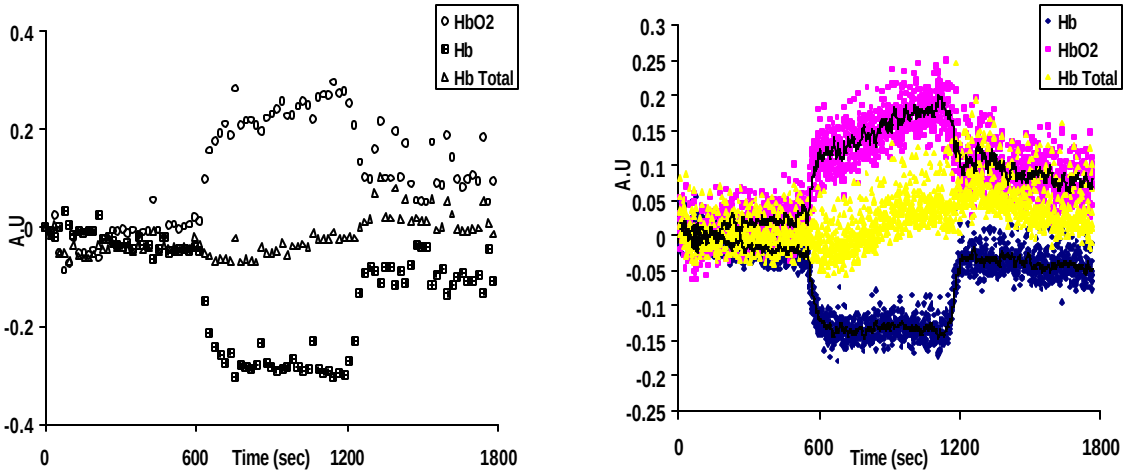

Figure 3.39: Data acquired simultaneously using CCD and spectrometer on high dose group, Day 1, Rat 5.

From Figs. 3.36 to 3.39, it is quite clear that the hemodynamic trends obtained from the NIR CCD imager and the single-channel spectrometer are quite similar. This

part of study proves that, like the spectrometer, the NIR CCD imager can also monitor hemodynamics in rat prostate tumors with the advantage of providing spatial images for tumor hemo-static and hemodynamic heterogeneities.

3.10 CCD and Oximetry Data during Chemotherapy

Hemodynamic changes were monitored on a daily basis for all the groups when the animals were under chemotherapy. Simultaneously, oximetry data from MouseOx was also recorded. Representative CCD and oximetry data are shown below in Figs. 3.40 to 3.44. The animal inhaled air for the first 10 minutes, oxygen for the next 10 minutes, and air for the last 10 minutes, and the data was recorded. It can be seen from these graphs that the rats show normal oximetry during anesthesia. The global arterial oxygen saturation (S_pO_2) increases to its maximum (i.e., from ~97% to 100%) during 100% oxygen intervention, and the oximetry shows normal trend. Also, it can be seen that during gas intervention, there is a corresponding hemodynamic change (i.e., HbO_2 change) in the tumor detected by the CCD imager.

In Figs. 3.40 and 3.43, a downward drift in tumor hemodynamics can be seen. This drift may result from the current anesthesia method used as it might induce a decrease in body temperature and change in the heart rate. The oximetry data shows that isoflurane, as an anesthetic, does not cause any large variations in the animal oximetry readings. In our earlier studies [13, 19], there was a significant reduction in arterial oxygen saturation which is not seen in this study.

The oximetry data obtained from most of the animals during the course of this study appears to be normal (>95%). The arterial oxygen saturation increases when the

animal breathes pure oxygen. The corresponding hemodynamic increases during gas intervention are also evident from the figures shown below. Notice that Fig. 3.41 shows a gradual increase in arterial oxygen saturation, whereas all other figures exhibit an immediate prompt in S_pO_2 when the breathing gas was switched to pure oxygen. Accordingly, the increase in HbO_2 seen in Fig. 3.41 is not as fast as those in other figures. This reveals that a slower change in S_pO_2 will result in a slow increase in HbO_2, as we would expect.

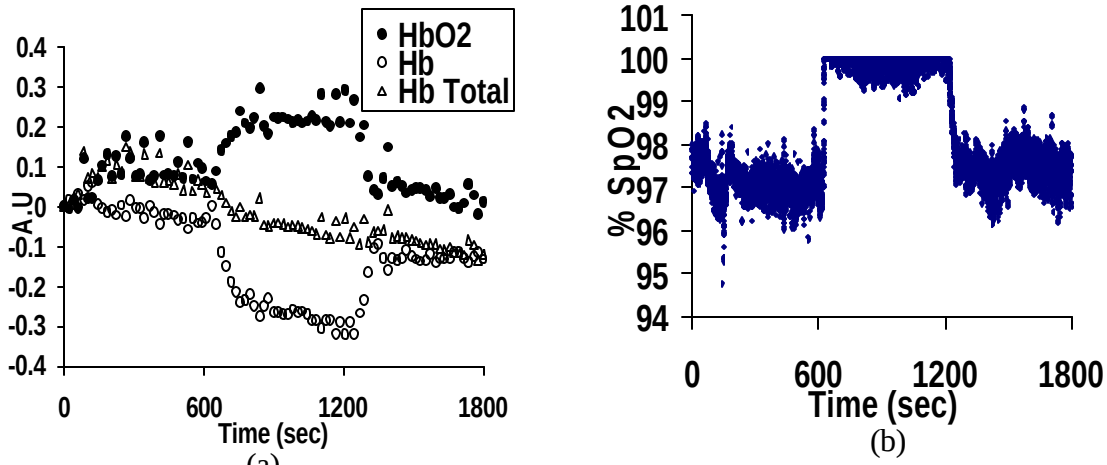

(a) (b)

Figure 3.40: Results of control group, rat 3, day 1 (a) CCD (b) MouseOx

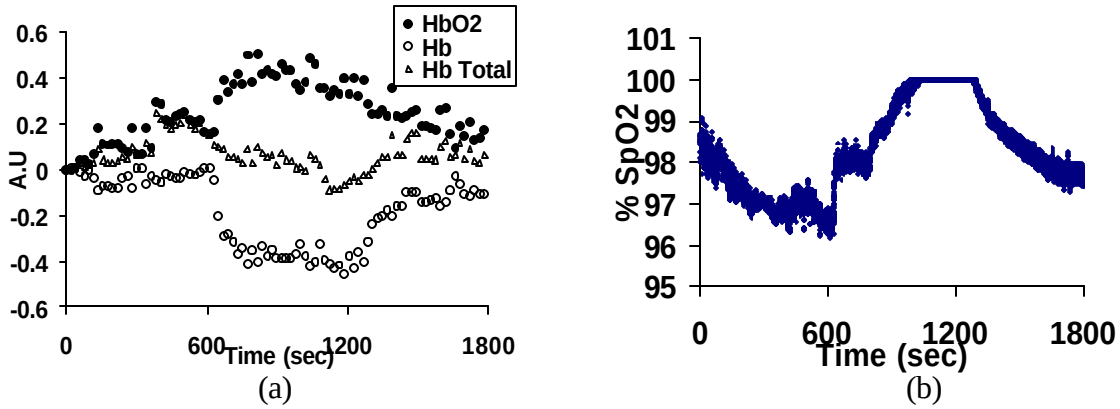

(a) (b)

Figure 3.41: Results of control group, rat 3, day 2 (a) CCD (b) MouseOx

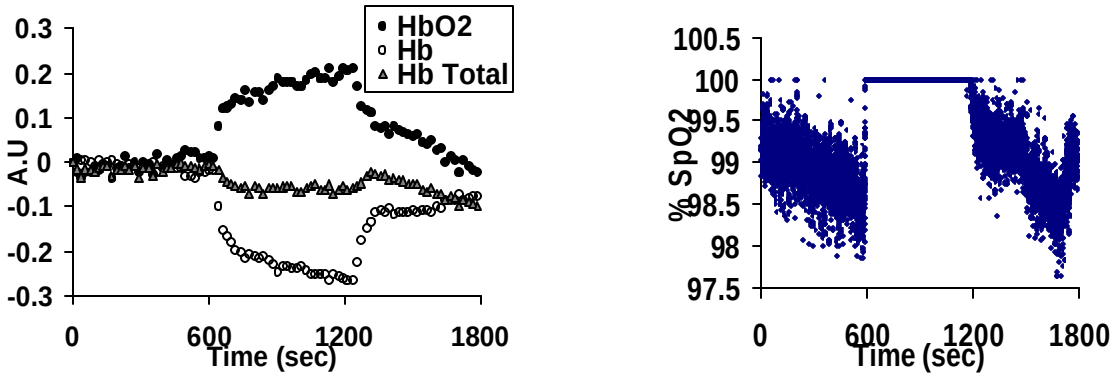

(a) (b)

Figure 3.42: Results of low dose group, rat 2, day 1 (a) CCD (b) MouseOx

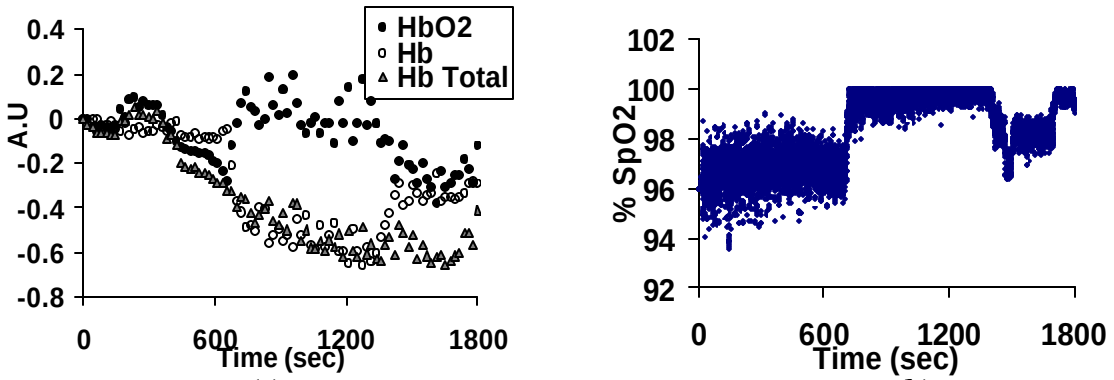

(a) (b)

Figure 3.43: Results of low dose group, rat 2, day 2 (a) CCD (b) MouseOx

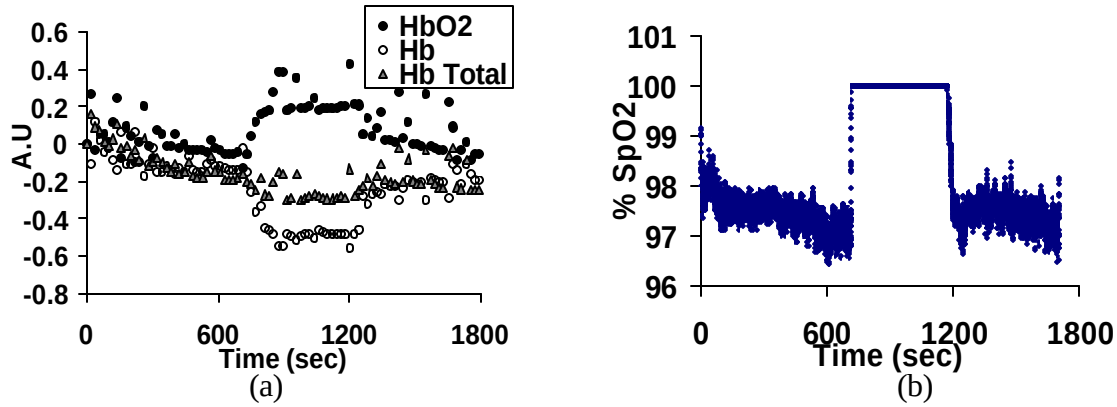

(a) (b)

Figure 3.44: Results of high dose group, rat 2, day 1 (a) CCD (b) MouseOx

3.11 Hemodynamic Maps Showing Relative Changes during Intervention

Topographic maps of tumor hemodynamics showing relative changes in oxygenated hemoglobin, deoxygenated hemoglobin and total hemoglobin concentrations during gas intervention are shown in Figs. 3.45, 3.46 and 3.47 below. These maps were constructed using the images obtained from the NIR CCD imager at wavelengths of 720 nm and 820 nm and using equations (1.5), (1.6) and (1.7). Fig. 3.45 gives a set of photos, showing the experimental setup, and the calculated hemodynamic maps obtained during the course of measurements. The images were obtained from the tumor region by focusing the camera on the tumor surface. The first row of the colored images shows the baseline readings of [Hb], [HbO_2], and [Hb total] when the rat inhaled air. The baseline was taken in a duration of 10 minutes and has 30 acquired images (about 20 sec per image through all 6 filters). The 3rd image (~ 1 minute after the starting point) was selected as a representative map for baseline. The oxygen gas intervention also lasted 10 minutes. The hemodynamic images taken at the peak of [HbO_2] during oxygen intervention were selected as representative maps for hemodynamic changes (see the second row of the colored images). It can be seen that during oxygen intervention, some areas in the tumor region show an increase in [HbO_2] and a simultaneous decrease in [Hb]. Figures 3.46 and 3.47 show two other examples from different rats at different times, and the maps were constructed using the same procedures as described above.

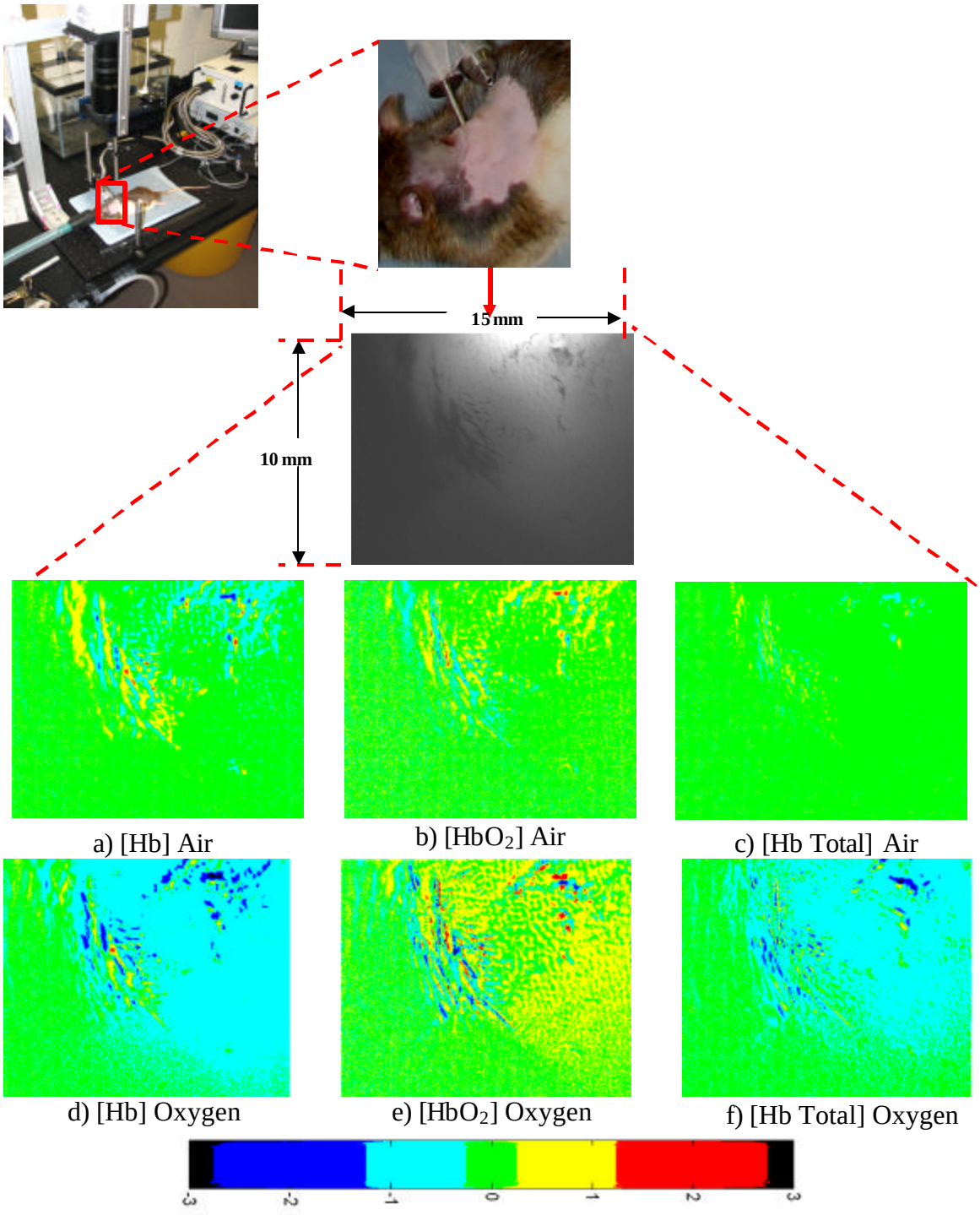

Figure 3.45: Tumor hemodynamic maps taken from rat 3, control group, day 1: showing changes of [Hb], [HbO_2], and [Hb Total] maps during baseline when the rat breathes air (top row) and during intervention when the rat breaths 100% pure oxygen (bottom row).

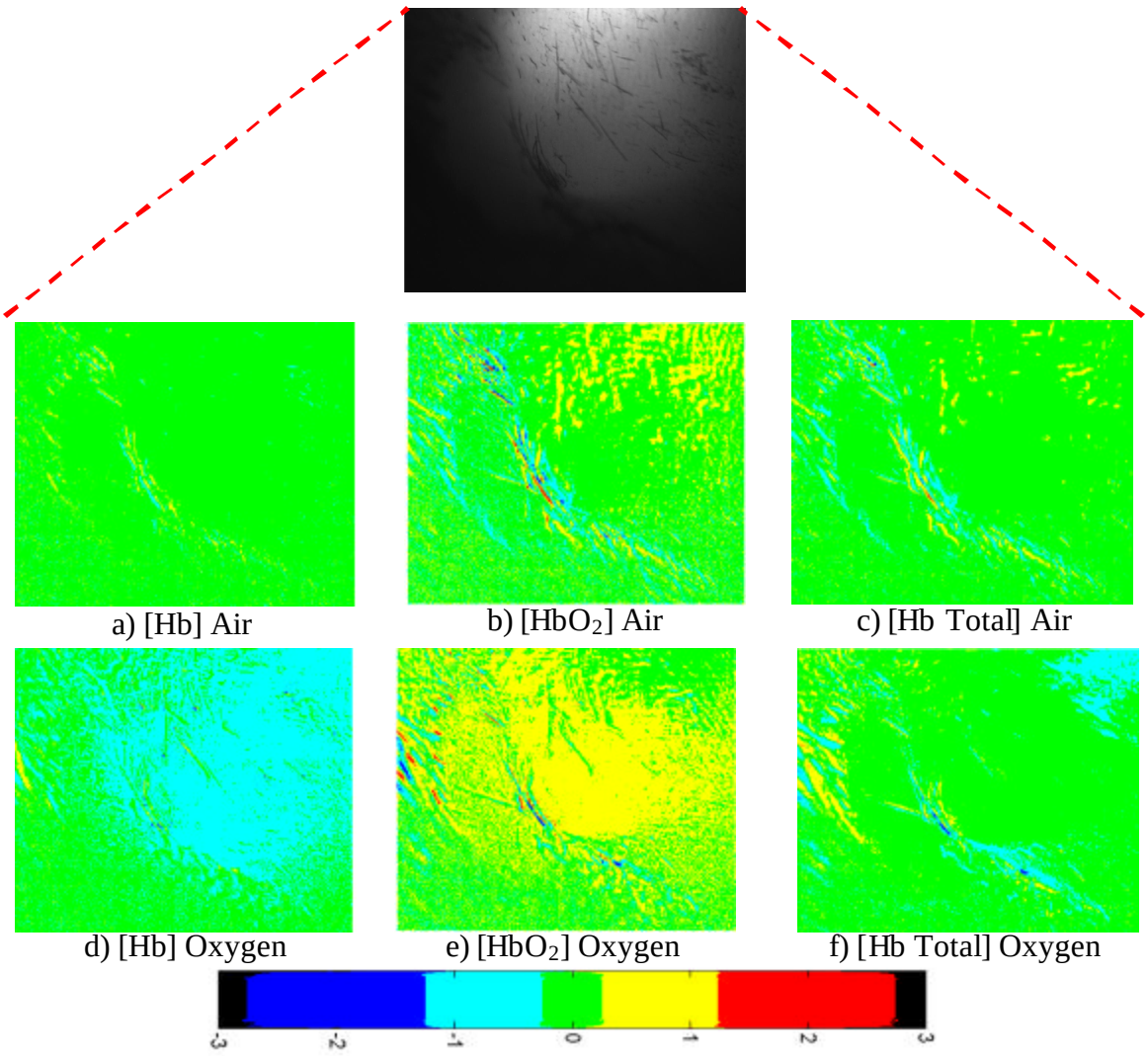

Figure 3.46: Tumor hemodynamic maps from rat 4, control group, day 1: showing changes of [Hb], [HbO_2], and [Hb Total] maps during baseline (top row) and during oxygen intervention (bottom row).

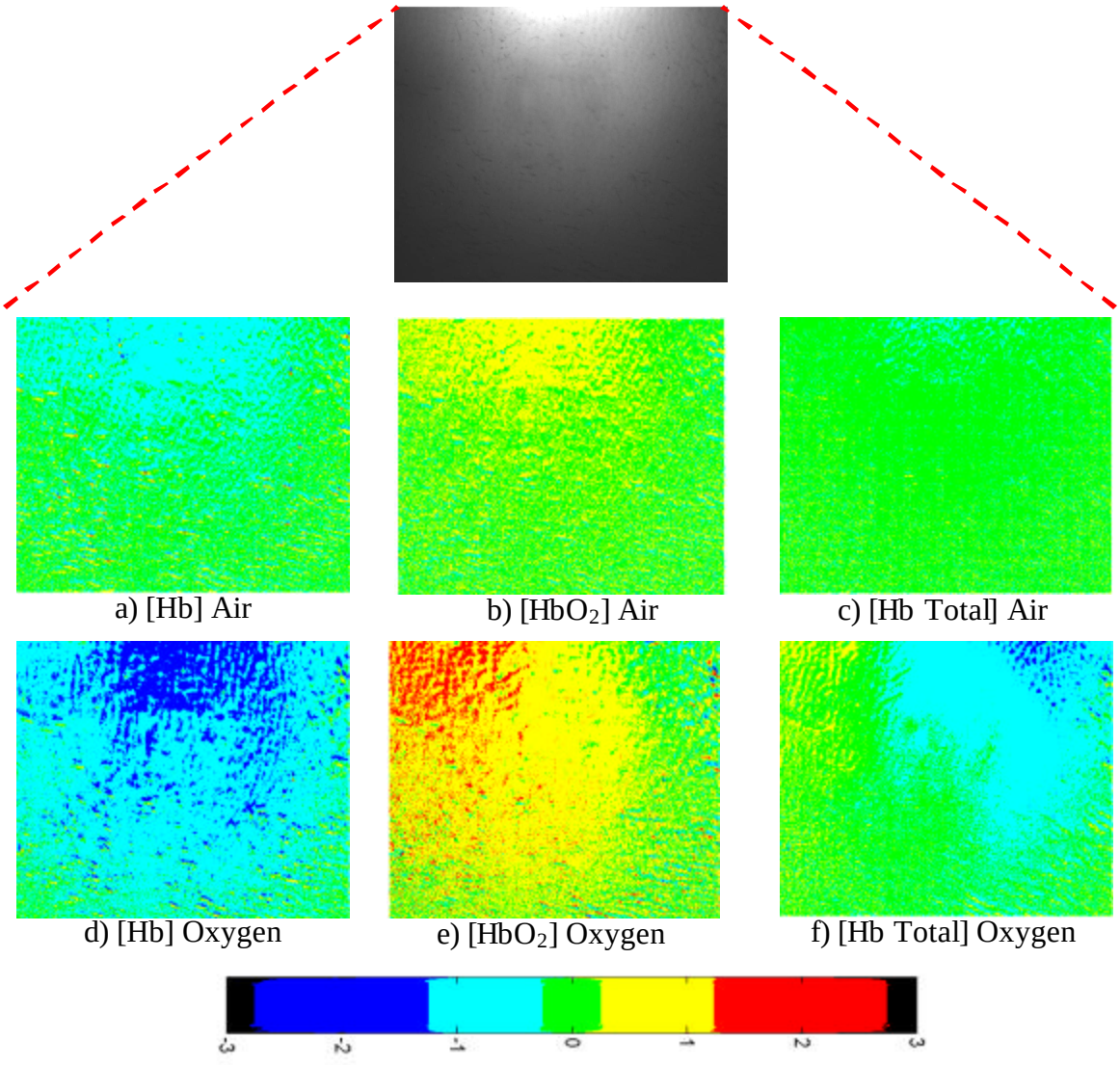

Figure 3.47: Tumor hemodynamic maps for rat 5, control group, day 2: showing changes of [Hb], [HbO_2], and [Hb Total] maps during baseline (top row) and during intervention (bottom row).

CHAPTER 4

DISCUSSION

4.1 Phantom Studies Using NIR CCD Imager

4.1.1 Light Propagation and Photon Migration through the Intralipid

Photons propagate through the tissue or a uniform medium in a banana shape pattern. Using the diffusion approximation in a uniform medium, scientists have classified the optical properties of various tissues [22, 23]. The photon path density distribution function is based on semi-infinite space geometry and depends on the source-detector separation. Since the phantom consists of an Intralipid solution without ink, the absorption factor is very weak. As described in section 3.1.1, the brightest spot in the images of the Intralipid at varying source depths corresponds to the peak position of photon path distribution function. According to the photon path density function equation for semi-infinite geometry, with weak absorption, the distance of the peak position (brightest spot) is given by [22]

$$z_0^{\max} \approx \frac{\sqrt{2}d}{4}, \tag{4.1}$$

$$z_0^{\max} = 0.707\left(\frac{d}{2}\right), \tag{4.2}$$

where d is the source detector separation, and $z_0^{\max}$ represents the location for maximal photon density in z direction, or in the direction perpendicular to the banana pattern and the line connecting the source and detector. It can be seen from equation (4.2) that the

location of the brightest spot or the region with highest photon density does not directly depend on light scattering, i.e., the concentration of the Intralipid. Fig. 4.1 below shows the schematic representation of photon propagation through the Intralipid phantom and detection by the CCD imager.

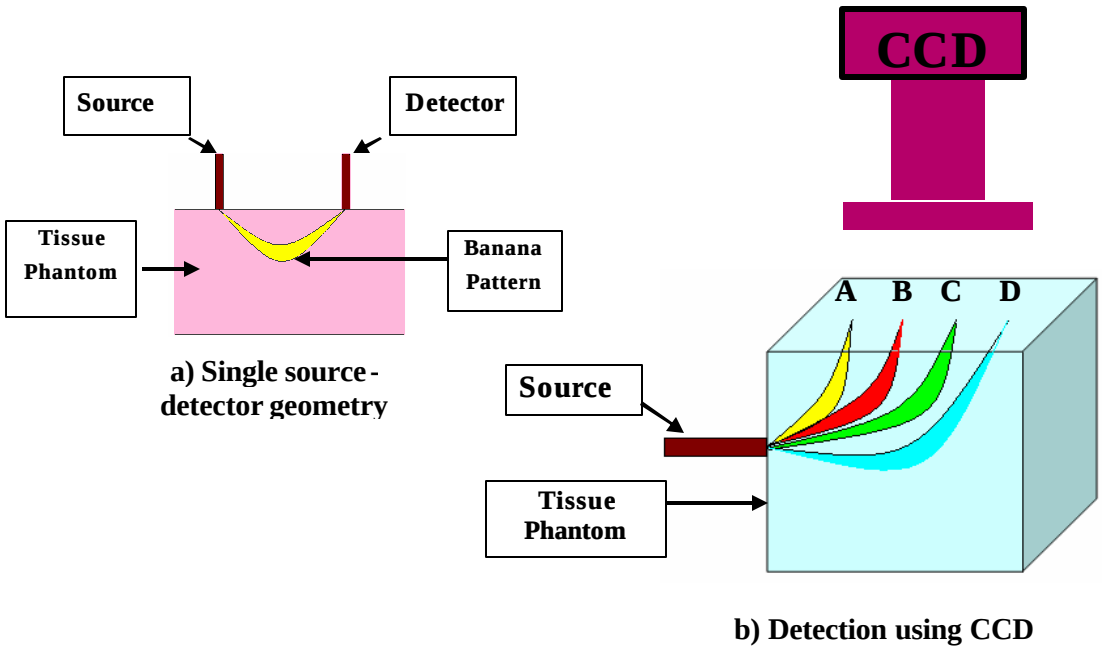

Figure 4.1: Schematic showing the banana shaped pattern of photon propagation through the Intralipid and detection by the CCD

In theory, the ideal slope obtained from equation (4.2) has a value of 0.707. It can be seen from Figs. 3.4, 3.5 and 3.6 that distance of the bright spot varies linearly with the location of light source. The slopes obtained for different Intralipid concentrations also remain fairly constant and do not show much variance on Intralipid concentrations. The values of slope obtained for 0.5%, 1% and 1.5% concentrations are nearly 0.5, a little smaller than the theoretical value. Notice that equation (4.2) was

derived from a semi-infinite geometry, while the phantom used for our studies was much smaller than a semi-infinite medium. The deviation in slope between the experimental and theoretical values could be attributed to the lack of sufficient volume of Intralipid for semi infinite conditions. The fact that the slopes do not vary directly with the change in Intralipid concentration is expected, as predicted by equation (4.2). This experiment proves to be useful in understanding photon propagation through a highly scattering medium (the Intralipid solution). This preliminary data provides valuable visual and statistical information about photon diffusion and propagation through a homogenous and uniform medium and could be useful for further characterization of the CCD imager.

4.1.2 Path Length Mask

In our previous studies, we used the single source-detector geometry for measuring hemodynamics in rat tumors [1]. The source-detector separation was kept the same and thus '*d*' remained constant, and DPF of the tumor tissue was assumed to be a constant. In case of CCD images, since every pixel acts as a detector, the distance '*d*' for each pixel would be slightly different and is a function of the location of the pixel in the image coordinate system and depth of light source. Figure 3.8 shows an example of an Intralipid surface with and without path length mask. It can be seen from the graphs that there is a decrease in magnitude of change in optical density of the images when mask is used. The corrected image is a better representation of the actual photon diffusion pattern compared to the uncorrected image. The location of light source from the surface of the object (Intralipid solution) and the exact physical

dimensions of object in the image should be known to compute the path length mask. Inclusion of path length mask is imperative in computation of hemodynamic changes and should not be assumed to be constant for the CCD images.

4.1.3 Effect of Variation in Intralipid Concentration on OD Images

Figures 3.9- 3.20 show a variety of CCD images of light intensities and the corresponding profiles taken with the light source at different depths (10-30 mm) and with varying Intralipid concentrations (0.5%-1.5%). The pathlength correction mask has been used in the calculation of optical density plots. It is seen that the magnitude of the optical density profiles depends on light intensities of Io and I_T. The spatial distributions of all these images have shown non-uniformity, which may result from the CCD imaging system due to its optics. For optical density plots with pathlength corrections, it is expected that the relative changes in light intensity will be uniform across the image. However, the theoretical expectation is not met, as seen in those figures. These results are suggestive of non-uniformity in the CCD imager and also indicate the presence of source bias to a certain extent. Further study is definitely needed to investigate and correct such non-uniformity for the NIR CCD imager.

Figs. 3.21, 3.22, 3.23 and 3.24 show the effects of variation of concentration of Intralipid at the light source depth of 10 mm, 15 mm, 20 mm and 30 mm, respectively. At a fixed depth, it can be seen from Figs. 3.21 and 3.22 that photon migration path, or the penetration depth of the largest photon density, is longer when the concentration of Intralipid is less. As the concentration of the Intralipid increases, the photon pattern bends shallower before emerging on the surface, thus covering a shorter distance during

propagation. When the source depth moved deeper at 20 and 30 mm (Figs. 3.23 and 3.24), the signals became weaker with a larger measurement noise, and the profile peaks do not depend on the Intralipid concentration much. Figs. 3.25 to 3.27 basically demonstrate a similar conclusion to that shown in Figs. 3.4 to 3.6. Notice that 1.5% Intralipid concentration induced larger measurement noise due to an increase in scattering property. Overall, from this experiment, it is evident that as density of Intralipid increases, scattering also increases resulting in shallower photon patterns, provided that the light source depth is fixed.

4.1.4 Effect of Variation in Depth of the Light Source

For each concentration of Intralipid, the depth of the light source was varied. It is seen that as the depth of the light source increases, the diffusion of photons is relatively more homogeneous because more events of light scattering take place. This is supported by Figs. 3.21 to 3.24 that the effect of concentration becomes less evident with an increase in depth of the light source. These results provide valuable information about diffusion of photons in a uniform and homogeneous medium. The information obtained from these experiments is valuable in visually understanding the diffusion of photons through a medium and characterizing the NIR CCD imager.

4.1.5 Effect of Optics on the CCD in Reflectance Mode

Results obtained by taking a reflectance image on a calibration sample, as described in section 3.5, show the effect of the CCD imager's optics on the image. The ring structures which are seen in the image are a result of the effects of optics in reflectance geometry. A profile across the image shows a Gaussian-like distribution

with the highest detected intensity at the center. To correct this effect, 'auto-leveling' is required so that intensity distribution across the image is homogenous and is not affected due to the optics. By applying a pixel wise correction, useful signal image can be obtained as [8]

$$u = \frac{r - o - t}{f - o - t} * k \,, \tag{4.3}$$

where, '*r*' is the raw image, '*o*' is the offset image, 't' is the thermal image, '*f*' is the flat field image, and '*k*' is the mean intensity of the flat field image. In this way, CCD can be calibrated and used in reflectance mode.

These phantom studies have proven to be very useful in understanding the behavior and characterization of the NIR CCD imager system in transmittance mode as well as understanding the photon diffusion through a homogeneous medium. Since we calculate the change in optical density, most of the inhomogeneity should be removed by the equation in principle. However, spatial inhomogeneity still exists because of the camera's optics in the imager and inhomogeneous distribution of photons across the CCD imager. To correct for these inhomogeneities, a calibration using an Intralipid phantom can be performed. The experimental setup will have to be kept fixed after calibration including the position of light source and the optical settings of lenses on CCD. The surface of Intralipid solution is a homogeneous and uniform surface. Using the image obtained from the surface of Intralipid, a correction map can be generated to account for the inhomogeneities in the imager. This correction map can be used on the acquired images and incorporated as a part of the algorithm. The information obtained

from these phantom studies would be helpful in better understanding and analyzing the preliminary animal data.

4.2 Animal Studies, Chemotherapy and Monitoring of Hemodynamic Changes in Rat Prostate Tumor

Animal experiments were performed to study the feasibility of NIR CCD imager in monitoring hemodynamic changes in rat prostate tumors during gas intervention. Cyclophosphamide, a chemotherapeutic agent, was administered to study its outcome for the rat prostate tumors and to examine if it is possible to monitor its effect on the tumor vasculature using the NIR imager. The discussion for the animal measurement results can be divided into several sub-sections below.

4.2.1 Chemotherapy

As described previously in section 2.2.4, chemotherapy was administered in the low dose group and high dose group. Tumor volume and body weight were monitored on a daily basis. It can be seen from Figs. 3.30 and 3.31 that the untreated control group shows a higher rate of tumor growth as compared to the high dose and low dose groups. However, there is no significant decrease in body weight of the rats in the control group, indicating the toxicity of chemotherapeutic effects of the drugs on the animals.

The low-dose rat group was injected (i.p.) with a daily dose of cyclophosphamide of 30 mg/kg. It can be seen from Figs. 3.30 and 3.31 that there is inhibition of tumor growth with no drastic fluctuations in the tumor volume, and these figures exhibit a consistent gradual decrease in the body weight of all the animals in the low dose group. Due to the tumor progression and toxicity of the drug, however, most of the animals had lost 20 % of their body weight (Fig. 3.29) and had stopped

grooming by the 8th day after the commencement of chemotherapy, as a result of which, they had to be sacrificed.

The high-dose rat group was injected with a single high dose of 200 mg/kg of cyclophosphamide when the tumor reached an approximate diameter of 1 cm. It is observed that even though the high dose is effective in inhibiting tumor growth as the low dose does (Figs. 3.30 and 3.31), it results in a larger body weight loss (see Fig. 3.29) possibly induced by a higher toxicity in the animals. On days following administration of the drug, bleeding through the urethral opening was observed in all the animals of the high dose group with deterioration in the overall health of the animals. Though not much variation in tumor volume is seen between the high and low dose rat groups, low dose chemotherapy is beneficial and preferred because high dose chemotherapy induces very high toxicity causing animal internal bleeding.

4.2.2 Histology

The tumor of the control group was found to have a very high vascularization, and necrosis was evident in some regions of the tumor, whose color was turning black. Histology was performed on three animals, one from each group, i.e., the untreated control group and treated high-dose and low-dose group, and the results from the control and low-dose group were already shown in Section 3.7. Histological evidence suggests that cancer cells in the control group are regular and denser as compared to those shown in the low dose group. The control group shows a high cell density, and cells can be seen growing in clusters.

A treated tumor from the low dose group is shown in Fig. 3.32 (b). It can be seen that this tumor is smaller and less vascularized as compared to the one in the control group (Fig. 3.32(a)). The histology from the low dose group tumor shows that the nucleus has a large, irregular, and unsymmetrical size and shape with dark staining, an indication of its dysfunction induced by the drug treatment. Many empty voids in the histology suggest the successful annihilation of the tumor cells and deterioration of tumor cell membranes.

4.2.3 Results Obtained from the NIR CCD Imager in Rat Prostate Tumor and Validation Using Single Channel Spectrometer

The NIR CCD imager was used to monitor the hemodynamic changes during chemotherapy. To validate the results obtained from the CCD, a single channel spectrometer was also used for simultaneous data acquisition. It can be seen from the obtained graphs that the CCD imager can be used to monitor tumor hemodynamics and get spatial and temporal topographic maps showing tumor heterogeneity while the detected CCD signals are very noisy and not consistent throughout all the animal measurements. While the graphs obtained from the CCD closely follow those obtained from the spectrometer, they both have noisy signals, much noisier than our previous reported results [13, 19]. Furthermore, although we can monitor hemodynamic changes, many of the graphs obtained from the NIR CCD imager do not show the bi-phasic feature in the tumor [HbO_2] response that have been reported previously [1, 19]. I wish to address several possible reasons for why the NIR signals in this study are noisier and lack of the bi-phasic feature.

The prostate tumor is a slow progressing and less vascularized as compared to other types of tumors. Previous studies of breast tumors using NIR spectroscopy have shown that tumors exhibit a biphasic response during gas intervention [1, 19]. In the CCD imager data, a mean of the image was computed to obtain the data points. Due to tumor heterogeneity, the tumor hemodynamic response varies from region to region. Computation of mean intensity over the entire image could be one of the possibilities for the absence of biphasic response, i.e., the local sharp changes are smoothed out.

The noisy oscillations shown in the data might be attributed to the breathing artifact. The consistent hemodynamic results taken simultaneously from the CCD and spectrometer indicate that the noisy signals are instrument independent and must result from the tumor physiology. In previous studies, Ketamine was used as an anesthetic in conjunction with isoflurane during the course of measurements. In this study, only Isoflurane has been used as an anesthetic agent, and the data obtained from rat pulse oximetry suggests the animals' oxygen saturation to be in the range of 95-97 % during normal air inhalation. Other studies have suggested that anesthetics affect the hemodynamic response to a large extent [24, 25] because anesthetics alter such physiological factors as heart rate, breathing rate and cardiac output. Given the fact that the rats can wake up completely in 2-5 minutes after isoflurane is removed, it is reasonable to suspect that the animals were not under deep anesthesia during the experiment, and that their bodies were not completely relaxed to perform the expected hemodynamic experiments.

The hemodynamic changes in the rat prostate tumors were monitored on a daily basis during chemotherapy regimen. From the current data analysis and processing, also possibly due to the current anesthesia, it is not possible to conclusively reveal the efficacy of chemotherapy based on tumor hemodynamics. Since this study is completely new, during the course of my research, I initiated the animal laboratory setup, animal tumor implantation with the help from Drs. Tang and Shen, animal tumor model development, and the development of the animal experiment protocols. My study described in this thesis provides the future students in the group with the first-handed, valuable, and practical information to better carry on the research development using the NIR CCD imager for animal tumor studies.

In short, the NIR CCD imager can be effectively used in monitoring tumor hemodynamics during gas intervention, and spatial hemodynamic maps can be obtained to show tumor heterogeneity. We believe that the efficacy of chemotherapy could be monitored effectively with the NIR imager after the current sources for noisy signals of the system are clearly understood and removed.

CHAPTER 5

CONCLUSION AND FUTURE WORK

Phantom studies to characterize an NIR CCD imager and data obtained from rat prostate tumors during chemotherapy have been performed in my thesis research, and the study demonstrates the feasibility of using the NIR CCD imager to monitor hemodynamic changes in the tumor and to give spatial maps showing tumor heterogeneity. Though both low dose and high dose chemotherapy prove to be effective in inhibiting tumor growth, the low dose chemotherapy seems to be more beneficially as it does not cause internal bleeding in the animals and has less cytoxic effects, while the high dose chemotherapy induces high toxicity. There are several major issues learned in my study:

(1) Though this study shows the feasibility of using the NIR CCD imager, more rigorous studies towards the characterization and better understanding of the NIR CCD imager needs to be further performed. The major issue is how to correctly calibrate and balance the non-uniformity of the imager across the entire spatial profiles in order to obtain accurate hemodynamic imaging readings. After the relationship between the image uniformity and optical properties of measured tissue is well understood, a calibration and intensity auto leveling module could be added to the imager software module to eliminate inhomogeneities occurring as a result of the imager optics.

(2) As seen through this thesis, the data obtained from the CCD imager is prone to noise. Such noise may be associated with the current anesthesia procedure, i.e., using only isoflurane without other anesthetic agents, which does not provide deep anesthesia to the animals. Further studies are needed to prove the expectation that isoflurane without any other deep anesthetic agent would be a source of signal noises.

(3) The source of noises could be due to motion artifacts arising as a result of breathing. By using filtering techniques and/or correlating the imaging data with the rat breathing rate taken from the pulse oximeter, the imaging noise can possibly be reduced.

(4) For the purpose of this study, only one light source was used to illuminate the tumor. In the future, multiple light sources can be used to illuminate the tumor vasculature for different directions, and these light sources can be alternately switched on using an optical switch. Thus, multiple sets of imaging data can be used to reconstruct the hemodynamic tumor vasculatures under therapeutic intervention or treatment.

(5) There is a need to improve the image processing algorithm and incorporate features which can provide easy accessibility to regional image and statistical analysis. The algorithm developed as a part of this study can be incorporated in the CCD imager software to show real-time hemodynamic changes during the measurement.

(6) The acquisition rate of the CCD also needs to be increased. It is possible to mount the CCD imaging system on a microscope. This setup could greatly enhance the

image resolution and provide a methodology for recording dynamic data at a microscopic level.

In summary, this thesis serves as a preliminary and ground-breaking step for future applications of the NIR, CCD imager for characterization of tissues in vivo, quantification of hemodynamic parameters of tissue/tumor vasculatures, and real-time monitoring of therapeutic efficacy for cancer treatments.

APPENDIX A

DATA OBTAINED FROM CCD IMAGER DURING CHEMOTHERAPY

A1.1 Control Group

Rat 1

Day 1

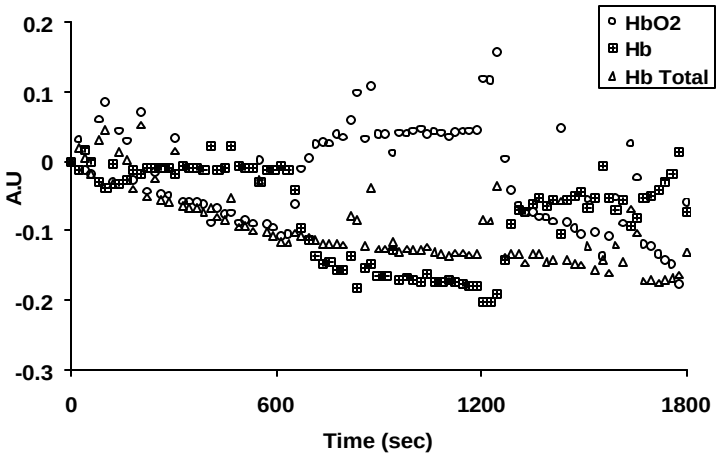

Day 2

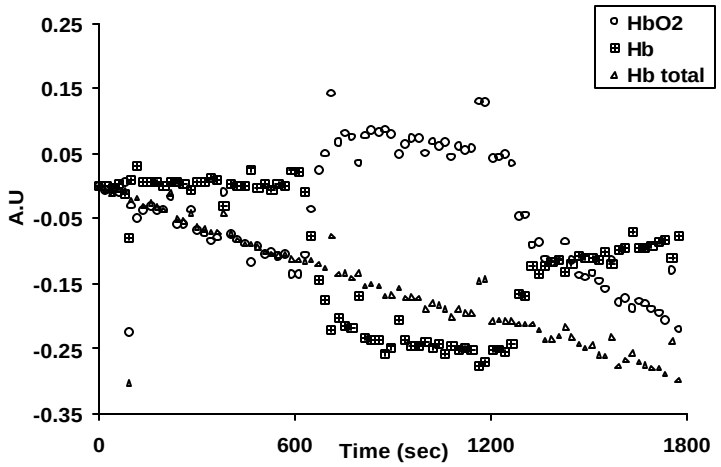

Day 3

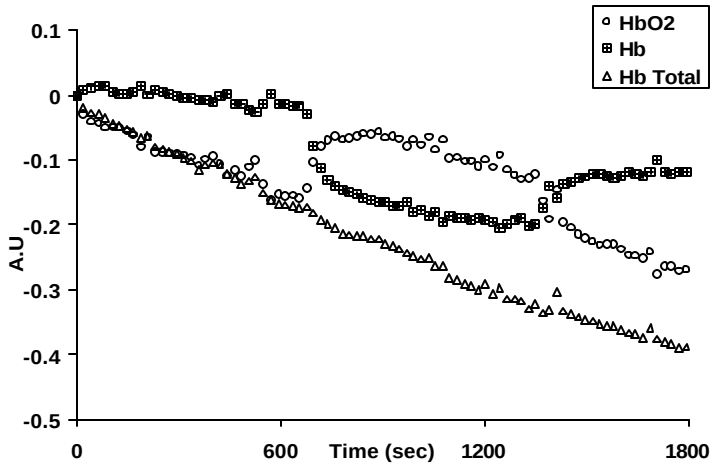

Day 4

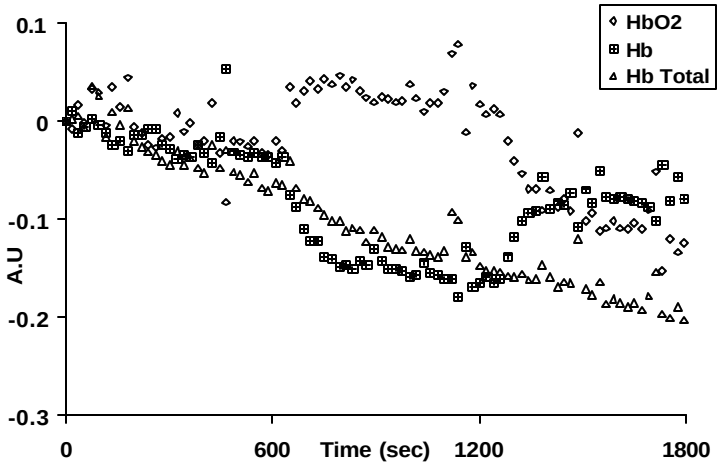

Rat 2

Day 1

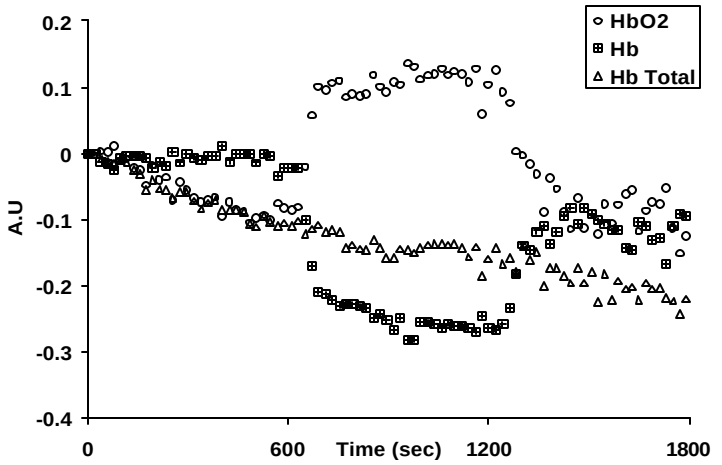

Day 2

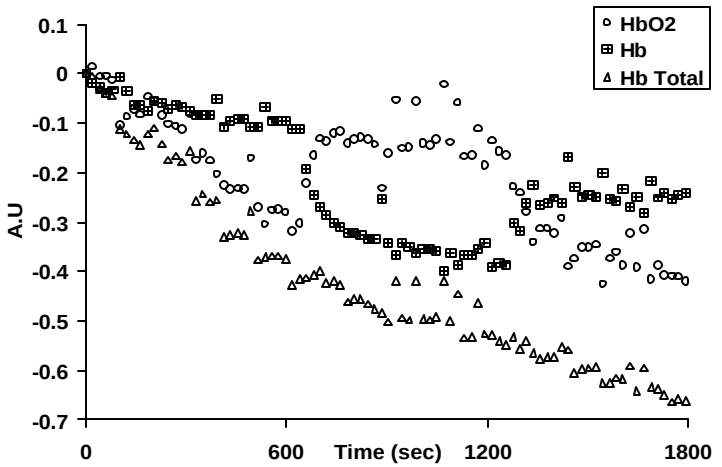

Day 3

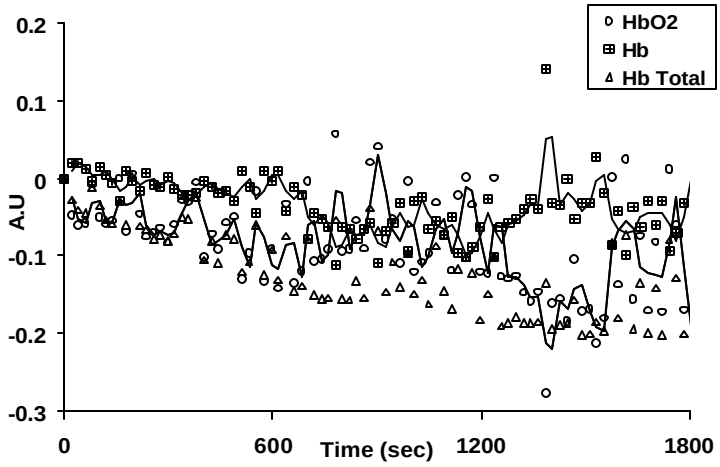

Day 4

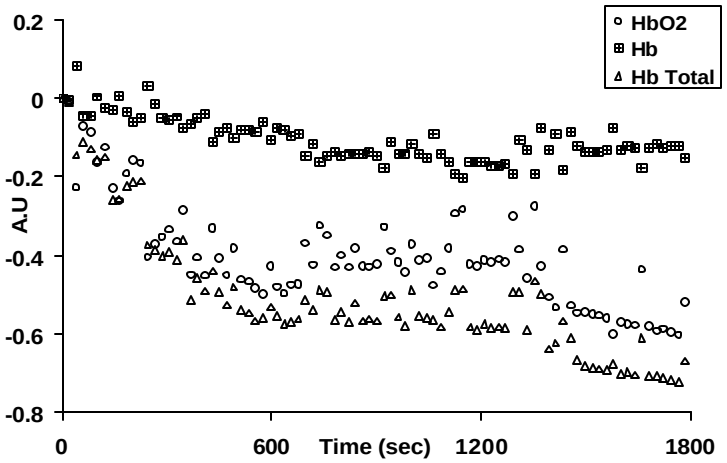

Rat 3

Day 1

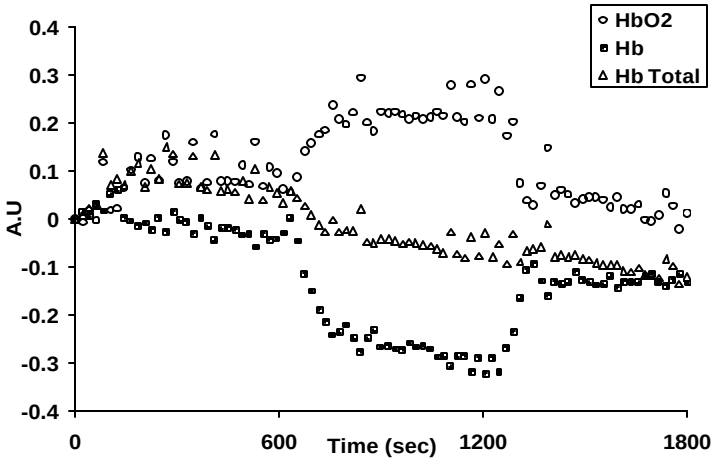

Day 2

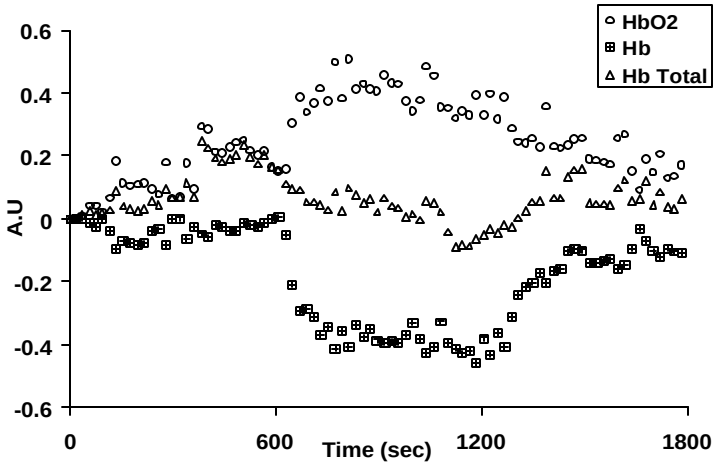

Day 3

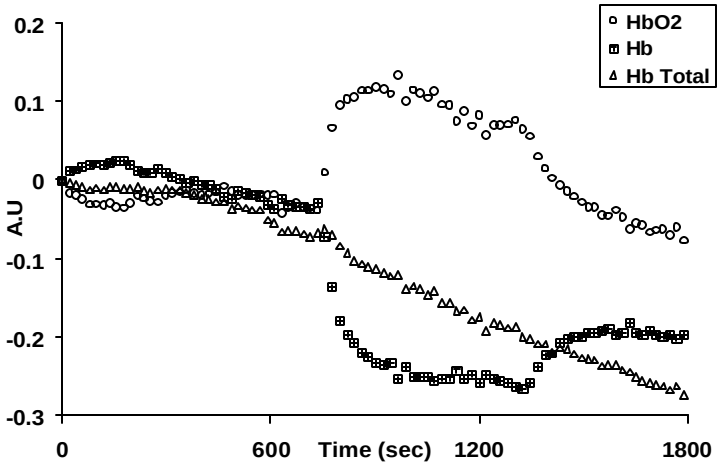

Day 4

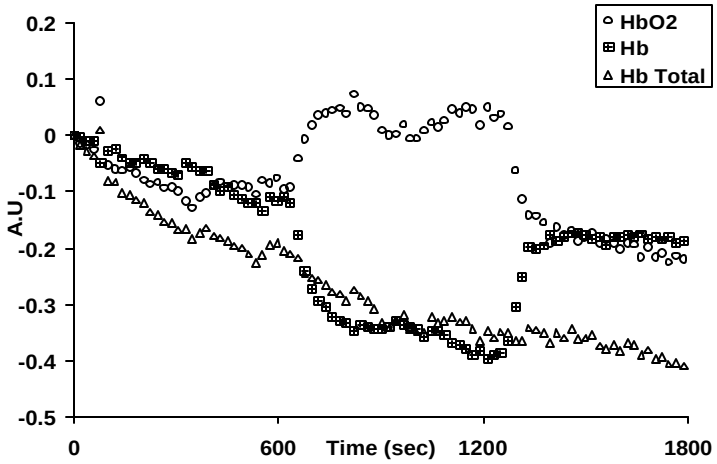

Rat 4

Day 1

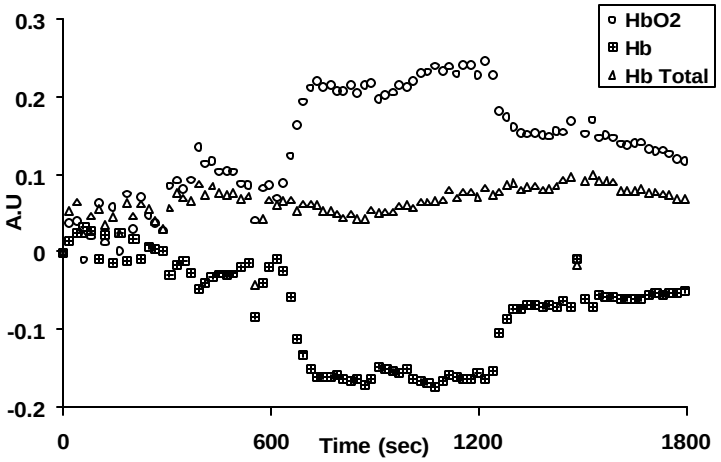

Day 2

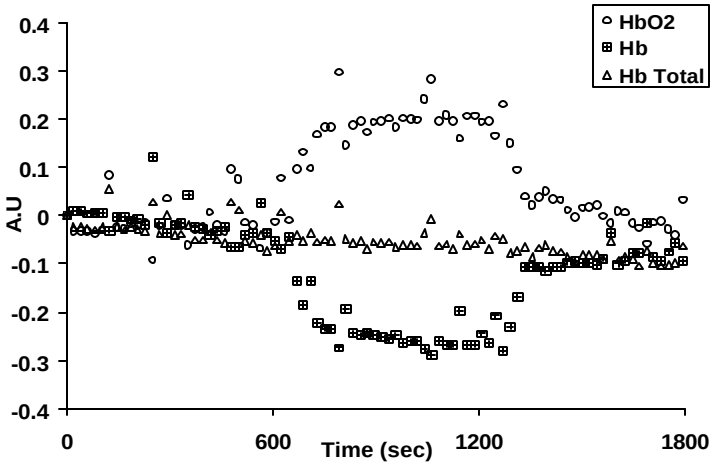

Day 3

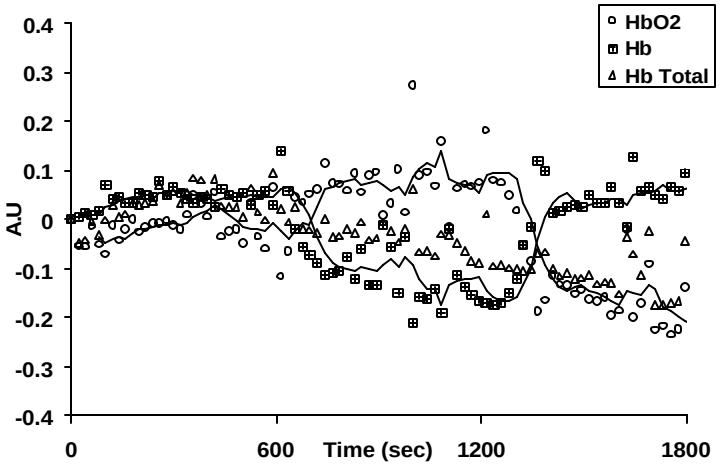

Day 4

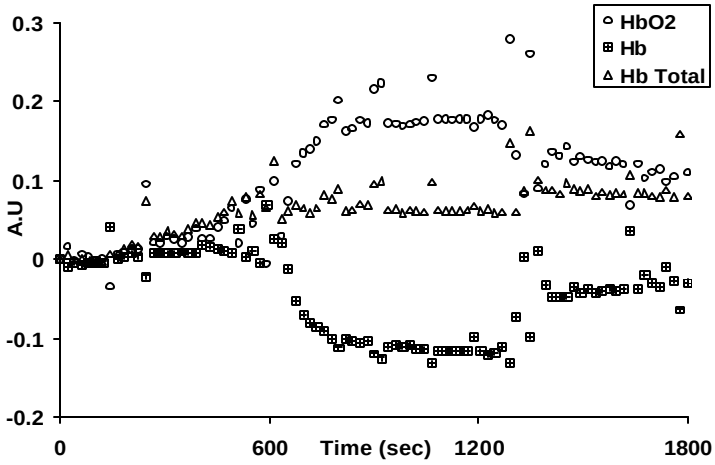

Rat 5

Day 2

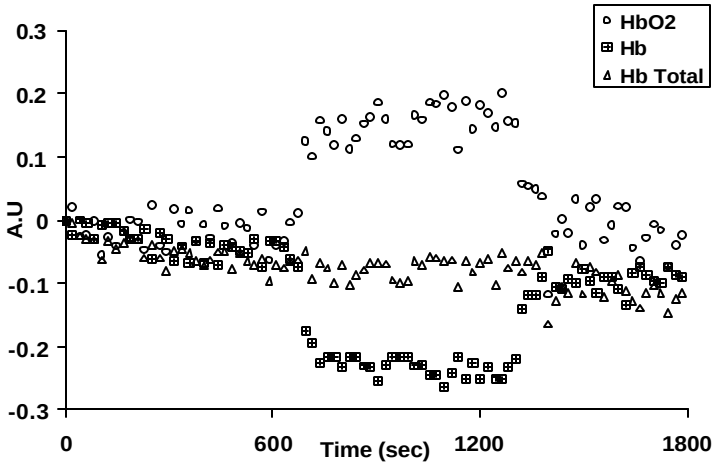

Day 3

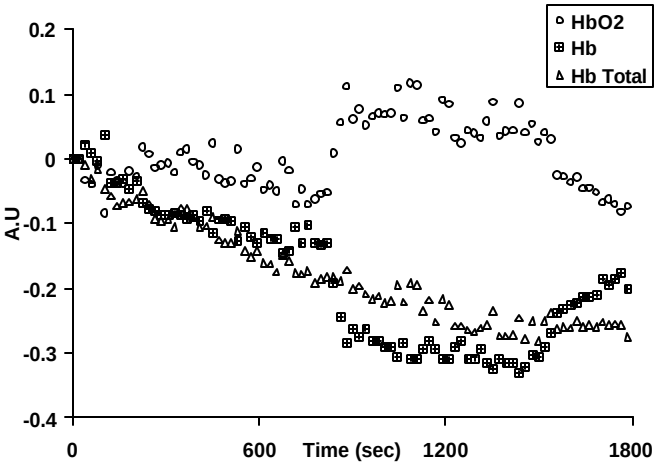

Day 4

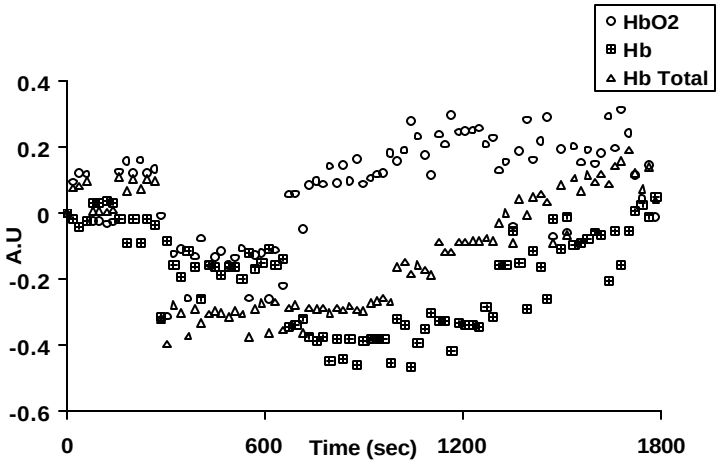

Rat 6

Day 1

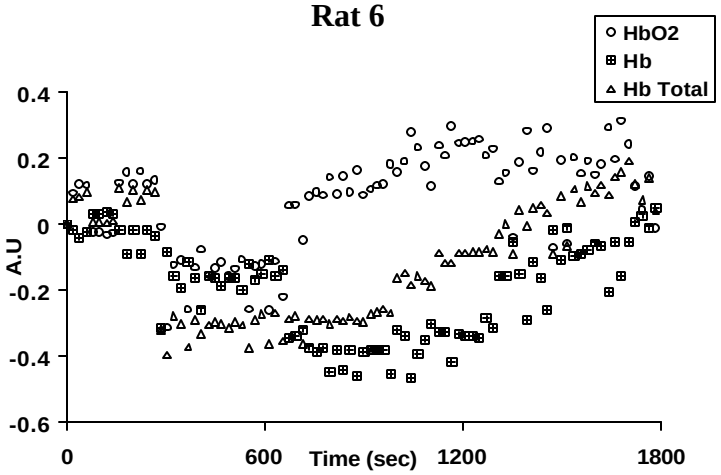

Day 2

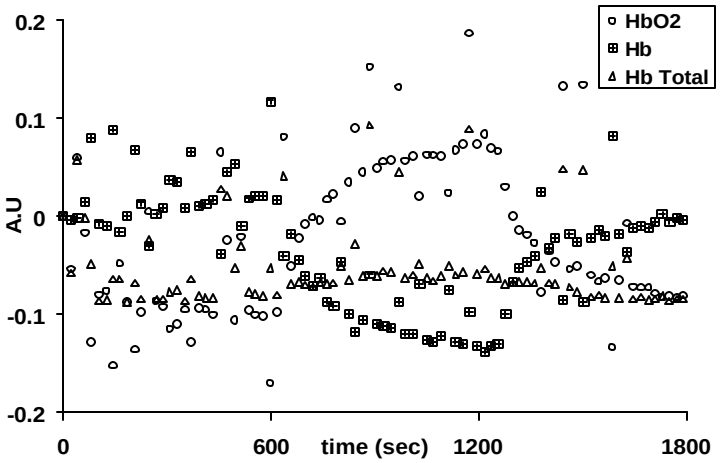

Day 3

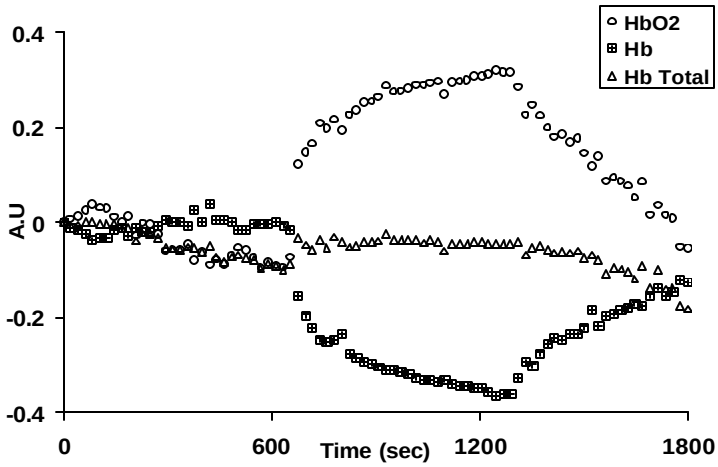
HbO2
Hb
Hb Total
0.4
0.2
0
-0.2
-0.4
A.U
0
600
1200
1800
Time (sec)

Day 4

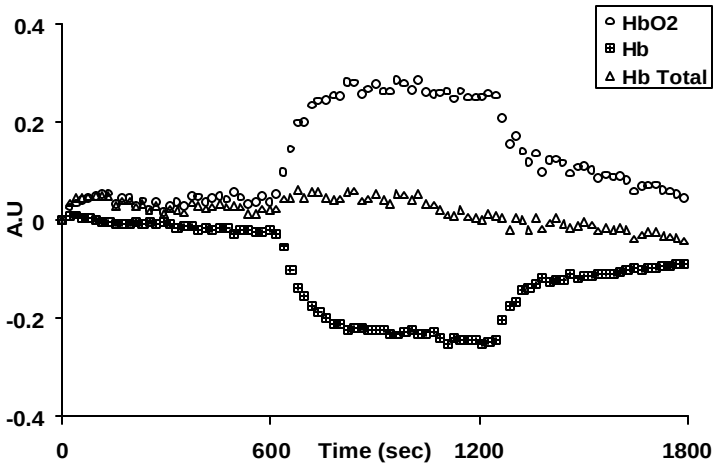
HbO2
Hb
Hb Total
0.4
0.2
0
-0.2
-0.4
A.U
0
600
1200
1800
Time (sec)

A1.2 Low Dose Group

Rat 1

Day 1

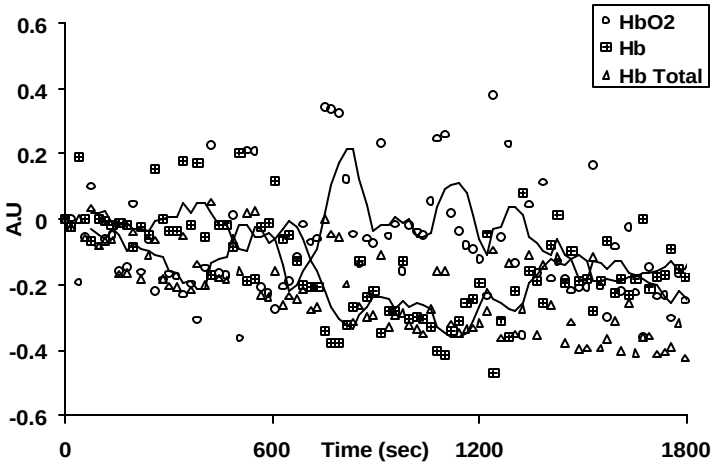

Day 2

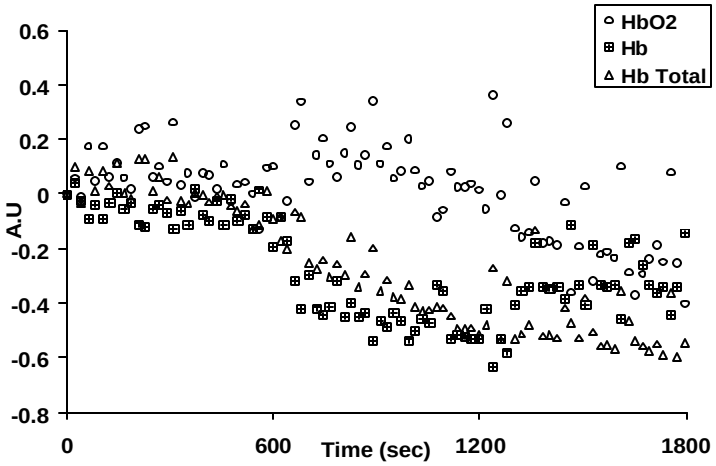

Day 3

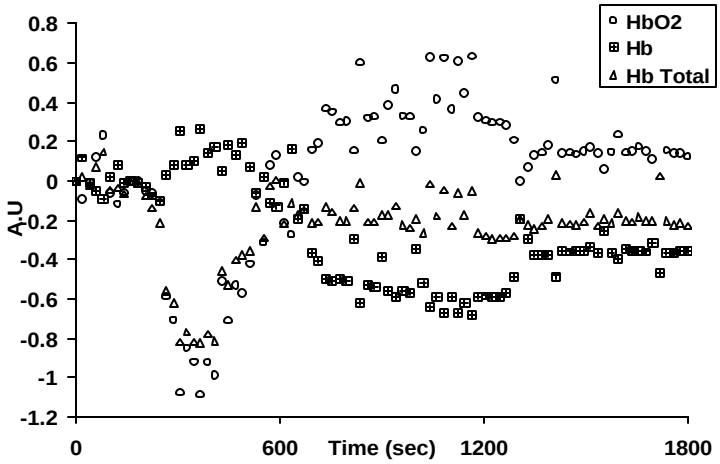

Day 4

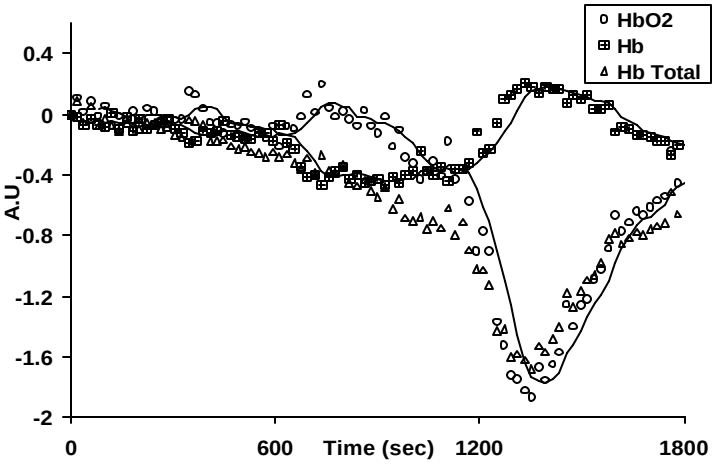

Day 5

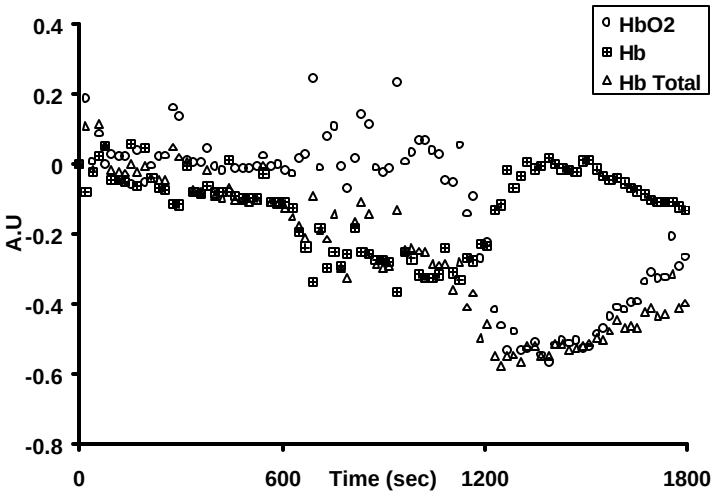

Rat 2

Day 1

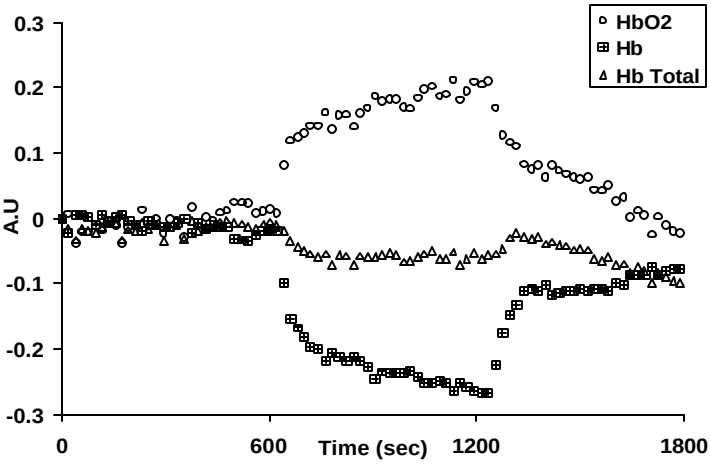

Day 2

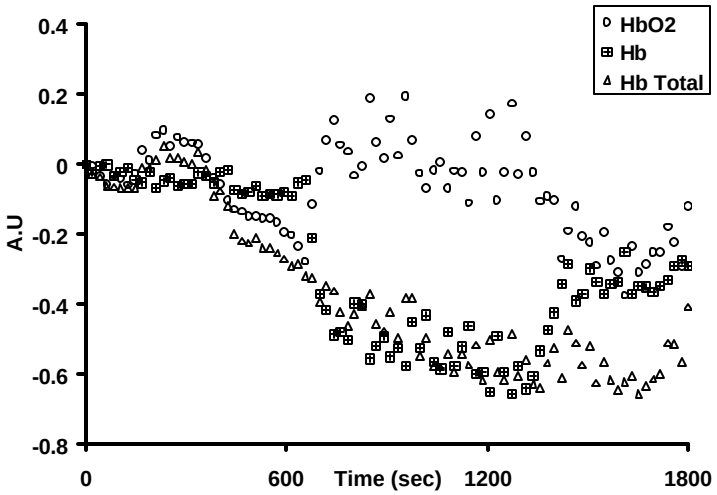

Day 3

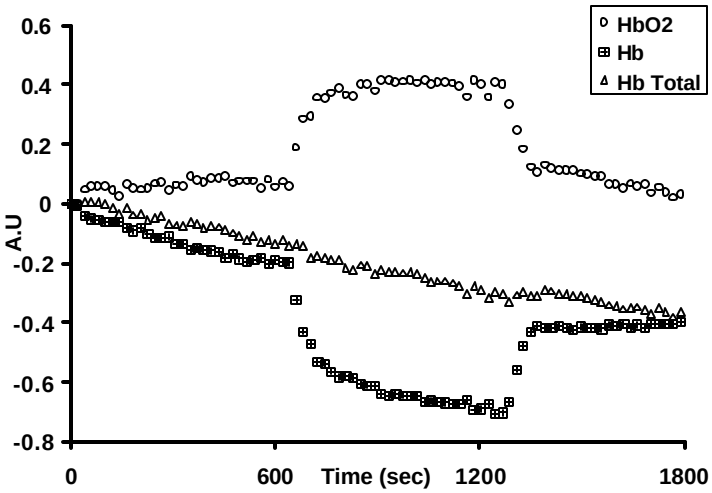

Day 4

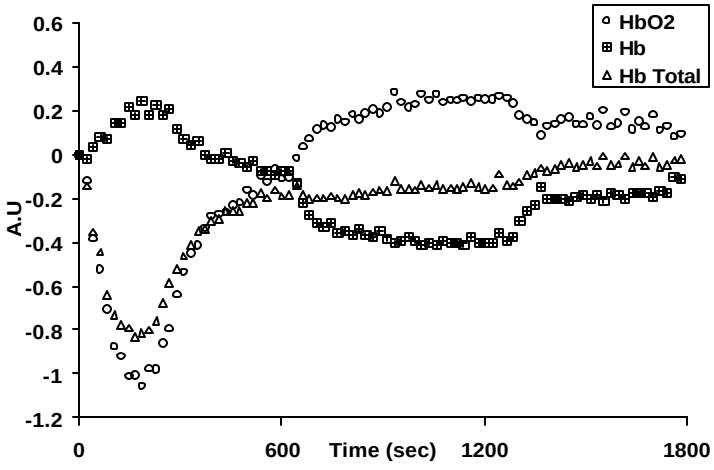

Day 6

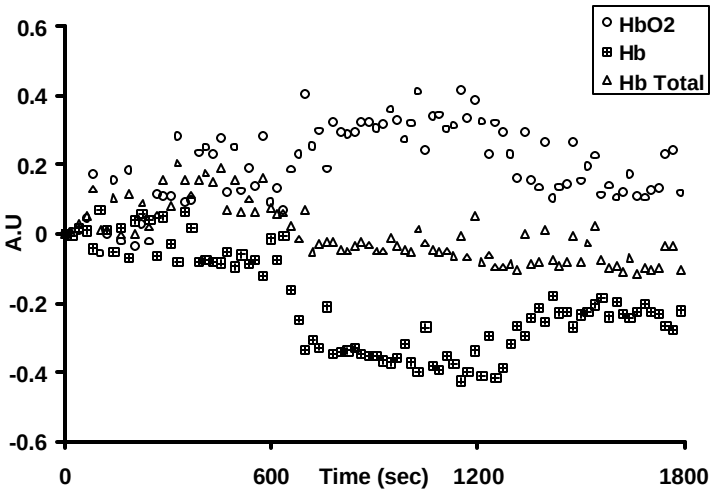

Day 7

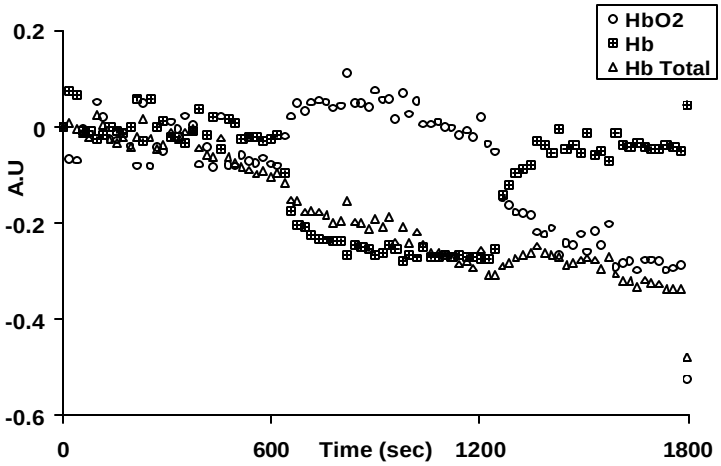

Rat 3

Day 1

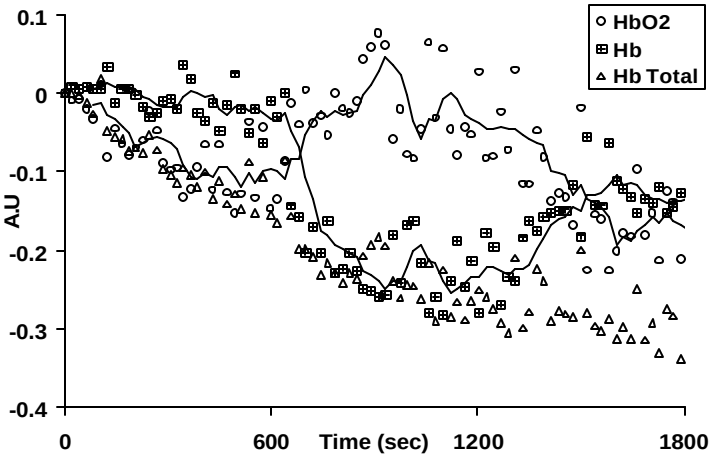

Day 2

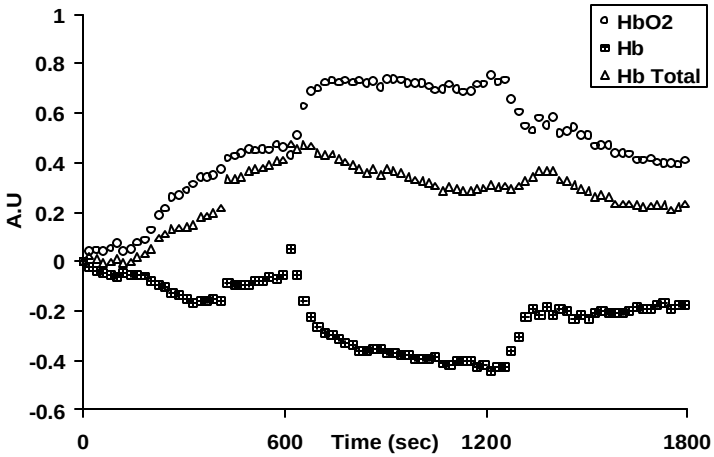

Day 3

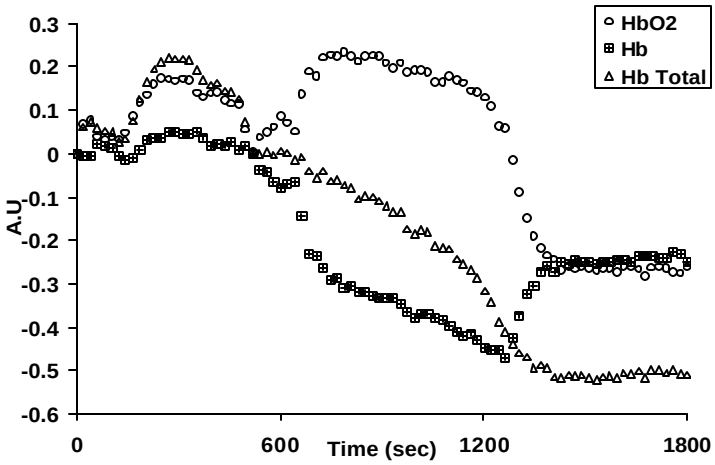

Day 4

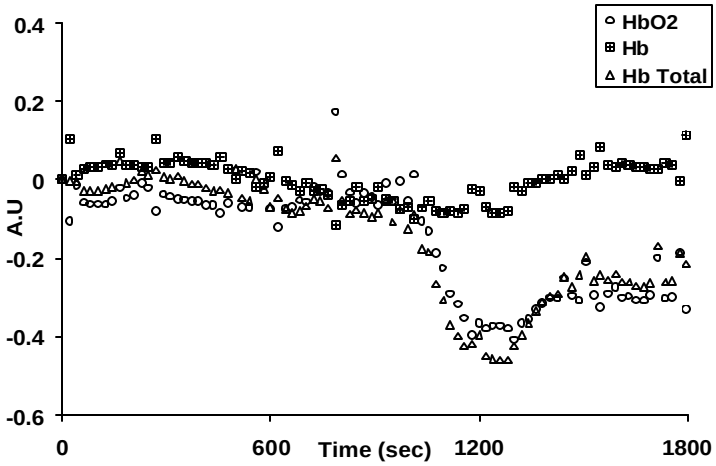

Day 5

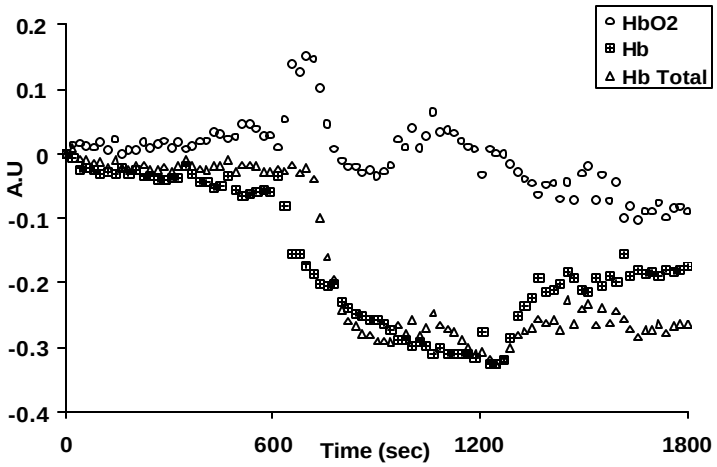

Day 7

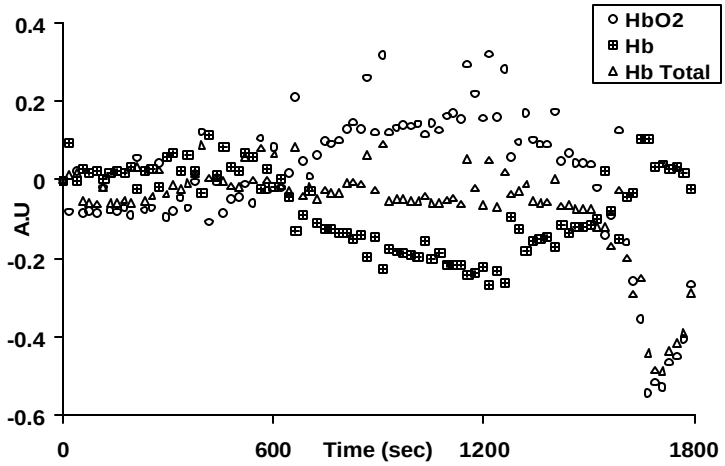

Rat 4

Day 1

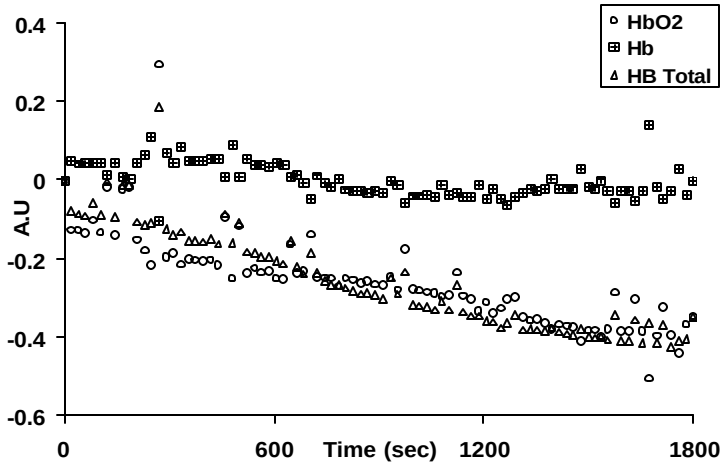

Day 2

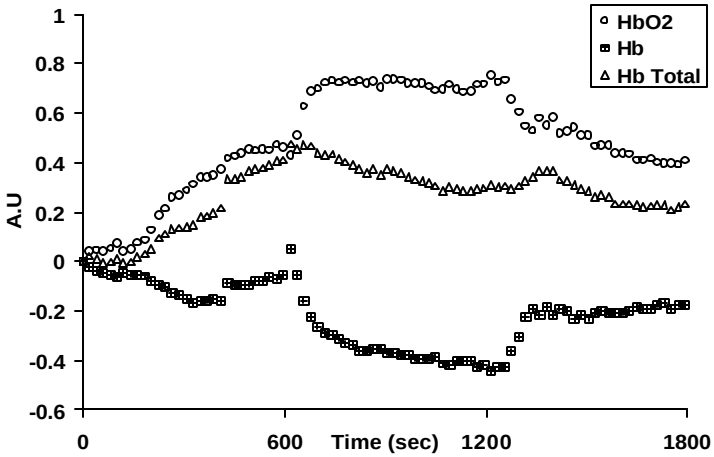

Day 3

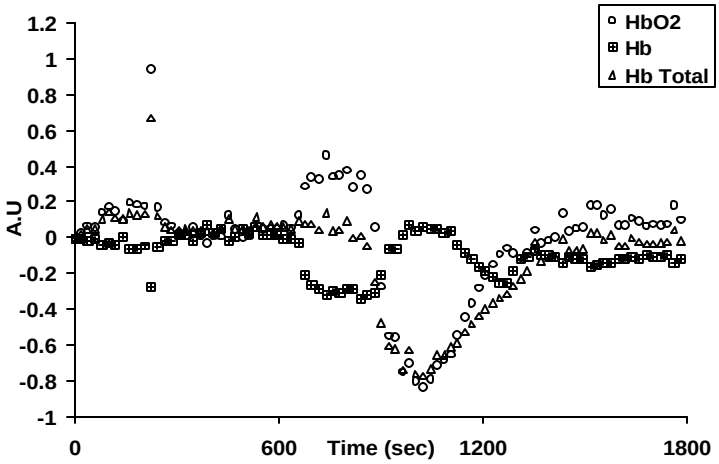

Day 4

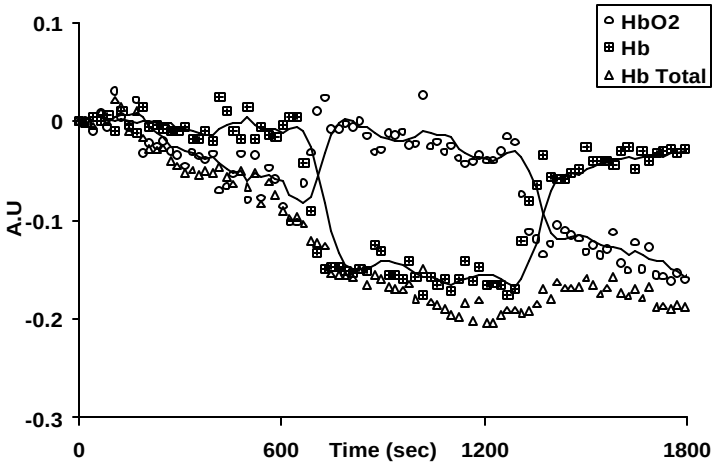

Day 5

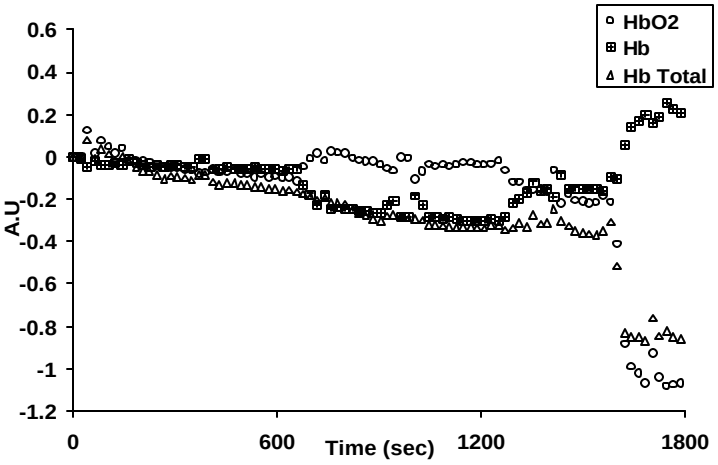

Day 7

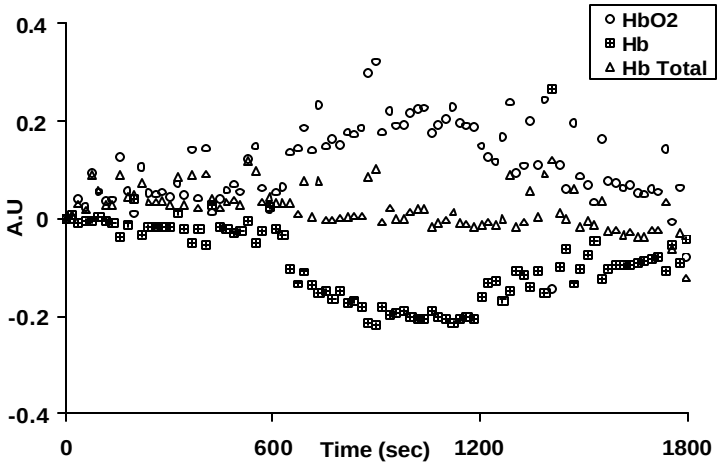

Rat 5

Day 2

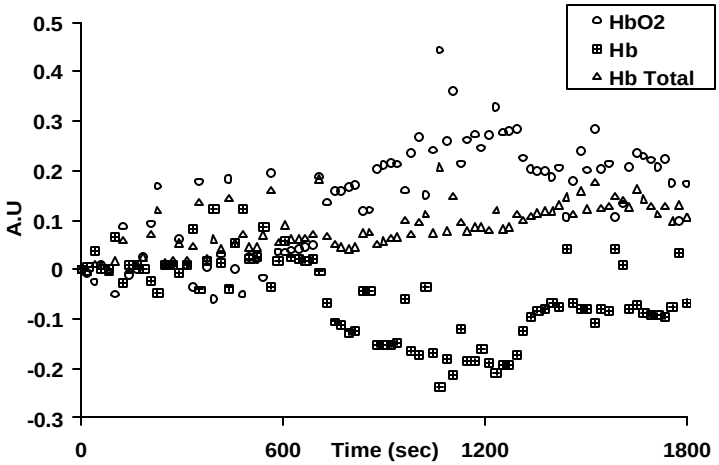

Day 3

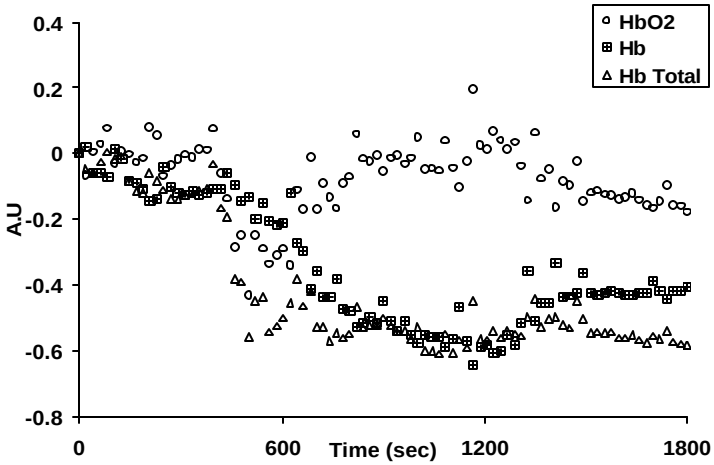

Day 5

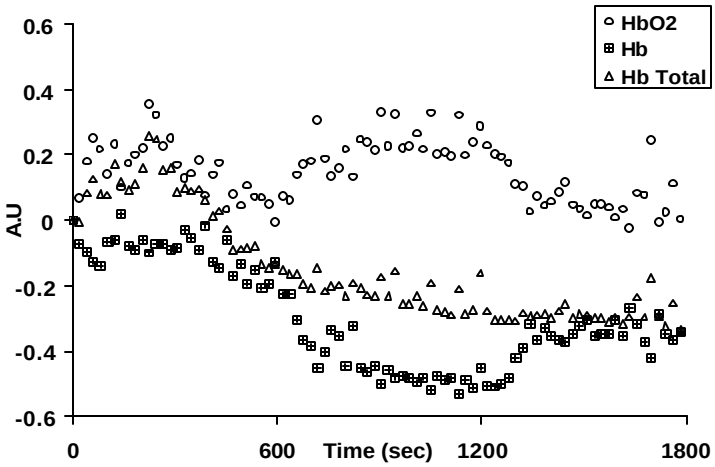

Day 7

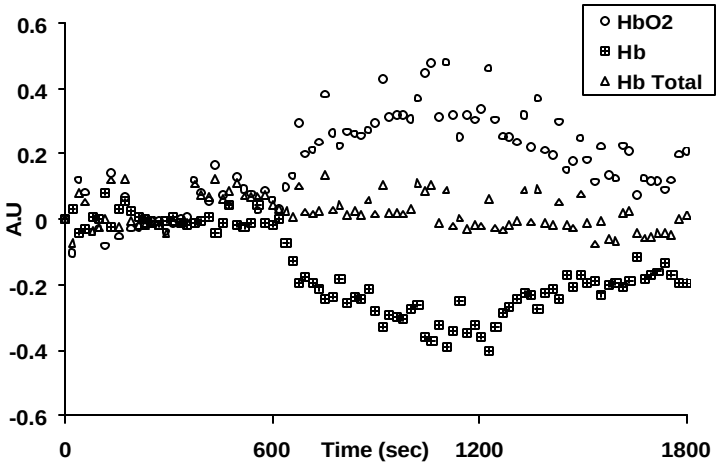

Rat 6

Day 2

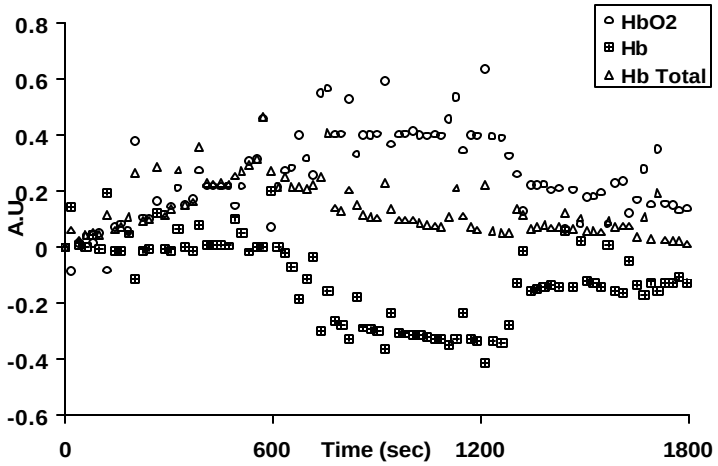

Day 3

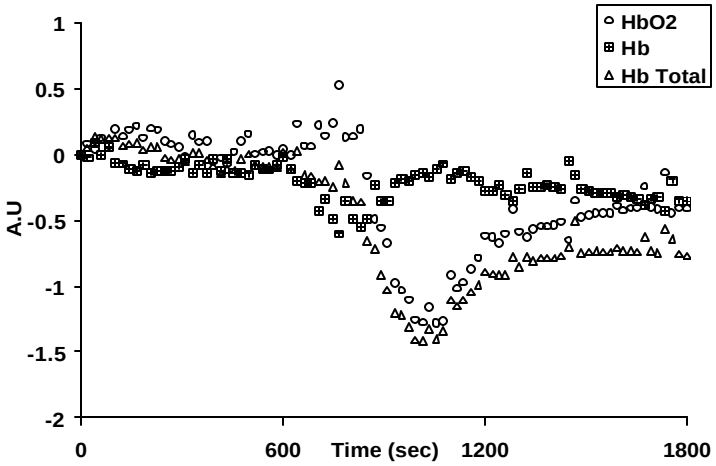

Day 4

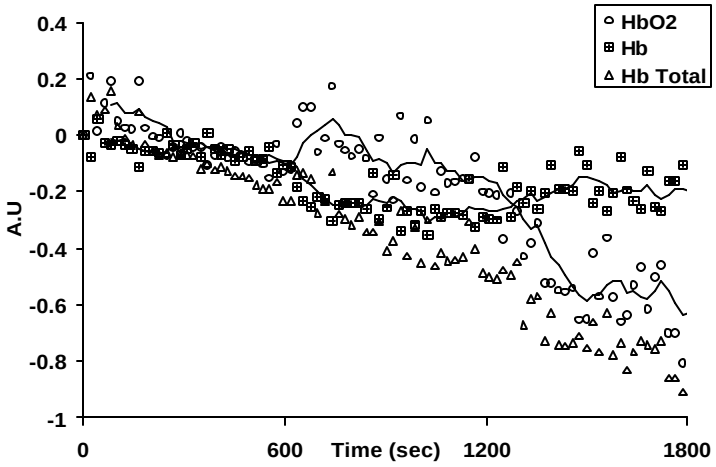

Day 5

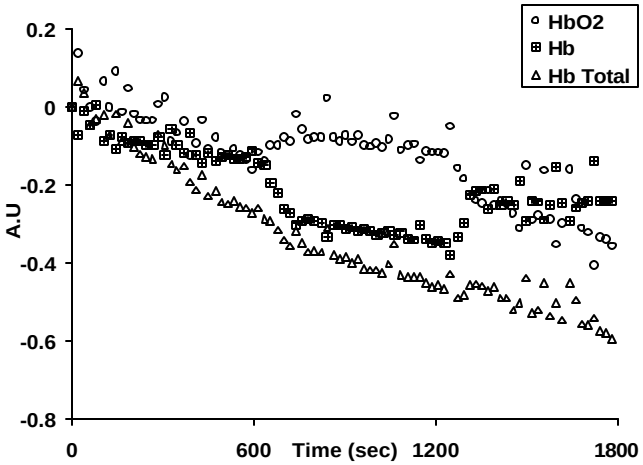
HbO2
Hb
Hb Total
0.2
0
-0.2
-0.4
-0.6
-0.8
A.U
0
600
Time (sec)
1200
1800

Day 7

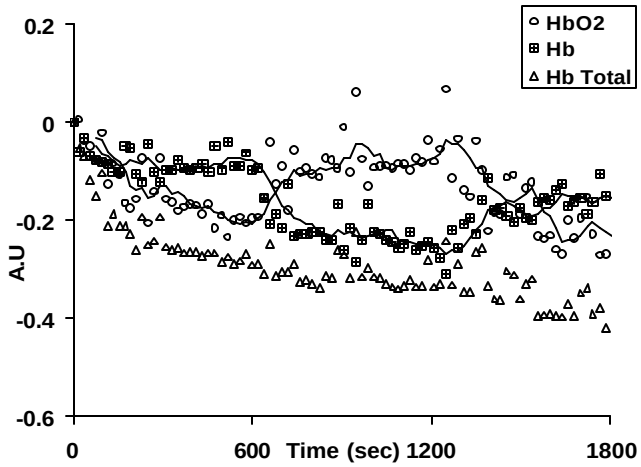
HbO2
Hb
Hb Total
0.2
0
-0.2
-0.4
-0.6
A.U
0
600
Time (sec)
1200
1800

A1.3 High Dose Group

Rat 1

Day 1

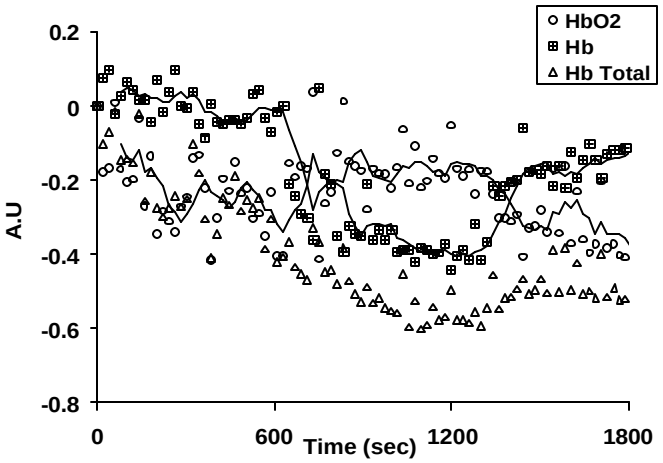

Day 2

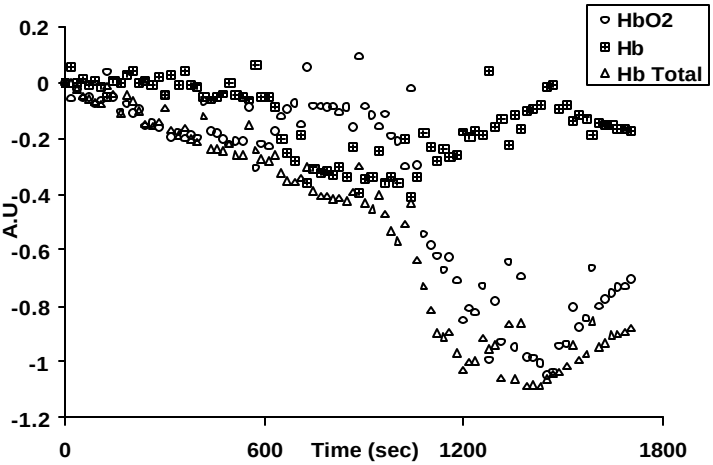

Day 3

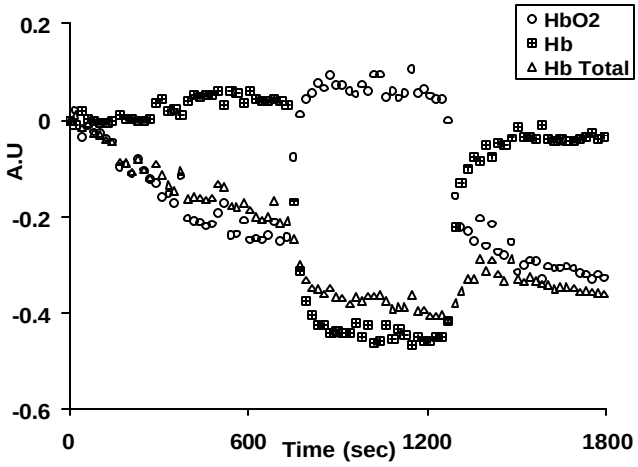

Day 4

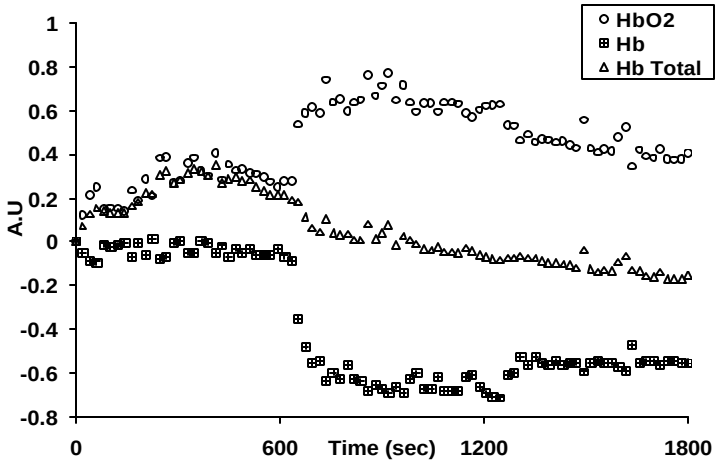

Day 6

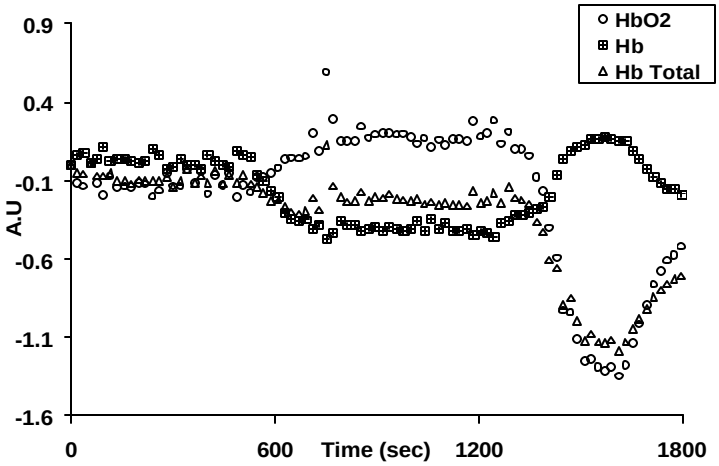

Day 7

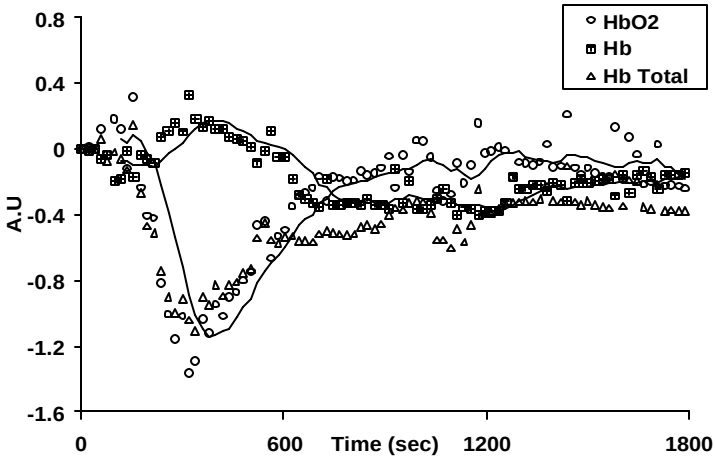

Rat 2

Day 1

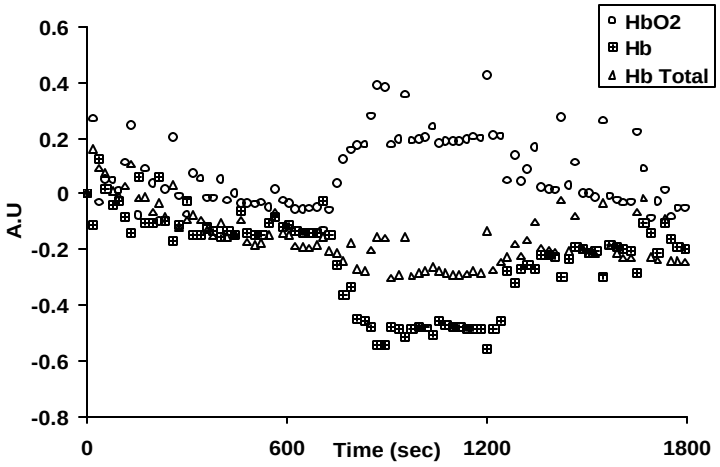

Day 2

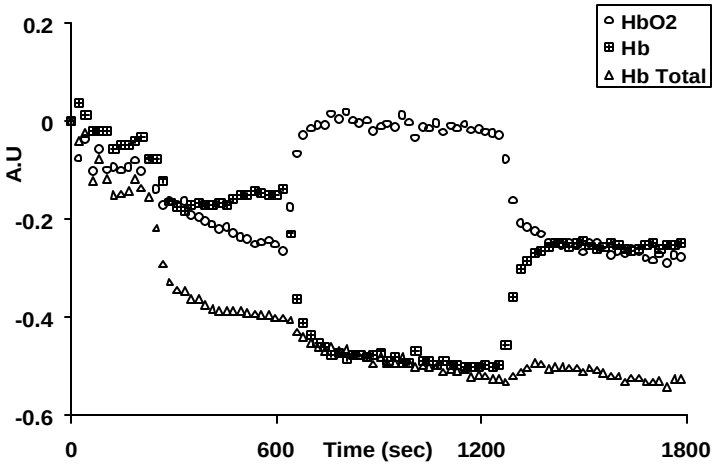

Day 3

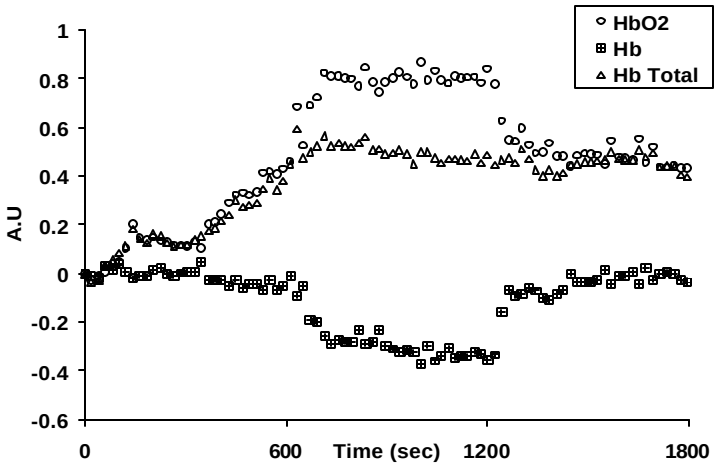

Day 4

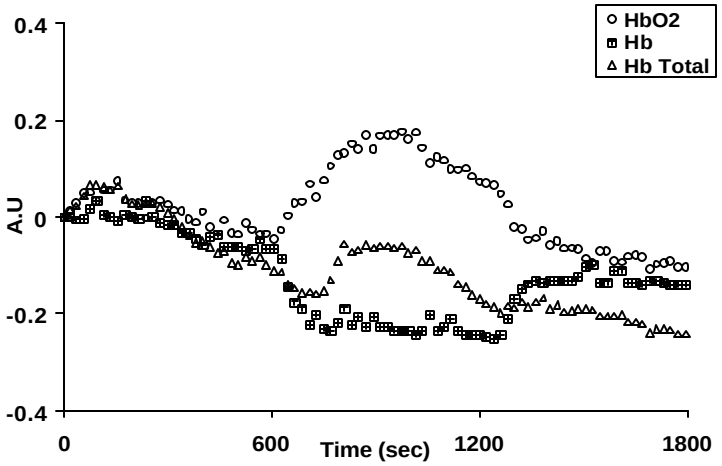

Day 6

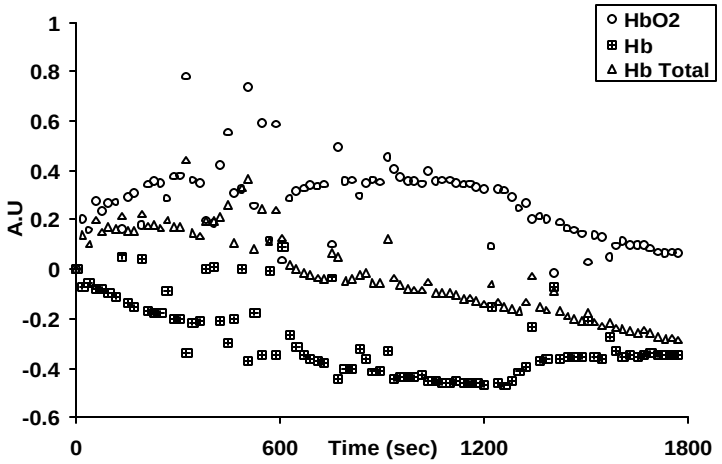

Day 7

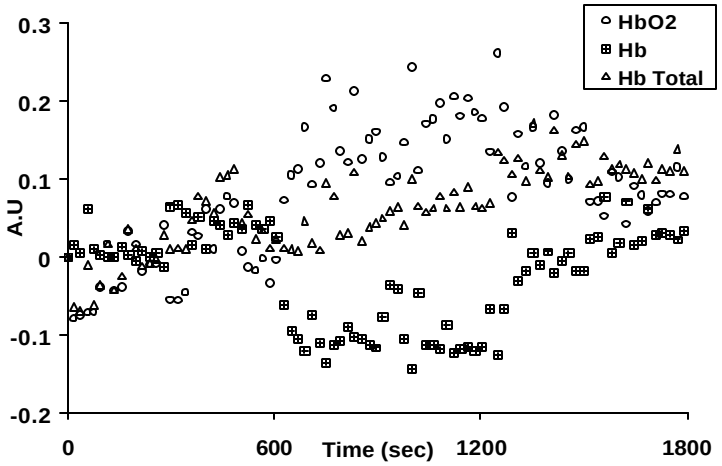

Rat 3

Day 1

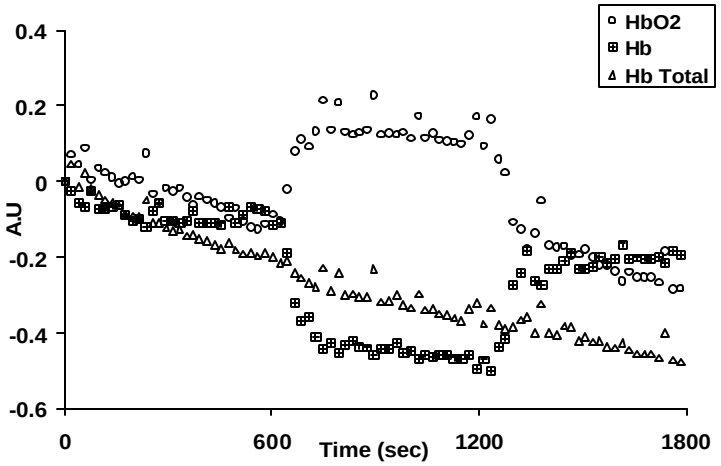

Day 2

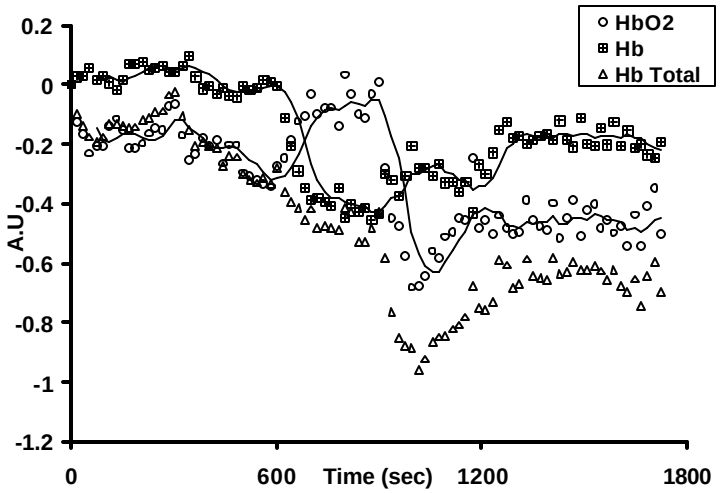

Day 3

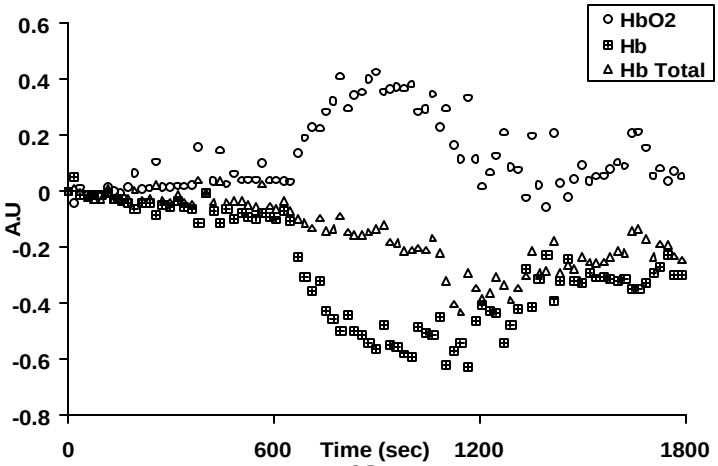

Day 4

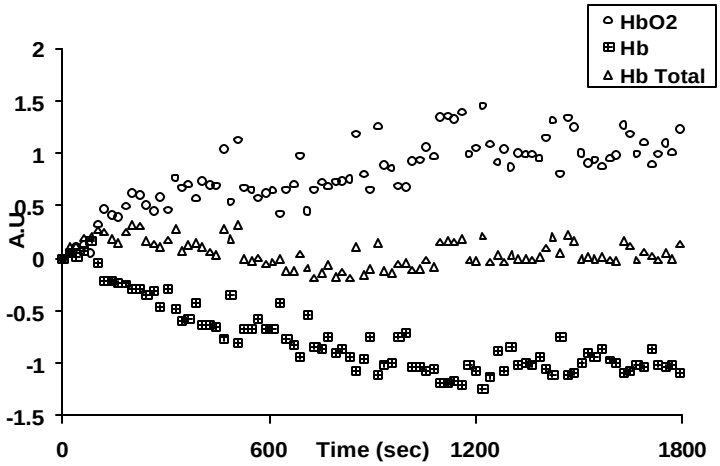

Day 6

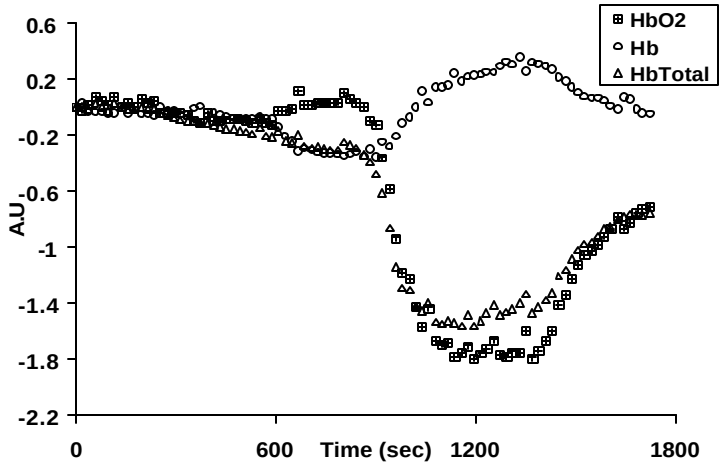

Day 7

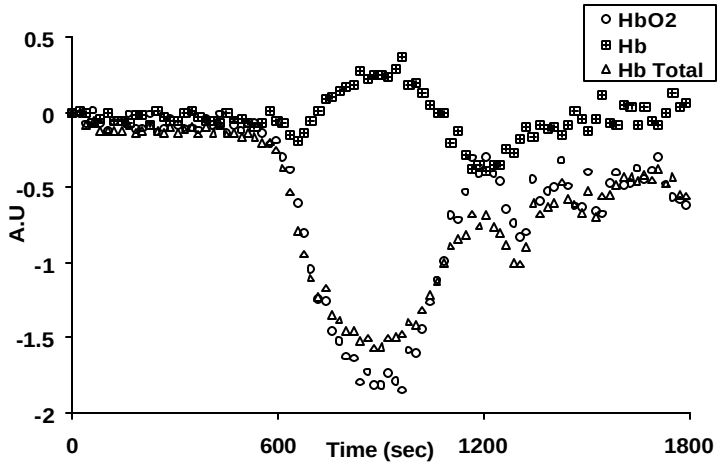

Rat 4

Day 1

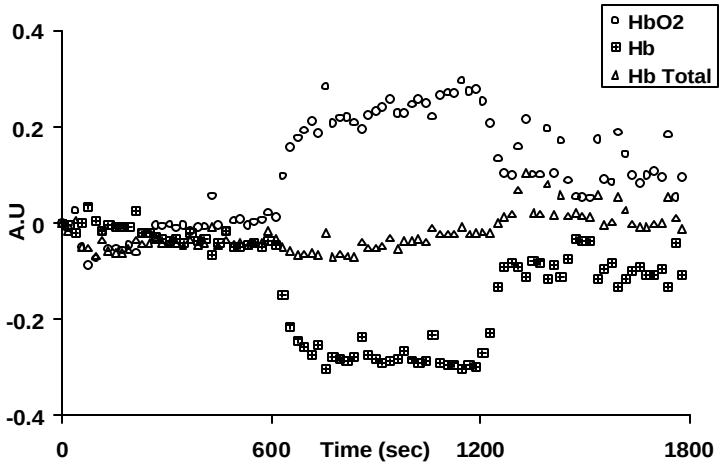

Day 2

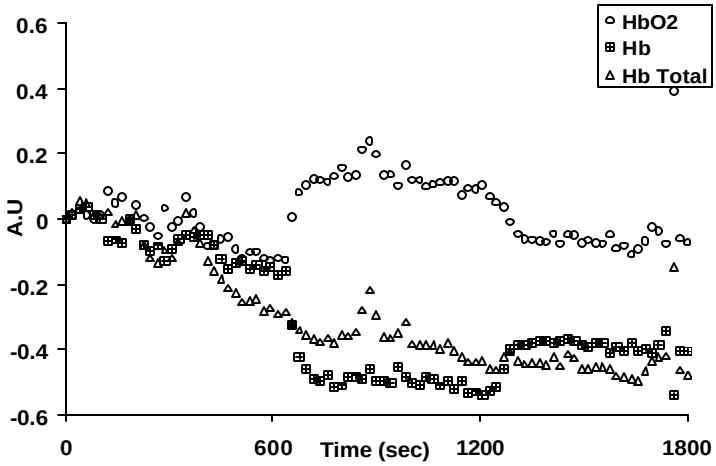

Day 3

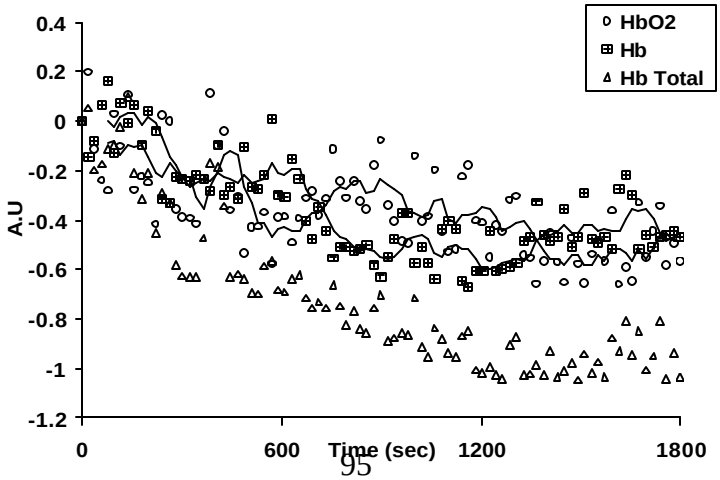

Day 4

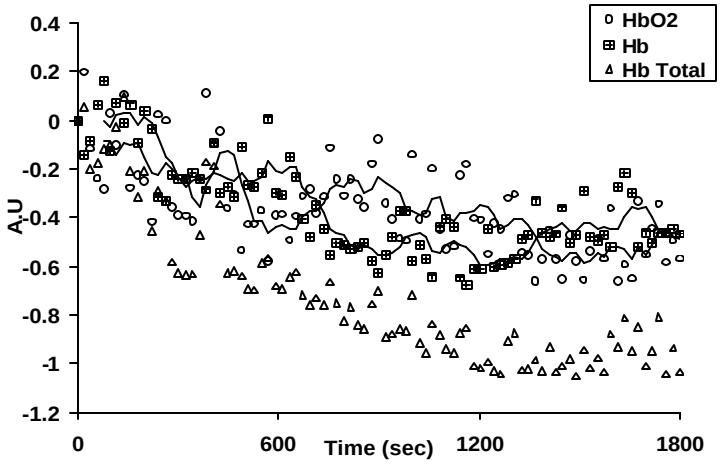

Day 6

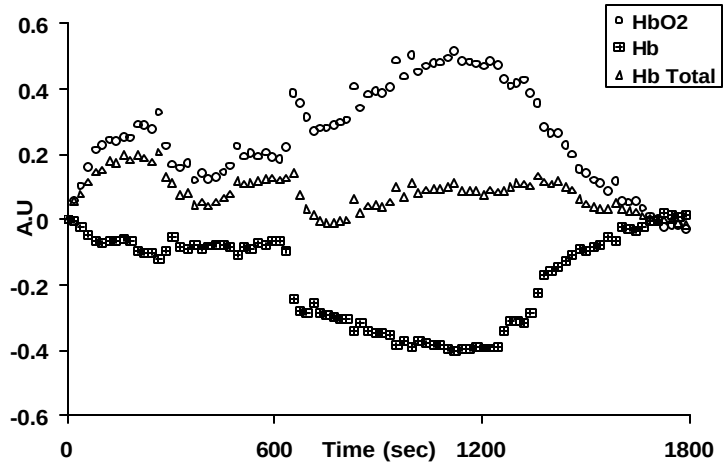

Rat 5

Day 1

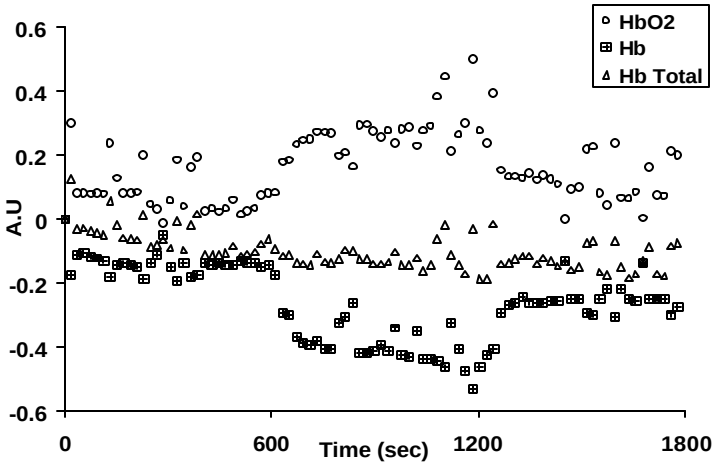

Day 2

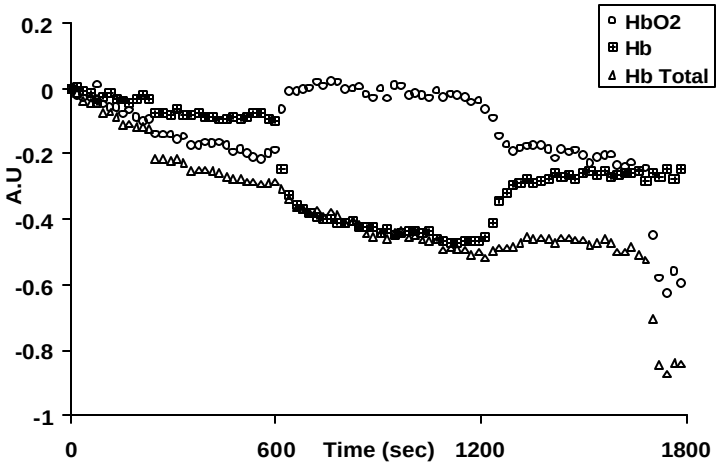

Day 3

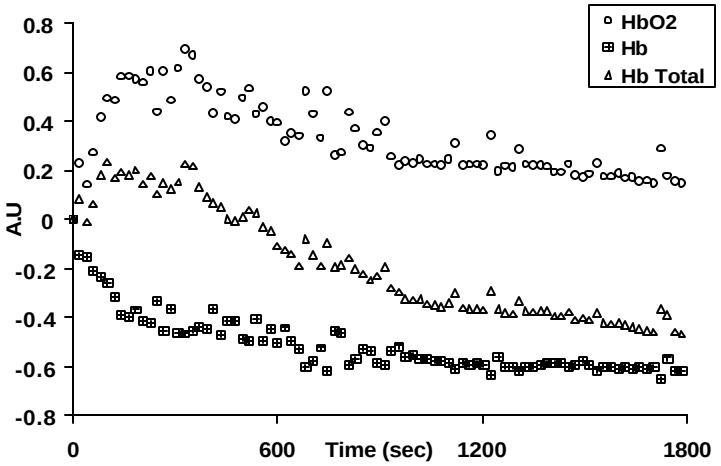

Day 4

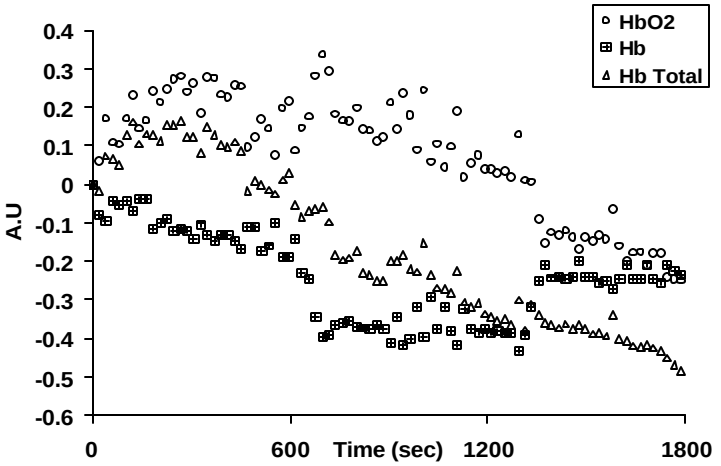

Day 6

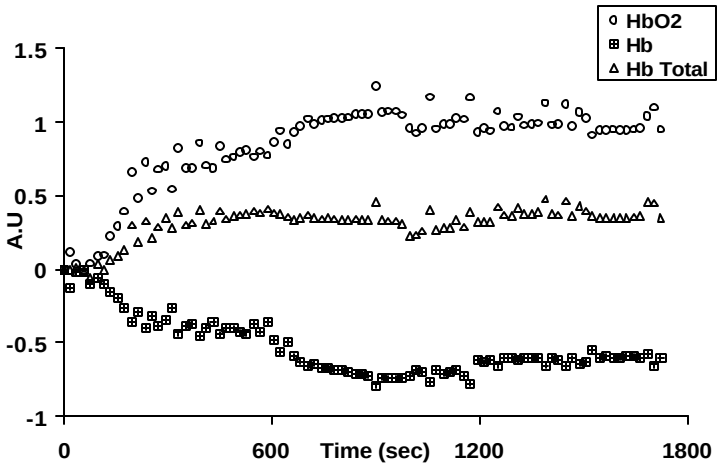
HbO2
Hb
Hb Total
1.5
1
0.5
0
-0.5
-1
A.U
0
600
Time (sec)
1200
1800

Day 7

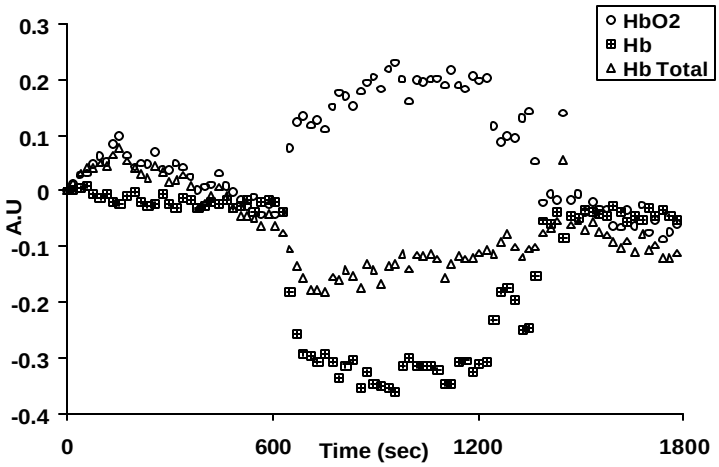
HbO2
Hb
Hb Total
0.3
0.2
0.1
0
-0.1
-0.2
-0.3
-0.4
A.U
0
600
Time (sec)
1200
1800

REFERENCES

1. Liu, H., Y. Song, K. L. Worden, X. Jiang, A. Constantinescu and R. P. Mason, (2000). "Non Invasive Investigation of blood oxygenation dynamics of tumors by near-infrared spectroscopy." Applied Optics, **39**: p. 5231-5243.

2. E.J. van Kampen, W.G.Zilstra,(1965)."Determination of hemoglobin and its derivatives." Adv. Clin. Chem. **8**: p. 141-187.

3. R. Benesch, G.M., and R.E. Benesch,(1965)."Determination of oxygen equilibria with a versatile new tonometer." Analytical. Biochemistry, **11(1)**: p. 81-87.

4. R.E. Benesch, R.B., and S. Yung,(1973) "Equations for the spectrophotometric analysis of hemoglobin mixtures." Analytical. Biochemistry, **55(1)**: p. 245-248.

5. Zijlstra, W.G.,(1975) "Extinction coefficients for use in equations for the spectrophotometric analysis of haemoglobin mixtures." Analytical. Biochemistry, **69**: p. 43-48.

6. W.G. Zijlstra, A.B., and A. Zwart,(1983) "Molar absorptivities of human hemoglobin in the visible spectral range." Journal of Applied Physiology: Respiratory. Environment Exercise Physiology, **54(5)**: p. 1287–1291.

7. Kim J.G., M. Xia and H. Liu.(2005) "Extinction coefficients of hemoglobin for near-infrared spectroscopy of tissue." Engineering in Medicine and Biology Magazine, IEEE, 2005. **24(2)**: p. 118 - 121.

8. G.E. Healey, and R. Kondepudy.(1994), "Radiometric CCD Camera Calibration and Noise Estimation." IEEE Transactions on Pattern Analysis and Machine Intelligence, 1994. **16(3)**: p. 267-276.

9. American Cancer Society.(2006), "Cancer Facts and Figures. Atlanta: 2006 American Cancer Society."

10. Folkman, J.(2003), "Fundamental Concepts of the Angiogenic Process." Current Molecular Medicine, **3**: p. 643-651.

11. Folkman, J.(2006), "Angiogenesis." Annu. Rev. Med, **57**: p. 1-18.

12. Bo Lennerna¨s, P.A., Hans Lennerna¨s and Klas Norrby, (2003) "Chemotherapy and Antiangiogenesis." Acta Oncologica. **42(4)**: p. 294-303.

13. Kim, J.G.,(2005) “Investigation of Breast Tumor Hemodynamics by Near Infrared Spectroscopy: Applications to Cancer Therapy Monitoring.” Dissertation in Biomedical Engineering, University of Texas at Arlington.

14. Ranga, R.(2005) “An In Vitro Hemodynamic Phantom Model for Near Infrared Spectroscopy.” in Biomedical Engineering., University of Texas at Arlington.

15. L. Gray, A.C., M. Ebert, S. Hornsey and O. Scott,(1953) “The concentration of oxygen dissolved in tissues at time of irradiation as a factor in radio-therapy.” Br. J. Radiol., **26**: p. 638-648.

16. J. H. Kaanders, L.A.P., H. A. Marres, J. Liefers, F. J. van den Hoogen, W. A. van Daal, A. J. and van der Kogel,(1998)”Accelerated radiotherapy with carbogen and nicotinamide (ARCON) for laryngeal cancer”. Radiother. Oncol., **48**: p. 115-122.

17. M.Horsman, J.Overgaard.,(1996) “Modification of hypoxia-induced radioresistance in tumors by the use of oxygen and sensitizers”. Semin. Radiat. Oncol., **6**: p. 10-21.

18. Cheong, W., S. A. Prahl and A. J. Welch,(1990) "A Review of the optical properties of biological tissue." IEEE Journal of Quantum Electronics,. **26**: p. 2166-2184.

19. J. G. Kim, A.C., R. P. Mason, and H. Liu, (2003)“Dynamic Response of Breast Tumor Oxygenation to Hyperoxic Respiratory Challenge Monitored with Three Oxygen-Sensitive Parameters.” Applied Optics, **42**: p. 2960-2967.

20. E. W. Hahn, P.P., R. P. Mason, E. E. Babcock, and P. P.Antich,(1993) “Isolated tumor growth in a surgically formed skin pedicle in the rat: a new tumor model for NMR studies.” Magnetic Resonance Imaging, **11**: p. 1007-1017.

21. Dawen Zhao, L.J., Eric W. Hahn and Ralph P. Mason,(2005) "Continuous Low-Dose (Metronomic) Chemotherapy on Rat Prostate Tumors Evaluated Using MRI In Vivo and Comparison with Histology." Neoplasia, **7(7)**: p. 678 – 687.

22. Shechao Feng, Fan-An Zeng, and Britton Chance,(1995) “Photon migration in the presence of a single defect: a perturbation analysis.” Applied Optics **34(19)**:p. 3826-3827.

23. M.S. Patterson, B. Chance, and C. Wilson,(1989) “Time resolved reflectance and transmittance for the non invasive measurement of tissue optical properties.” Applied Optics **28**:p. 2331-2336

24. C. Baudelet and B. Gallez,(2004) ”Effect of anesthesia on the signal intensity in tumors using BOLD-MRI: Comparison with flow measurements by laser Doppler

Flowmetry and oxygen measurements by luminescence based probes." Magnetic Resonance Imaging **22**:p.905-912

25. Ben J. A. Janssen, Tijl De Celle, Jacques J. M. Debets, Agnieszka E. Brouns, Michael F. Callahan, and Thomas L. Smith, (2004) "Effects of anesthetics on systemic hemodynamics in mice." American Journal of Circulatory Physiology **(287)**:p. H1618–H1624

26. Zijlstra, W. G.,(2000) "Visible and near infrared absorption spectra of human and animal hemoglobin." Book, publisher O. W. V. Assendelft, VSP.

BIOGRAPHICAL INFORMATION

Manan Goel was born on March 8, 1982 in India. He earned his Bachelor of Engineering degree in Instrumentation and Control Engineering from University of Pune, India in 2004. With a keen interest in biomedical engineering, he started working towards his masters in Biomedical Engineering in fall 2004 from Joint Program of Biomedical Engineering at the University of Texas at Arlington and University of Texas Southwestern Medical Center at Dallas, completing it by summer 2006. His research interests include image processing and analysis, tissue optics, near infrared spectroscopy and image reconstruction.